University of New Mexico
UNM Digital Repository

Earth and Planetary Sciences ETDs

Electronic Theses and Dissertations

Fall 11-14-2022

Dense Array Seismic Imaging of Earth's Crust Using Active and Passive Sources

Evans Awere Onyango
University of New Mexico - Main Campus

Follow this and additional works at: https://digitalrepository.unm.edu/eps_etds

Part of the Geophysics and Seismology Commons

Recommended Citation

Onyango, Evans Awere. "Dense Array Seismic Imaging of Earth's Crust Using Active and Passive Sources." (2022). https://digitalrepository.unm.edu/eps_etds/330

This Dissertation is brought to you for free and open access by the Electronic Theses and Dissertations at UNM Digital Repository. It has been accepted for inclusion in Earth and Planetary Sciences ETDs by an authorized administrator of UNM Digital Repository. For more information, please contact disc@unm.edu.

Evans Awere Onyango

Candidate

Earth and Planetary Sciences

Department

This dissertation is approved, and it is acceptable in quality and form for publication:

Approved by the Dissertation Committee:

Dr. Lindsay L. Worthington

Chair

Dr. Brandon Schmandt

Member

Dr. Robert E. Abbott

Member

Dr. Susan L. Bilek

Member

Dense Array Seismic Imaging of Earth's Crust Using Active and Passive Sources

BY

Evans Awere Onyango
B.S., Geophysics, University of Houston, 2016

DISSERTATION

Submitted in Partial Fulfillment
of the Requirements for the Degree of
Doctor of Philosophy

Earth and Planetary Sciences
The University of New Mexico
Albuquerque, New Mexico

December, 2022

DEDICATION

To my parents, William and Margaret, for their support, encouragement, and sacrifice.

ACKNOWLEDGEMENTS

I would like to take this opportunity to express my thanks to those who helped me with various aspects of conducting research and the writing of this thesis. First, Dr. Lindsay L. Worthington for her guidance, patience and overwhelming support throughout this research and the writing of this manuscript and related publications. Her insights and words of encouragement have often inspired me and renewed my hopes for completing my graduate education. I would also like to thank my committee members for their efforts and contributions to this work: Dr. Brandon Schmandt, Dr. Robert E. Abbott and Dr. Susan L. Bilek. I would additionally like to thank Dr. Schmandt for his technical guidance and allowing me to drop-in to his office anytime with questions throughout my graduate career. Dr. Abbott for guidance in the first two years and for tolerating a barrage of emails and forms throughout my graduate career. Dr. Bilek for inspiring me as an IRIS intern and for being available even with short notice.

From the Earth and Planetary Sciences Department at the University of New Mexico, I thank several professors who showed interest in my research and well-being. In particular, Dr. Peter Fawcett, Dr. Yemane Asmerome, Dr. Louis Scuderi and Dr. Gary Weissman. It was a pleasure working with Dr. Aurora Pun as a teaching assistant, and Dr. Eric Lindsey as a teaching assistant and instructor at the Earth Sciences Computing and Programming Experience program. I thank my office mates Justin Wilgus, Collin Brandl, Margaret Glasgow, Han Zhang, Olumide Adedeji, Sarah Nolt-Caraway, Ian Podmore, Joshua Osasona and Loring Schaible for their professionalism and for sharing their expertise.

I thank numerous people who have taught and inspired me professionally including Dr. Donna Shillington (NAU), Dr. Carl Tape (UAF), Dr. Jenny Nakai (Alaska Volcano Observatory) and Dr. Shuhab Khan (UH).

Finally, I thank my family for their unceasing love and support throughout my time at UNM. My wife Kulagwa for being my steadfast supporter all the time. Micah for being a dependable big brother, and Vance for keeping your room clean even when I wasn't looking. Gratitude to my family in Kenya, Tanzania, Houston and California.

Funding for these studies came from scholarships from the UNM Earth and Planetary Sciences Department, the DOE and several NSF awards from different principal investigators.

Dense Array Seismic Imaging of Earth's Crust Using Active and Passive Sources

by

Evans Awere Onyango

B.S., Geophysics, University of Houston, 2016

Ph.D., Earth and Planetary Sciences, University of New Mexico, 2022

ABSTRACT

Imaging Earth's crust is critical to understanding processes in the near-surface that affect civilization such as the interaction of seismic waves with the near-surface to generate natural or man-made hazards or investigating how the shallow crust affects the distribution of resources. In chapter 1, I processed and analyzed active source seismic data recorded by ∼1000 geophones that were acquired over the legacy HADDOCK nuclear test at the Nevada National Security Site. Using seismic reflection and refraction methods, we image the partially collapsed post-detonation structure to better understand the velocity structure in and around the HADDOCK chimney. Results from this work can be generalized to assist in the investigation of suspected Underground Nuclear Explosions and support ongoing source physics experiments at the Nevada National Security Site. In chapter 2, I investigate the subduction zone interface structure beneath Kodiak Island in Alaska. I estimate P-to-S receiver functions from distant earthquakes recorded by ∼400 three-component 5 Hz geophones. We determined that the 1964 Great Alaska Earthquake ruptured beyond the extent of the low-velocity shear zone observed in the Kenai Peninsula. In chapter 3, I study the subsurface structure of the Raton Basin in New Mexico. I analyze teleseismic waveforms recorded by nine broadband

and 96 5 Hz geophones deployed at different times within the last fourteen years. Results from this work show that the top of the Early Cretaceous-age Dakota Formation is the most prominent seismic boundary basin-wide. The results also suggest that local earthquakes attributed to reactivated basement faults occur from roughly the sediment-basement boundary and extend deeper into the Precambrian basement. The three chapters presented here were prepared as manuscripts to be submitted for publication in peer-reviewed Earth Sciences journals. Chapter 1 is modified from a manuscript that was published in the *Bulletin of the Seismological Society of America, 2021, Volume 111.* Chapter 2 was published in *Geophysical Research Letters, 2022, Volume 49.* A version of Chapter 3 will be submitted to a peer-reviewed journal. Together these works create high-resolution images of the near-surface environment to better understand both man-made and natural geologic structures.

Contents

List of Figures xi

List of Tables xxiii

1 Dense Seismic Array study of a Legacy Underground Nuclear Test at the Nevada National Security Site 1

1.1 Abstract 1
1.2 Introduction and Motivation 2
1.3 Geological Setting 6
1.4 Background and Previous Work 7
1.5 Data 8
1.6 Methods 10
  1.6.1 Tomographic inversion 10
  1.6.2 2D seismic reflection processing and imaging 13
  1.6.3 Forward modeling 18
1.7 Results 22
  1.7.1 Tomographic inversion 22
  1.7.2 2D seismic reflection processing and imaging 24
  1.7.3 Forward modeling 24
1.8 Discussion 29
  1.8.1 Limitations of seismic imaging 29
  1.8.2 Chimney structure 31

1.9 Conclusions 33
1.10 Data and Resources 33
1.11 Acknowledgements 34

References 35

Appendices 45

1.A Supplementary Figures 45

2 Subduction Zone Interface Structure Within the Southern Mw9.2 1964 Great Alaska Earthquake Asperity: Constraints From Receiver Functions Across a Spatially Dense Node Array 48

2.1 Abstract 48
2.2 Introduction 49
2.3 Geologic Background and Previous Geophysical Studies of the 1964 Rupture Area 51
2.4 Data and methods 53
2.4.1 The AACSE 53
2.4.2 Receiver Function Processing 53
2.4.3 1-D Synthetic Modeling 55
2.5 Results 57
2.5.1 Receiver Function Imaging 57
2.5.2 Synthetic Modeling Results 58
2.6 Discussion 58
2.6.1 Absence of Oceanic Crust Arrival 58
2.6.2 Evidence of Rupture Across a Heterogenous Plate Interface . . 62
2.6.3 Implications for Rupture Dynamics 63
2.7 Conclusions 64
2.8 Data Availability Statement 65

2.9 Acknowledgements 65

References **66**

Appendices **76**

2.A Supplementary Figures 76

2.B Supplementary Tables 80

3 Geometry and Subsurface Characterization of the Raton Basin using Teleseismic Receiver Functions **81**

3.1 Abstract 81

3.2 Introduction 82

3.3 Geologic Background and Previous Geophysical Studies 86

3.4 Data and methods 89

3.4.1 Broadband Data and Processing 89

3.4.2 Nodal Data and Processing 90

3.4.3 Receiver Function Calculation 92

3.4.4 EPI Gather Analysis 94

3.4.5 H-k Stacking 95

3.4.6 Stratigraphic Data 101

3.5 Results 101

3.5.1 Receiver Function Results 101

3.5.2 H-k stacking Results 102

3.6 Discussion 102

3.6.1 Limitations of Seismic Imaging 102

3.6.2 Identification of the Top-of-Dakota Formation Signal 103

3.6.3 Implications for Induced Seismicity 104

3.7 Conclusions 105

3.8 Data Availability Statement 105

References 106

Appendices 110

3.A Supplementary Figures 110

List of Figures

1.2.1 (a) Shaded topographic map of the Yucca Flat region of the Nevada National Security Site (NNSS). The blue line marks the NNSS boundary. The red line marks the Yucca Flat sedimentary basin boundary. The FREY experiment's Line 500 and Line 600 are shown as the black X. The purple line marks the location of the legacy seismic line LANL-80-6. Subsidence sinks formed from legacy nuclear testing dominate the eastern side of the basin. (b) Quaternary geology of Yucca Flat Basin (Slate et al., 2000). Refer to Slate et al. (2000) for geologic unit explanation. (c) Shaded relief image showing receiver geometry of the FREY experiment. The black dots mark the positions of the geophones. (d) Shaded relief image showing shot geometry of the experiment. Blue circles are shot locations of the Seismic Hammer. Red circles mark the positions of the P/S 100 Accelerated Weight Drop (AWD) shots. Inset is a map of Nevada showing the location of the NNSS and the Yucca Flat. 5

1.5.1 (a) Shows raw Seismic Hammer shot number 43 on Line 500. The red line shows first arrival picks and the red arrows at the bottom of the record indicate bad traces. The phase labeled A is the ground-roll, B are reflections plus noise and C is the pre-shot noise. (b) Plot of first arrivals of shots on Line 500. (c) Plot of first arrival picks of shots on Line 600. 11

1.6.1 AWD Inline shot 43 Line 500 shot gather (top) and the normalized average amplitude spectra for the regions in the red rectangles (bottom). (A) ground-roll, (B) first-break, (C) 59–64 Hz near offset noise, (D) reflection contaminated with noise, (E) pre-shot noise. 12

1.6.2 Field data processing workflow. 14

1.6.3 Selected AWD shot gathers in time and frequency-wavenumber (f-κ) domain. (a) f-κ filtering of AWD inline shot gather 93 Line 500 (positive offset). (Left) Gained (automatic gain control 0.5 s window) unfiltered data in the time domain, (center) f-κ domain, and (right) f-κ filtered data in time domain. The arrivals are labeled as follows: A, ground-roll; B, first break; C, reflections; D, spatially aliased ground roll; and E, 59, 62, and 64 Hz near offset noise. (b) Plot of calculated shot gather and f-κ domain located approximately on top of the chimney. (c) AWD shot gather 27 from Line 500 and F-K domain located approximately on top of the chimney, the same geometry as the calculated synthetic gather in panel (c). 16

1.6.4 Constant velocity stacks of Line 500 and Line 600. (a) 700 m/s constant velocity stack of Line 500. (b) 700 m/s constant velocity stack for Line 600. (c) 1200 m/s constant velocity stack for Line 500. (d) 1000 m/s constant velocity stack for Line 600. CMP, common midpoint. 18

1.6.5 (a) Model 1 is a control for both Lines. (b) Synthetic shot gathers calculated from Model 1. The purple star shows shot #1, the red star shows shot #27 and the blue star is shot #54. (c) Model 2 is the same as Model 1 with the inclusion of a linear high-V_P anomaly roughly the length of the anomaly in the inverted V_P model at ~30 m depth and a low-V_P anomaly representing the cavity beneath the spalled layer centered at 150 m in the first layer. (d) Synthetic shot gathers calculated from Model 2. The purple star shows shot #1, the red star shows shot #27 and the blue star is shot #54. (e) Model 3 is the same as Model 1 with the inclusion of a linear high-V_P anomaly roughly the length of the anomaly in the inverted V_P model at ~30 m depth, a low-V_P anomaly representing the cavity beneath the spalled layer centered at ~150 m in the first layer, and a low-V_P anomaly centered at 400 m depth in the second layer. (f) Synthetic shot gathers calculated from Model 3. The purple star shows shot #1, the red star shows shot #27, and the blue star is shot #54. Line 500 and Line 600 analog models are identical except for the addition of the extra low-V_P anomaly. 20

1.7.1 Slices through the 3-D tomographic model. (a) Line 500 tomogram with colormap optimized for the region above the chimney. The black star marks the depth of burial. (b) Line 600 tomogram with colormap optimized for the region above the chimney. (c) Line 500 tomogram with colormap optimized for the region around the detonation point. (d) Line 600 tomogram with colormap optimized for the region around the detonation point. 23

1.7.2 Checkerboard test with ±20% perturbation and ray coverage plots. (a) Line 500 checkerboard test result using 200 x 50 m blocks. The stars mark the depth of burial. (b) Line 600 checkerboard test result using 200 x 50 m blocks. (c) Line 500 checkerboard test result using 50 x 25 m blocks. (d) Line 600 checkerboard test result using 50 x 25 m blocks. (e) Ray coverage plot for Line 500. (f) Ray coverage plot for Line 600. 25

1.7.3 Line 500 and 600 migrated sections. (a) Line 500 seismic image. (b) Line 600 seismic image. (c) Interpreted Line 500 seismic image. (d) Interpreted Line 600 seismic image. The yellow line represents the spalled layer, the red ellipse denotes the void, the green line marks the alluvium-tuff contact, and the blue line marks the vitric non welded tuff (VNT)-zeolitic nonwelded tuff (ZNT) contact. (e) Line 500 tomogram with colormap optimized for the region above the chimney overlaid on Line 500 seismic image. (f) Line 600 tomogram with colormap optimized for the region above the chimney overlaid on Line 600 seismic image. (g) Line 500 tomogram with colormap optimized for the region around the detonation point overlaid on Line 500 seismic image. (h) Line 600 tomogram with colormap optimized for the region around the detonation point overlaid on Line 600 seismic image. The white star marks the detonation point. 26

1.7.4 Images of stacked synthetic section after normal-moveout correction and migration. (a) Control for both lines (Model 1) stacked section showing the alluvium-tuff reflector at 0.4 s and VNT-ZNT contact at 0.7 s. (b) Synthetic stack of Line 500 (Model 2) showing the spall surface at 0.1 s, the void between the peaks of the two diffraction hyperbolas at ∼0.3 s and ∼0.4 s, the alluvium-tuff contact at ∼0.4 s and the VNT-ZNT contact at ∼0.7 s. (c) Synthetic stack of Line 600 (Model 3) showing the spall surface at 0.1 s, the void between the peaks of the two diffraction hyperbolas at ∼0.3 s and ∼0.4 s, the additional low-V_P anomaly between the hyperbolas peaks at ∼0.5 s and 0.65s, the alluvium-tuff contact at ∼0.4 s and the VNT-ZNT contact at ∼0.7 s. (d) Model 1 migrated section showing the alluvium-tuff reflector at ∼300 m and VNT-ZNT contact at ∼600 m depth. (e) Migrated synthetic stack of Line 500 (Model 2) showing the spall surface at ∼30 m, the void at ∼200 m, the alluvium-tuff contact at 300 m and the VNT-ZNT contact at ∼600 m. (f) Migrated synthetic stack of Line 600 (Model 3) showing the spall surface at ∼30 m, the void at ∼200 m, the additional low-V_P anomaly centered at ∼400 m, the alluvium-tuff contact at 300 m and the VNT-ZNT contact at ∼600 m. 27

1.A.1 Legacy seismic profile (LANL-80-6) near HADDOCK (L. Prothro, written comm., 2018). (a) The entire seismic line. The purple letter A marks the beginning of the line while the purple letter B marks the end of the seismic line. (b) A subset of the seismic line (X to X') showing the prominent basin reflectors near HADDOCK lie with the 0.4–1.2 s window. 45

1.A.2 Average spectra plots. (a) The green curve is the average spectra of the raw Seismic Hammer field data. The blue curve is the average spectra of the raw Accelerated Weight Drop field data. (b) Average spectra of the Accelerated Weight Drop field data after applying different ground-roll removal filters. The blue curve represents the average spectra of the raw data. The cyan curve is the average spectra of the f-κ filtered data. The magenta curve is the average spectra of the low-frequency array filtered (LFAF) data. The red curve is the average spectra of the ground roll adaptive noise (GRAN) filtered data. 46

1.A.3 Final stacking velocities for Line 500 and Line 600. (a) Stacking velocity model for Line 500. (b) Stacking velocity model for Line 600. (c) Unmigrated stack of Line 500. (d) Unmigrated stack of Line 600. 47

2.2.1 Study area. (a) Shaded topographic map and faults of southern Alaska and the Kodiak Islands region. MOOS array (blue triangles), BEAAR array (green triangles), WVLF array (Orange triangles). (b) Geology map of the Kodiak Islands region. Refer to Wilson et al. (2015) for geologic unit explanation. (c) Shaded topographic map of the study area. (d) Schematic diagrams depicting scenarios for Kodiak Island formation and deformation. (i) Modified from Paterson and Sample (1988) illustrates the duplex accretion and underplating scenario. (ii) Modified from Tsuji et al. (2014) illustrates the splay faulting scenario. 50

2.4.1 Receiver function profiles. (a) Stacked radial receiver functions with a Gaussian value of 2.5 (∼1.2 Hz). (b) ∼1.2 Hz CCP image for transect A-B. Note the clear lack of a low-velocity channel at the plate interface (Red = Positive, Blue = Negative). For reference, we plotted earthquakes from the AACSE catalog (black dots), the top-of-slab depth from Hayes et al. (2018) (blue dashes), and an inferred Moho surface (red dashes) assuming an 8-km thick oceanic crust. Vertical exaggeration = 0.135. (c) Stacked radial receiver functions with a Gaussian value of 5.0 (∼2.4 Hz). Stack1, Stack2 and Stack3 show the locations of the receiver functions stacked and plotted in Figure 3 to compare with synthetics. (d) ∼2.4 Hz CCP image for transect A-B. Note the clear lack of a low-velocity channel at the plate interface. . 56

2.5.1 Synthetic tests. Each set of 3 plots represents synthetic modeling results (black dashed lines) overlaid on stacked field RFs (red lines) centered at 10 km (top), 22 km (middle) and 3 km (bottom), field RF uncertainties are plotted as black dashed lines. The right column contains the velocity models used to calculate the synthetic RFs on the left. (a) Model 1 is analogous to the Kenai observations by Kim et al. (2014). (b) Model 2 has no LVZ above the subduction slab. (c) Model 3 is the best-fitting model, it only contains the slab Moho. . . 59

2.A.1 (a) Back azimuthal distribution of teleseismic events >5.0 MW within the 30° – 90° distance window, occurring between May 23, 2019, and June 17, 2019. (b) Location of the 7 events selected for receiver function calculation. (c) Record section plot of one of the events used for receiver function calculation after instrument response removal, and a bandpass filter (0.2-2 Hz). Amplitudes normalized with each trace. This M_W6.3 occurred on 04 June 2019, 04:39:17 UTC at ∼430 km depth southeast of Honshu, Japan. 76

2.A.2 Comparison of near co-located nodal and broadband station waveforms. (a) Plots of node station 3001 and broadband station KD02 vertical, east, north component recordings of the 04 June 2019, 04:39:17 UTC Event shown in Appendix 2.A Figure 2.A.1 part c. (b) Plot of the average radial receiver functions for stations KD02, KD01, KS03 and KD00 calculated by Z. Li et al., (2020) projected onto transect AB (top). Plot of the average radial receiver functions calculated from near-colocated nodal station 3001, 9218, 2056 and 9033 projected onto transect AB. 77

2.A.3 Map of piercing points (black stars) at 20 km depth, and the stations (red inverted triangles) used for common conversion point stacking. The grey rectangles show the position of all the profile boxes used in the stacking. 78

2.A.4 (a) Synthetic tests of 2.5 Hz Ps RFs for models with different LVZ thicknesses. The vertical light blue rectangles in the left panel mark the position of the negative conversion for the 4-km thick LVZ in the top seismogram. The blue lines are synthetic waveforms, and the red dashed lines are the averages of the standard deviations of the field data from Figure 2.5.1. (b) Moveout-corrected radial receiver functions with a Gaussian value of 10 (∼4.8 Hz) stacked by common conversion point. 79

3.2.1 USGS earthquake locations of events M>3 in the Raton Basin. (a) Location of events occurring between January 01, 1970 and January 01, 1999. (b) Location of events occurring between January 01, 1999 and January 01, 2022. (c) Cross section of transect A-A'. Top of the Dakota formation (green dashed line) and top of the Precambrian basement (magenta dashed line) modified from Weingarten (2015) plotted for reference. The top of Precambrian basement estimated from Mooney and Kaban (2010) (cyan dashed line) is also plotted for comparison. Note the ∼2km difference in the predicted basement depths on western end of the transect. 83

3.2.2 Shaded relief map of the Raton Basin in New Mexico and Colorado and the study area. 84

3.2.3 Composite map of the geology and structural geology of the Raton Basin region. New Mexico geology from the Bureau of Geology and Mineral Resources (2003) and Colorado geology from Tweto (1979). See references for geologic unit explanation. 85

3.3.1 Mooney & Kaban (2010)'s sedimentary thickness estimates and broadband station locations. (a) Black dashed lines are B-B', C-C', D-D' profile location that are near the broadband array stations and also gives an ideas of basin structure. (b) Cross-sections of profiles B-B', C-C' and D-D' shown in (a). 87

3.3.2 Modified from Applegate & Rose (1985). Seismic correlation chart for the northern Raton Basin. Notice that the top of Trinidad and top of Dakota reflectors are more clearly defined than the Precambrian basement. See Figure 3.4.10 for the complete 2D seismic profile. . . . 88

3.4.1 Plot showing time windows used to calculate the signal-to-noise ratio. 90

3.4.2 Comparison of co-located nodal station (4E.95) and broadband station (YX.UNM4) recordings of the June 02, 2018, 11:53:09 UTC Samoa Islands region event after preprocessing. A bandpass filter (0.5–2.0 Hz) has been applied to these waveforms. 92

3.4.3 Average moveout corrected radial-component receiver function traces. (a) 1, 2.5 and 5 Hz receiver functions for broadband station UNM4 receiver functions. (b) 1, 2.5 and 5 Hz receiver functions for nodal geophone station 95. 93

3.4.4 Example of epicentral (EPI) gathers showing interpreted top of Dakota and Moho signals at different frequencies. (a) R-component of gathers from UNM6. (b) R-component of gathers from UNM7. 94

3.4.5 Example of back-azimuth plot of 2.5 Hz R- and T-component receiver functions. Note the coherent positive conversion on the R-component at $\sim$0.5 s. 95

3.4.6 H-κ stacking results for UNM4 and 95. (a) Plot of the H-κ search space for UNM4 with the maximum values indicated with a white x. (b) UNM4's 2.5 Hz radial receiver functions used in the stack sorted by the slowness. Magenta lines show the moveout curves for the best estimates of the phase arrivals from H-κ stacking. (c) Plot of the H-κ search space for nodal station 95. (d) Station 95's 2.5 Hz Radial receiver functions. 96

3.4.7 Comparison of H-κ stacking results with well data. (a) Map showing broadband array, near co-located injection wells. (b) Cross-sections of profiles shown in (a). Mooney & Kaban (2010)'s top of the Precambrian basement (cyan dashed line). Wang et al. (2020) relocated catalog (black dots). Magenta circles with error bars are H-κ stacking results from this study and green circles are the top of the Dakota calculated from the elevation of the known top of Dakota formation from the wells onsite. 97

3.4.8 Compilation of basin-wide top-of-Dakota depth measurements. Circles are depths from wells, triangles are depths estimated by the broadband array and the squares are depths estimated by the nodal array. Black circles are earthquakes detected by Wang et al., (2020). 98

3.4.9 Zoomed-in area in Figure 3.4.8 above. Events, wells and seismometers between latitude 36.95°and 37.0° are projected to transect E-E'. Events, wells and seismometers between latitude 36.78° and 36.925°are projected to transect F-F'. Top of Dakota (brown dashed lines) inferred from the mean of the wells and seismometer estimates that are projected to the line. Top of basement (red dashed lines) inferred assuming a cumulative thickness of 1.438 km (e.g., Weingarten, 2015) for all the layer between the top of Dakota and the top of basement. . 99

3.4.10 Modified from Applegate and Rose (1985). Legacy seismic line for the northern Raton Basin. Magenta triangle marks the location of S16 on the line. 100

3.A.1 Distribution of M>5.5 seismic earthquakes used in the RF analysis for broadband seismometers. (a) Epicentral locations of events used for network YX, XP and TA respectively. (b) Back-azimuthal distribution of the selected earthquakes around the array. 110

3.A.2 Distribution of M>5.5 seismic earthquakes used in the RF analysis for broadband seismometers. (a) Epicentral locations of events used for network YX, XP and TA respectively. (b) Back-azimuthal distribution of the selected earthquakes around the array. 111

List of Tables

1.5.1 Recording information for the Seismic Hammer and Accelerated Weight Drop (AWD) 8
1.6.1 Forward modeling parameters 19

2.B.1 Events used in this study 80
2.B.2 One-Dimensional model parameters 80

3.3.1 Summary of broadband array and number of events used in analysis . 89
3.4.1 List of injection wells used in this study. Highlighted wells were used for groundtruthing 91
3.5.1 H-k stacking results for the broadband array 102
3.6.1 Modified from Weingarten (2015). Thickness of formations below top-of-Dakota and above top-of-basement. 105

1 Dense Seismic Array study of a Legacy Underground Nuclear Test at the Nevada National Security Site

Authors and Affiliations

Evans A. Onyango[1*]
Robert E. Abbott[2]
Lindsay L. Worthington[1]
Leiph A. Preston[2]

[1]Dept. of Earth and Planetary Sciences, University of New Mexico, Albuquerque, New Mexico, USA
[2]Sandia National Laboratories, Albuquerque, New Mexico, USA
[*]Corresponding author

Modified from a manuscript published in *Bulletin of the Seismological Society of America*

1.1 Abstract

The complex post-detonation geologic structures that form after an underground nuclear explosion are hard to constrain because increased heterogeneity around the damage zone affects seismic waves that propagate through the explosion site. Generally, a vertical rubble-filled structure known as a chimney is formed after an underground nuclear explosion that is composed of debris that falls into the subsurface cavity generated by the explosion. Compared with chimneys that collapse fully, leaving a surface crater, partially collapsed chimneys can have remnant subsurface cavities left in place above collapsed rubble. The 1964 nuclear test HADDOCK, conducted at the Nevada test site (now the Nevada National

Security Site), formed a partially collapsed chimney with no surface crater. Understanding the subsurface structure of these features has significant national security applications, such as aiding the study of suspected underground nuclear explosions under a treaty verification. In this study, we investigated the subsurface architecture of the HADDOCK legacy nuclear test using hybrid 2D–3D active source seismic reflection and refraction data. The seismic data were acquired using 275 survey shots from the Seismic Hammer (a 13,000 kg weight drop) and 65 survey shots from a smaller accelerated weight drop, both recorded by $\sim$ three-component 5 Hz geophones. First-arrival, P-wave tomographic modeling shows a low-velocity anomaly at $\sim$200 m depth, likely an air-filled cavity caused by partial collapse of the rock column into the temporary post-detonation cavity. A high-velocity anomaly between 20 and 60 m depth represents spall-related compaction of the shallow alluvium. Hints of low velocities are also present near the burial depth ($\sim$364 m). The reflection seismic data show a prominent subhorizontal reflector at $\sim$300 m depth, a short-curved reflector at $\sim$200 m, and a high-amplitude reflector at $\sim$50 m depth. Comparisons of the reflection sections to synthetic data and borehole stratigraphy suggest that these features correspond to the alluvium–tuff contact, the partial collapse cavity, and the spalled layer, respectively.

1.2 Introduction and Motivation

The Nevada National Security Site (NNSS) is home to many of the United States' historic nuclear tests. More than 650 underground nuclear tests were conducted in the Yucca Flat basin (Figure 1.2.1a) between 1951 and 1992 (*Springer*, 2002). The HADDOCK nuclear test in this basin was conducted in 1964 at 364 m below ground surface with an announced yield of “less than 20 kilotons” (*DOE*, 2000). Unlike the great majority of nuclear tests in Yucca Flat, HADDOCK did not form a collapse crater on the surface and has little to no surface expression. To understand the lateral and vertical changes resulting from underground nuclear tests at the NNSS, several geophysical techniques such as borehole and electromagnetic surveys have been used to successfully characterize the subsurface (*Keiswetter and Won*, 1997; *Sweetkind et al.*, 2007). The FREY experiment, described in this article, tests the ability of seismic reflection and refraction methods to image underground nuclear explosion features. We acquired ∼6 km of hybrid 2D–3D seismic data in April 2017 (*Abbott et al.*, 2017) to image the post-detonation subsurface structure of the HADDOCK nuclear test (Figure 1.2.1). The study was motivated by three objectives: (1) to determine the feasibility of seismically imaging partial collapse and chimney structures, (2) to acquire ground truth for modeling the effects on seismic waves propagating through existing collapse structures, and (3) to acquire ground truth for modeling the coseismic effects on regional and teleseismic recordings of nuclear explosions caused by damage and spallation.

The phenomenology associated with deep underground nuclear explosions is unique to these kinds of explosions, and the fundamental processes that accompany them are generally the same from a few microseconds after detonation to the formation of the chimney (*Carothers*, 1995; *Eisler and Chilton*, 1964; *Germain and Kahn*, 1968; *Glasstone and Dolan*, 1977; *Hakala*, 1970; *Higgins*, 1970; *Vincent et al.*, 2011). Residual surface features associated with contained underground nuclear explosions are also well documented (*Allen et al.*, 1997; *Grasso*, 2000, 2003), but literature on underground nuclear explosions that have little or no surface manifestation is scarce. Results from this study could elucidate the enigmatic structure of contained explosions that have minimal surface expression. Our findings can be applied to the study of suspected underground nuclear explosions under a treaty verification or other multilateral agreement. The unique nuclear collapse structure could also be used to discriminate anomalies associated with natural phenomena such as earthquakes.

Starting in 2010, the Source Physics Experiment (SPE) program performed a series of chemical explosive tests at the NNSS to study the generation and propagation of seismic waves (*Snelson et al.*, 2013) and provide data for improving models for detecting and characterizing underground explosions (*Ford and Walter*, 2013). SPE Phase I (Figure 1.2.1a,1.2.1b) sampled the Climax stock, an amalgamation of Cretaceous age quartz-monzonite and granodiorite that intrudes sedimentary rocks of Paleozoic and Precambrian age (*Maldonado*, 1977; *Townsend and Obi*, 2015). SPE Phase II was conducted in the alluvium of the Yucca Flat sedimentary basin (*Townsend and Obi*, 2015) to understand the differences in explosion-source phenomenology between granitic rock and alluvium and update existing explosion-source ground-motion modeling codes (*Chen et al.*, 2017). Because Yucca Flat is heavily populated with previous nuclear tests in close proximity, a better understanding of seismic-wave interactions at these structures is needed to properly model seismic-wave propagation. *Toney et al.* (2019) concluded that seismic scattering induced by high-contrast seismic-wave velocity anomalies corresponding to nuclear test chimneys inhibited the formation of coherent surface waves, thus compromising S wave and P-wave/S-wave velocity ratio (V_P/V_S) models. *Toney et al.* (2019) were focused on basin-wide structure and as a consequence, their study and lower resolution than the current effort, which isolates a single collapse structure with denser spatial sampling of the subsurface.

Secondary seismic signals created by damage and spallation at the time of the explosion can influence seismic motion recorded at regional or teleseismic distances (*Day and McLaughlin*, 1991; *Patton and Taylor*, 1995; *Schlittenhardt*, 1991; *Taylor and Randall*, 1989). Spallation, in particular, is important to infrasound monitoring of underground explosions (*Jones et al.*, 1993, 2015; *Poppeliers et al.*, 2019). Explosion-induced spall is formed when the shock wave traveling outward and upward following detonation is reflected back when it reaches the surface forcing the

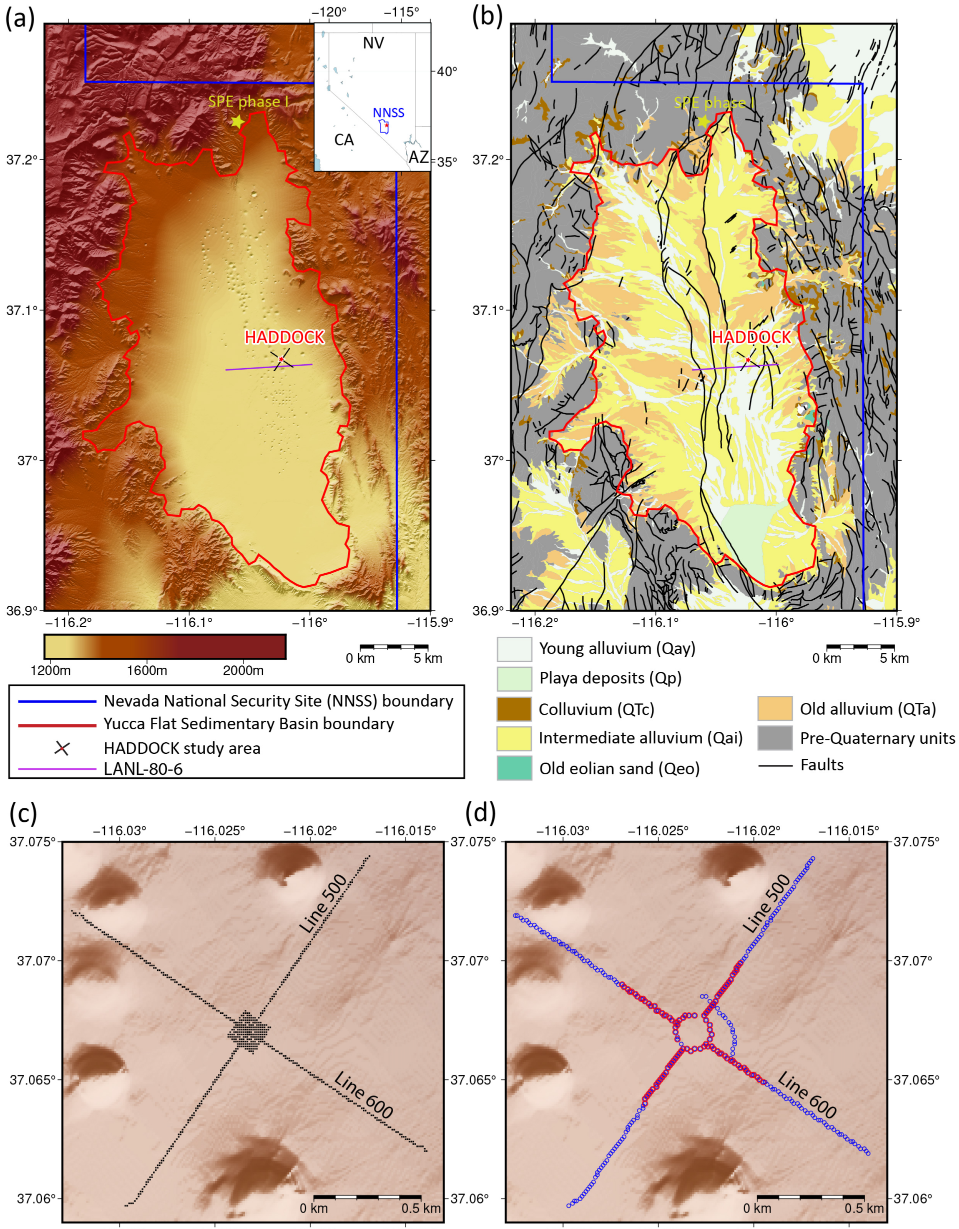
(a)
(b)
(c)
(d)
NV
CA
AZ
NNSS
SPE phase I
HADDOCK
–120°
–115°
40°
35°
37.2°
37.1°
37°
36.9°
–116.2°
–116.1°
–116°
–115.9°
1200m
1600m
2000m
0 km
5 km
Nevada National Security Site (NNSS) boundary
Yucca Flat Sedimentary Basin boundary
HADDOCK study area
LANL-80-6
Young alluvium (Qay)
Playa deposits (Qp)
Colluvium (QTc)
Intermediate alluvium (Qai)
Old eolian sand (Qeo)
Old alluvium (QTa)
Pre-Quaternary units
Faults
–116.03°
–116.025°
–116.02°
–116.015°
37.075°
37.07°
37.065°
37.06°
Line 500
Line 600
0 km
0.5 km

Figure 1.2.1: (a) Shaded topographic map of the Yucca Flat region of the Nevada National Security Site (NNSS). The blue line marks the NNSS boundary. The red line marks the Yucca Flat sedimentary basin boundary. The FREY experiment's Line 500 and Line 600 are shown as the black X. The purple line marks the location of the legacy seismic line LANL-80-6. Subsidence sinks formed from legacy nuclear testing dominate the eastern side of the basin. (b) Quaternary geology of Yucca Flat Basin (Slate et al., 2000). Refer to Slate et al. (2000) for geologic unit explanation. (c) Shaded relief image showing receiver geometry of the FREY experiment. The black dots mark the positions of the geophones. (d) Shaded relief image showing shot geometry of the experiment. Blue circles are shot locations of the Seismic Hammer. Red circles mark the positions of the P/S 100 Accelerated Weight Drop (AWD) shots. Inset is a map of Nevada showing the location of the NNSS and the Yucca Flat.

ground to split off into subhorizontal layers (*Eisler and Chilton*, 1964; *Glasstone and Dolan*, 1977; *Merkle*, 1980). Spallation can potentially change the calculated magnitude of the explosion, change the phase of outgoing seismic waves, and lengthen the source time function of the recorded event, complicating nuclear explosion monitoring worldwide (*Rygg*, 1979; *Stump*, 1985). Constraints on the depth and lateral extent of surface spall and detonation point damage would aid in the understanding of these phenomena and, consequently, the monitoring effort.

1.3 Geological Setting

The Yucca Flat basin lies within a zone of east-west basin and range extension posited to have occurred primarily during the Tertiary period (*Drellack et al.*, 2010; *Hudson et al.*, 1994; *Proffett Jr*, 1977). The basin extends roughly along a north–south axis, with Paleozoic carbonate rocks defining the basement (*Connor et al.*, 2000). Yucca Flat is bounded by normal faults and contains north-south striking intrabasinal faults (*Minor*, 1995, Figure 1.2.1b). Tertiary volcanic tuff and Quaternary alluvium overlie the Paleozoic basement (Figure 1.2.1b). In the deepest part of the basin, unconsolidated alluvium and volcanic deposits are >2 km thick according to models combining gravity modeling, seismic studies, and borehole mapping (*Phelps et al.*, 2011; *Schramm et al.*; *Toney et al.*, 2019). Ground-water studies estimate the water table at ∼400–500 m (*Fenelon*, 2005).

HADDOCK's emplacement hole stratigraphy highlights three different stratigraphic units: Quaternary alluvium (0–283.5 m thick), bedded or nonwelded Rainier Mesa tuff or tuff of Holmes Road (54.9 m thick), and bedded undifferentiated tuff (>32.0 m thick) (*DOE*, 2000, M. Townsend, written comm., 2016). The NNSS 3D geologic framework model (*Prothro et al.*, 2016) breaks Yucca Flat's tertiary tuffs into four units. Zeolitic nonwelded tuff consists of nonwelded to partially welded zeolitic tuff atop the Paleozoic basement. The zeolitic nonwelded tuff is overlain by lower welded tuff, which is partially to densely welded ash-flow tuff. Poorly fractured vitric nonwelded tuff overlies the lower welded tuff, and upper welded tuff consisting of devitrified welded tuff overlies the vitric nonwelded tuff. The nonuniform distribution of the four tuff units within the basin contributes to changes in V_P, bulk density and porosity throughout the basin. The HADDOCK study area only has vitric nonwelded tuff and zeolitic nonwelded tuff between Quaternary alluvium and Paleozoic basement. Vitric nonwelded tuff includes all stratigraphic units from the base of welded Rainier Mesa tuff to the top of zeolitic nonwelded tuff, and the zeolitic nonwelded tuff includes all stratigraphic units from the base of welded Topopah Spring tuff to the top of the Paleozoic basement (*Prothro et al.*, 2016).

1.4 Background and Previous Work

The FREY experiment was one of a recent series of data acquisition campaigns in Yucca Flat using large numbers (≥1000) of seismic instruments to study shallow seismic structure and wave propagation in the NNSS (*Chen et al.*, 2017; *Mellors et al.*, 2018; *Toney et al.*, 2019). Prior to FREY, the THOR 1 and THOR 2 2D surveys were designed to define basin-wide P- and S-wave velocities of Yucca Flat (*Finlay et al.*, 2015; *Tang et al.*, 2015; *Toney et al.*, 2019). THOR 1 and THOR 2 recorded ∼147 shots on >350 geophones (variable spacing) along transects totaling 30 km. Legacy 2D seismic lines (Appendix 1.A Figure 1.A.1) across Yucca Flat, primarily taken in the 1970s and 1980s, show reflectors with a discontinuous, chaotic character on the near-surface underlain by prominent, continuous reflectors between 0.4 and 1.2 s (*Hudson et al.*, 1983, L. Prothro, written comm., 2018). These legacy seismic records also show the continuous reflectors offset by what appear to be faults.

Other seismic studies of the post-detonation structures at the NNSS have failed to constrain the subsurface architecture of the resultant chimney near nuclear tests.

Cogbill and Taylor (1994) performed a high-frequency (40-Hz geophones) seismic reflection survey before and after the DIVIDER underground nuclear test in the Yucca Flat to image the resultant spalled layer. Shot gathers lacked obvious, coherent reflectors in both pre- and post-event surveys. The study attributed the failure to image the spalled layer to the difficulty in imaging coherent reflections, which is typical of Yucca Flat seismic surveys. *Miller and Steeples* (1992) also conducted a shallow, high-frequency seismic reflection survey before and after the BEXAR underground test on Pahute Mesa on the NNSS. This study also failed to image the spalled layer or any other explosion-related structure. Among other recommendations, the study suggested that spall detection research involving reflection seismology should focus on tests that were detonated at 2–3 km away from ground zero of any previous nuclear tests to avoid disruption to the host geology by previous tests (*Miller and Steeples*, 1992).

1.5 Data

Parameter	Seismic Hammer	US Alliance P/S 100 AWD
Number of hits per shot	10	5
Shot interval	15 m	15 m
Line 500 receiver interval	5 m	5 m
Line 600 receiver interval	5 m	5 m
Line 500 length	2 km	2 km
Line 600 length	2 km	2 km
Number of 3D grid lines	14	14
Length of each 3D grid line	140 m	140 m
3D grid inline spacing	10 m	10 m
3D grid crossline spacing	10 m	10 m
Record length	9000 ms	4000 ms
Time sampling interval	0.5 ms	0.5 ms
Number of time samples per trace	18000 samples	8000 samples
Data format	SEG-Y	SEG-Y

Table 1.5.1: Recording information for the Seismic Hammer and Accelerated Weight Drop (AWD)

Seismic data for this study were acquired in the Yucca Flat basin as part of the FREY experiment run by Sandia National Laboratories and coordinated by the Desert Research Institute and the NNSS. About 6 km of hybrid 2D and 3D seismic data were acquired above the HADDOCK test site by 998 PS-5R geophones. These three-component 5 Hz geophones have a high sensitivity (83 V/m/s) compared with conventional geophones and a low wave distortion ($\leq 0.2\%$). The 2D geometry consisted of two 2 km long orthogonal lines (line 500 and line 600), each with 401 receivers at 5 m spacing. The 3D portion of the experiment was a dense grid of fourteen 140 m long lines directly over HADDOCK ground zero, with inline and crossline spacing of 10 m (Figure 1.2.1c).

Two seismic sources were used for this experiment (Figure 1.2.1d). About 275 shots were recorded from the seismic hammer (*Hampshire and O'Donnell*, 2013) (Table 1.5.1) and 65 shots from a smaller US Alliance P/S 100 accelerated weight drop (AWD) (Table 1.5.1). The seismic hammer is a customized industrial pile driver that hydraulically hoists a 13,000 kg mass to 1.5 m height and then drops the mass onto a 1.8 m diameter metal strike plate. At its highest point, the potential energy of this system is 0.19 MJ (*Toney et al.*, 2019). Approximately 10 shots were acquired per shot location. Generally, we used the eighth shot per location because it required ∼8 hits before the ground was driven to refusal (*Lee and Abbott*, 2017). The dominant frequencies of the raw seismic hammer data ranged from 0 to 40 Hz (Appendix 1.A Figure 1.A.2a), making these data useful for body-wave tomography and deep seismic reflection imaging. Here, we used the seismic hammer data (Figure 1.5.1a) to estimate V_P by inverting first-arrival picks (Figure 1.5.1b, 1.5.1c) recorded by all the receivers in the survey.

Unlike the seismic hammer, in which the mass's acceleration downward is due solely to gravity, the AWD uses a nitrogen spring to drive its mass downward. The AWD's adjustable nitrogen pressure ranges from 2964 to 13,789 kPa, yielding an accelerated impact energy between ∼400 and ∼1550 J. Although the low-frequency output of the seismic hammer is useful for deep reflection imaging and body-wave tomography, the AWD's broadly higher-frequency output (Appendix 1.A Figure 1.A.2a) is useful for shallow reflection imaging.

Similar to other active seismic data collected in Yucca Flat (*Cogbill and Taylor*, 1994; *Sexton et al.*, 2013; *Toney et al.*, 2019), the raw shot gathers are dominated by surface waves (Figure 1.6.1). A consistent narrowband (59–64 Hz) noise peak was present in the near-offset traces. Incoherent noise was observed throughout the 0–100 Hz band. Four days of the eight-day AWD data collection period occurred during unusually high winds, degrading the signal-to-noise ratio of that data. Average atmospheric conditions characterized the seismic hammer collection.

1.6 Methods

1.6.1 Tomographic inversion

We estimated HADDOCK's V_P distribution by inverting first-arrival picks on the Seismic Hammer 2D and 3D datasets. Clear onsets of P arrivals were picked from seismic data that were first gained (automatic gain control 0.5 s window) and then band-pass filtered (5–10–40–50 Hz) with a zero phase, sine squared tapered filter (Figure 1.5.1). The band-pass filter adequately attenuated low-frequency pseudo random noise and high-frequency coherent noise from powerlines and machinery but did not eliminate the coherent preshot signal recorded before the true first arrival. The preshot signal in the seismic hammer data is due to elastic rebound in the earth caused by unloading of the 13,000 kg mass in free fall. The true first arrival due to impact is recorded ∼0.5 s later (*Lee and Abbott*, 2017; *Toney et al.*, 2019) (Figure 1.5.1a). All arrival times were picked manually, making sure to avoid dead seismograms and seismograms of which P arrivals may have been distorted in any

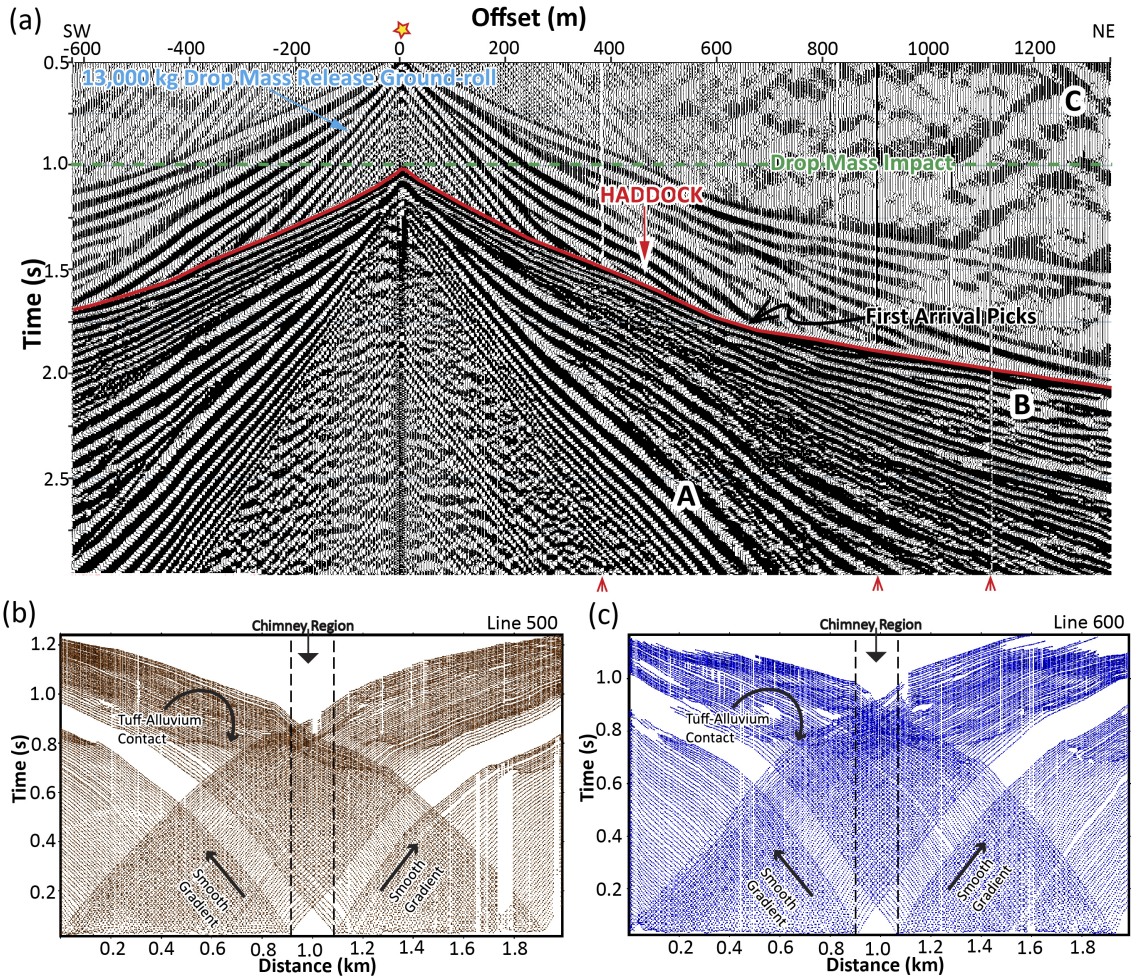

Figure 1.5.1: (a) Shows raw Seismic Hammer shot number 43 on Line 500. The red line shows first arrival picks and the red arrows at the bottom of the record indicate bad traces. The phase labeled A is the ground-roll, B are reflections plus noise and C is the pre-shot noise. (b) Plot of first arrivals of shots on Line 500. (c) Plot of first arrival picks of shots on Line 600.

way. Our final dataset contained ∼109,600 picks from Line 500, ∼109,500 picks from Line 600, and ∼30,900 picks from the shorter lines at the center of the array. The picking accuracy is estimated to be 0.004–0.01 s.

The complex structure of the HADDOCK site is evident from composite travel-time curve plots (Figure 1.5.1b; 1.5.1c), which show lateral variation in the chimney region: shallow travel-time gradients characterize the shallow depths (<80 m) and steep gradients characterize the deeper section (<250 m). Abrupt changes in the

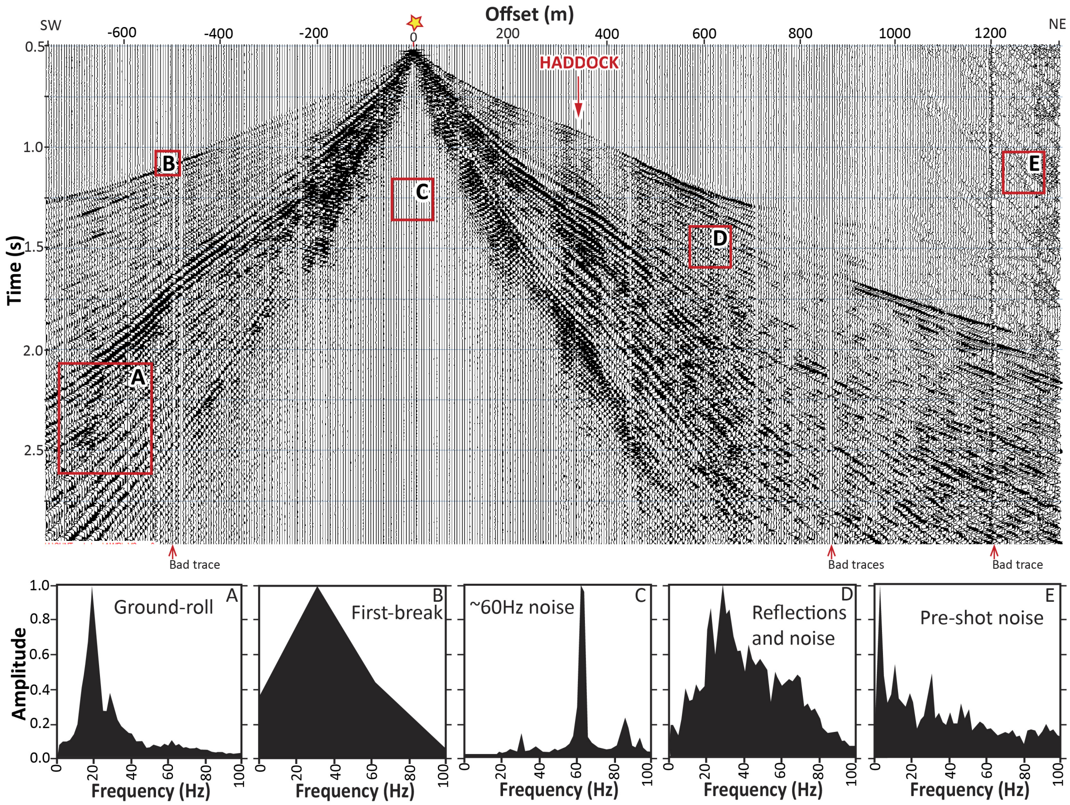

Figure 1.6.1: AWD Inline shot 43 Line 500 shot gather (top) and the normalized average amplitude spectra for the regions in the red rectangles (bottom). (A) ground-roll, (B) first-break, (C) 59–64 Hz near offset noise, (D) reflection contaminated with noise, (E) pre-shot noise.

travel-time gradient across the line also indicate a possible change in lithology, for example, alluvium–vitric nonwelded tuff contact at ∼0.8 s. We used the Sandia-developed code, called “tomog,” to estimate a smooth V_P model. Tomog is a 3D ray-based (eikonal solver) P-wave travel-time tomographic program (*Preston et al.*, 2003). We used a nonlinear inversion procedure that iteratively solves for the 3D V_P distribution from P-wave travel times (*Preston et al.*, 2007), implementing the full 3D raytracing and travel-time calculations through the Vidale–Hole algorithm (*Hole and Zelt*, 1995).

1.6.2 2D seismic reflection processing and imaging

We processed the AWD field data using the open-source Seismic Unix software, the Echos module from the commercial software Paradigm 15, and commercial software Visual-Seismic UNIX for Windows (SUNT) (Figure 1.6.2). Because there were ∼5 hits per AWD shot location, we used diversity stacking on the duplicate field records to suppress bursts of noise caused by high winds (*Klemperer*, 1987). Field geometry was edited in the header file followed by static correction. Both Line 500 and Line 600 were acquired along a relatively flat area. Elevation ranged from 1234.9 to 1266.6 m on Line 500 and from 1244.3 to 1251.0 m on Line 600. Thus, the gradients from the lowest to the highest point are ∼0.02 (2% slope) for line 500 and ∼0.003 (0.3% slope) for Line 600. We used first-arrival alignment static correction in which picked first breaks are aligned along a laterally interpolated velocity function (*Pugin and Pullan*, 2000). Remaining static irregularities were addressed later by applying residual statics corrections after normal moveout. Trace editing of the entire dataset involved entirely muting dead, clipped, or anomalous amplitude seismograms to minimize introduction of artifacts on final stacked images. To compensate for the decay of signal amplitude with increasing distance, we applied gain to the data (*Yilmaz*, 2001). We found a 0.5 s time-window sufficient for gain correction.

Initial data processing involved spectrum analysis of the seismic data to characterize the frequency content of the data. The average spectrum of the raw dataset showed that the data were dominated by a low-frequency signature (0–3 Hz), and a narrow band of high-frequency (∼59–64 Hz) noise from the diesel generator was used to drive the nitrogen spring and the powerlines in the vicinity (Appendix 1.A Figure 1.A.2a) Selected shot gathers were then displayed and the spectra of different arrivals plotted (Figure 1.6.1) to better characterize the frequency content of the data. Inspection of these frequency spectra showed that surface waves dominate

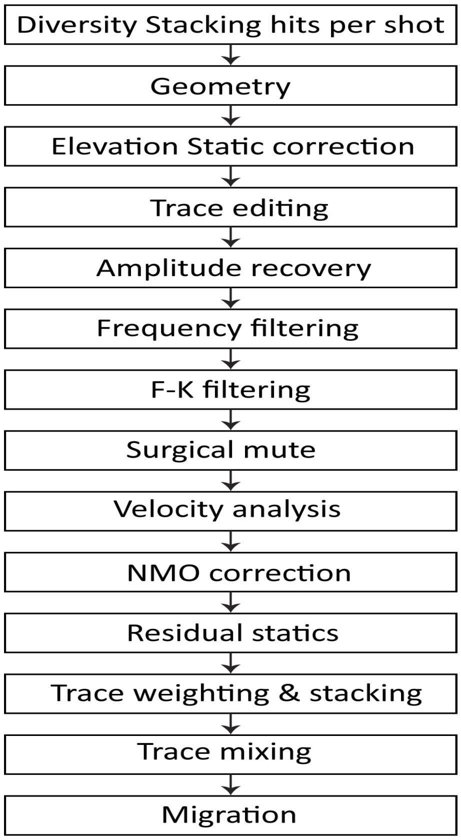
Diversity Stacking hits per shot
Geometry
Elevation Static correction
Trace editing
Amplitude recovery
Frequency filtering
F-K filtering
Surgical mute
Velocity analysis
NMO correction
Residual statics
Trace weighting & stacking
Trace mixing
Migration

Figure 1.6.2: Field data processing workflow.

frequencies between 10 and 40 Hz, first breaks are centered between a wideband of frequencies between 0 and 60 Hz, and near-offset machinery noise dominated a narrowband of frequencies centered between 59 and 64 Hz. Preshot noise is represented by a broadband of frequencies between 0 and 100 Hz with the most dominant of this signature centered between 0 and 10 Hz. The preshot noise is recorded right before the nitrogen spring pushes the AWD mass into the ground. Suspected reflections fall within a wide range of frequencies between 0 and 100 Hz, peaking at ∼30 Hz. No useful signal can be seen beyond 100 Hz. Informed by the frequency spectrum analysis, we applied a band-pass filter (10–20–50–70 Hz) as preliminary noise reduction to allow for better identification of signal and noise. The selected band-pass filter was kept wide to avoid attenuating useful signal. We also kept the slope of the high-cut side of the filter gentle to prevent frequency aliasing (*Yilmaz*, 2001).

Because frequency filtering did not successfully eliminate coherent noise such as ground roll, we explored different methods of coherent noise reduction, including frequency–wavenumber (f-κ) filtering (*Dobrin and Savit*, 1988), ground-roll adaptive noise (GRAN) filtering (*Farhang-Boroujeny*, 1999), and low-frequency array filtering (LFAF; *Oppenheim and Schafer*, 1975). In GRAN filtering, the assumption is that the vertical-component records both signal (S) and noise (Nv). It is also assumed that the radial-component records noise (Nr), which is uncorrelated with signal S but correlates to some extent with the noise Nv. The noise Nr is filtered such that the output (Y) is a close replica of Nv, and then Y is subtracted from the vertical component (*Farhang-Boroujeny*, 1999; *Widrow and Stearns*, 1985). GRAN filtering removed some of the ground-roll phases but failed to eliminate the first break and noise with frequencies >58 Hz (Appendix 1.A Figure 1.A.2b). It is possible that GRAN filtering failed because the wavefield's interaction with the explosion site is such that the resultant Nr has very little correlation with Nv.

The LFAF method attenuates surface-wave noise via low-frequency array forming. We convolved each frequency component within a specified noise frequency band with a boxcar corresponding to the effective array length calculated from surface-wave velocity and seismogram spatial distance (*Oppenheim and Schafer*, 1975; *Oppenheim et al.*, 1989; *Robinson and Treitel*, 2000). Not only did LFAF fail to attenuate the ground-roll and the near-offset noise, but it also degraded the overall frequency content of the gathers (Appendix 1.A Figure 1.A.2b).

Although f-κ filtering has the potential to introduce artifacts, we found f-κ filtering to be the most effective method for attenuating linear noise from these data. In the f-κ domain, coherent linear noise and spatially aliased ground roll (~30–50 Hz) were

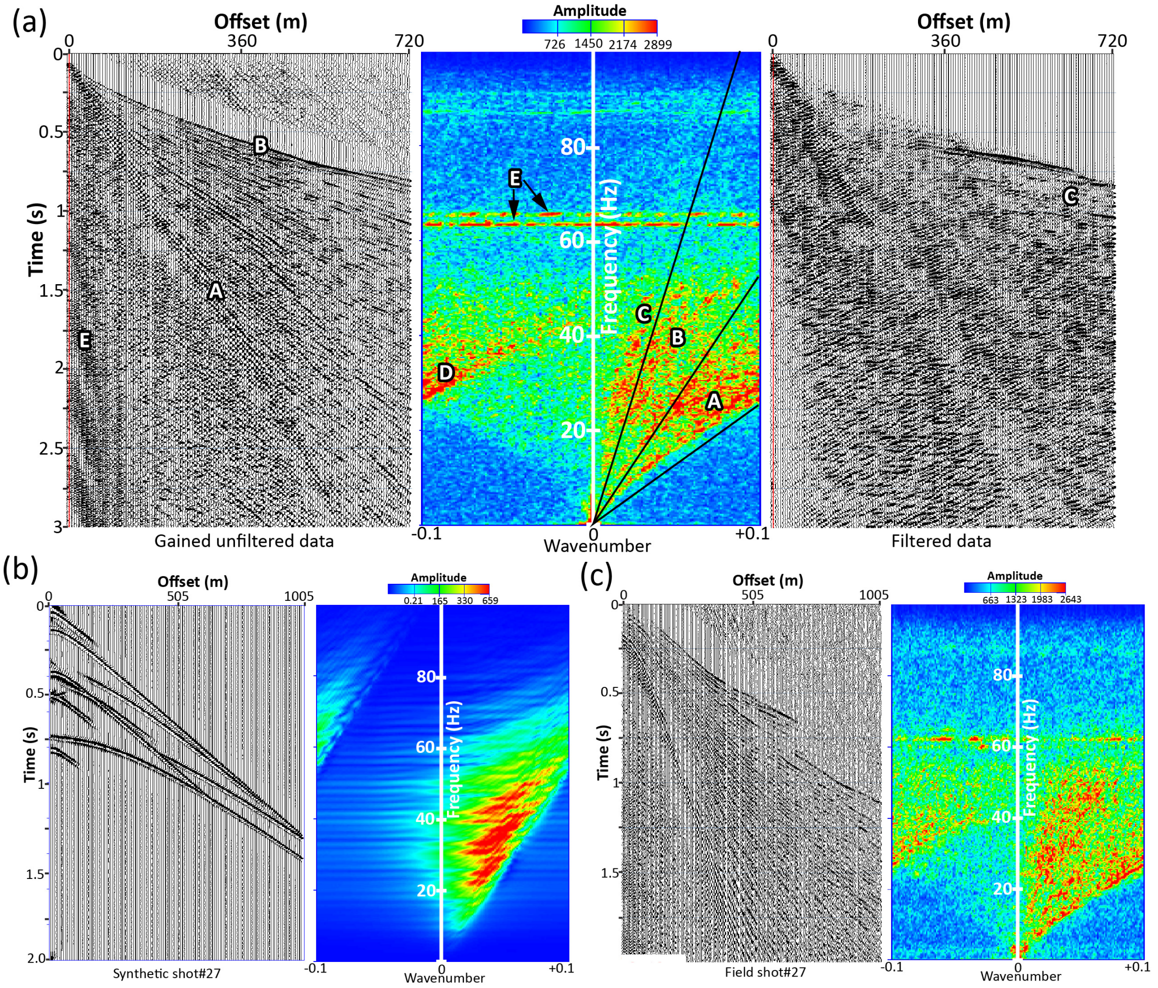

Figure 1.6.3: Selected AWD shot gathers in time and frequency-wavenumber (f-κ) domain. (a) f-κ filtering of AWD inline shot gather 93 Line 500 (positive offset). (Left) Gained (automatic gain control 0.5 s window) unfiltered data in the time domain, (center) f-κ domain, and (right) f-κ filtered data in time domain. The arrivals are labeled as follows: A, ground-roll; B, first break; C, reflections; D, spatially aliased ground roll; and E, 59, 62, and 64 Hz near offset noise. (b) Plot of calculated shot gather and f-κ domain located approximately on top of the chimney. (c) AWD shot gather 27 from Line 500 and F-K domain located approximately on top of the chimney, the same geometry as the calculated synthetic gather in panel (c).

easily identifiable (*Dobrin and Savit*, 1988, Figure 1.6.3). We plotted different shot gathers along both Line 500 and Line 600 field data in the f-κ domain; however, backscattered energy was not clearly visible. In this study, we used f-κ dip filtering to denoise the data by rejecting the entire left side of the f-κ space to remove any aliased signal and backscatter (*Yilmaz*, 2001). We also use an f-κ dip filter to remove coherent ground roll from the right side of the f-κ space. The f-κ filtering successfully rejected most of the coherent noise and revealed reflections but potentially eliminated 50% or more of scattering diffractions.

We applied careful surgical mutes to sorted common midpoint (CMP) gathers to remove the first-arrival phases, which when stacked would lead to the wrong interpretation (*Büker et al.*, 1998). Additional muting was applied after normal moveout correction to eliminate the effect of moveout stretching, which can severely distort shallow reflections at far offsets (*Yilmaz*, 2001).

Semblance analysis and velocity scans were not very effective for these data because they lacked obvious coherent reflection hyperbolas. We estimated stacking velocities from the analysis of constant velocity stacks (Figure 1.6.4). Constant stacking velocities that revealed coherent structures for both Lines 500 and 600 ranged from 700 to 1200 m/s. The final variable velocity models used to moveout Line 500 and Line 600 are derived from the constant velocity stacks (Appendix 1.A Figure 1.A.3).

We computed and applied residual statics prior to creating each stack and then applied the average refraction statics after stacking. In addition, we weighted far offset traces more than near offset prior to stacking because reflections were more visible at middle and far offsets compared with the near offset. Finally, we improved the stack section with a broadband bandpass filter and trace mixing before performing a 2D poststack Kirchhoff depth migration.

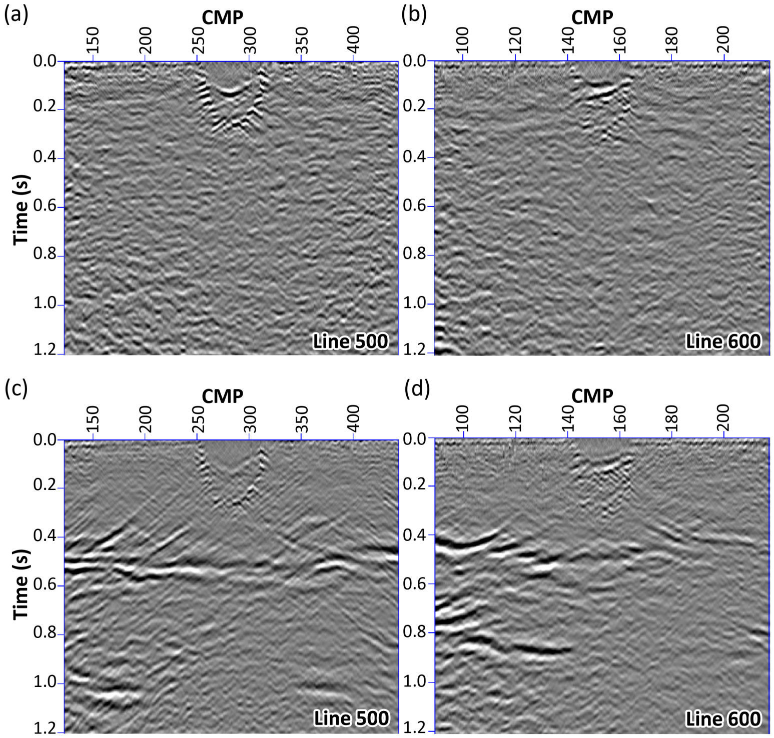

Figure 1.6.4: Constant velocity stacks of Line 500 and Line 600. (a) 700 m/s constant velocity stack of Line 500. (b) 700 m/s constant velocity stack for Line 600. (c) 1200 m/s constant velocity stack for Line 500. (d) 1000 m/s constant velocity stack for Line 600. CMP, common midpoint.

1.6.3 Forward modeling

The goals of forward modeling were to create a simplified geometry of the geology of the test area, create synthetic test data in the same configuration as the FREY experiment geometry, and produce a final image that would be useful for interpreting first-order features that might be observed in the final seismic image from the FREY field dataset. We modified the workflow and code from seismic reflection imaging of underground cavity examples presented by *Mellors* (2011). Using P-wave velocities, natural-state bulk densities, and depths (for alluvium–vitric nonwelded tuff contact and vitric nonwelded tuff–zeolitic nonwelded tuff contact) from the NNSS's 3D geologic framework (*Prothro et al.*, 2016), we built three geologic models with triangular elements. Two simplified geologic models derived from these data were used as analogs of the HADDOCK test, and a laterally homogeneous model was used as a control for both lines.

Layer	**Vp(km/s)**	**Sloth(1/Vp)^2**	**Density (g/cm^3)**	**Top Depth (km)**
Alluvium	1.601	0.3901	1.91	0.000
Spalled layer	1.750	0.3265	2.00	0.030
Void	0.700	2.0408	1.40	0.113
Vitric nonwelded tuff	1.937	0.2665	1.65	0.300
Low-V_P anomaly	0.700	2.0408	1.40	0.357
Zeolitic nonwelded tuff	2.430	0.1693	1.83	0.600

Table 1.6.1: Forward modeling parameters

The physical property values (Table 1.6.1) used in model building are all unit averages from the 3D geologic framework (*Prothro et al.*, 2016). Alluvium V_P used in the models is 1601 m/s, and the natural bulk density used for alluvium is 1.91 g/cm^3. We used a V_P of 1937 m/s and a density of 1.65 g/cm^3 for the vitric nonwelded tuff. Finally, we used a zeolitic nonwelded tuff V_P of 2430 m/s and a density of 1.83 g/cm^3.

Model 1, consisting of three homogeneous and isotropic layers (Table 1.6.1; Figure 1.6.5), was the control for the two lines. Model 2 (Table 1.6.1; Figure 1.6.5) was also three-layered, but the first layer included a linear high-V_P anomaly at 30 m depth (representing spall compaction) at the center of the model and a low-V_P anomaly (representing the residual cavity) centered at 155 m depth. We inferred the relative locations of the anomalies from preliminary results of the tomographic inversion. Model 3, the analog for Line 600 (Table 1.6.1; Figure 1.6.5), included a linear high-V_P anomaly (representing spall compaction) at 30 m depth at the center of the model, a low-V_P anomaly (representing the residual cavity) beneath the spalled layer centered at 155 m depth, and an additional low-V_P anomaly centered at 400 m depth. The defined layers were filled with triangles of "sloth" in which sloth $= 1/(V_P)^2$ (*Forel et al.*, 2005) and the density values derived from the 3D geologic framework. We approximated the densities of the spalled layer and the void using

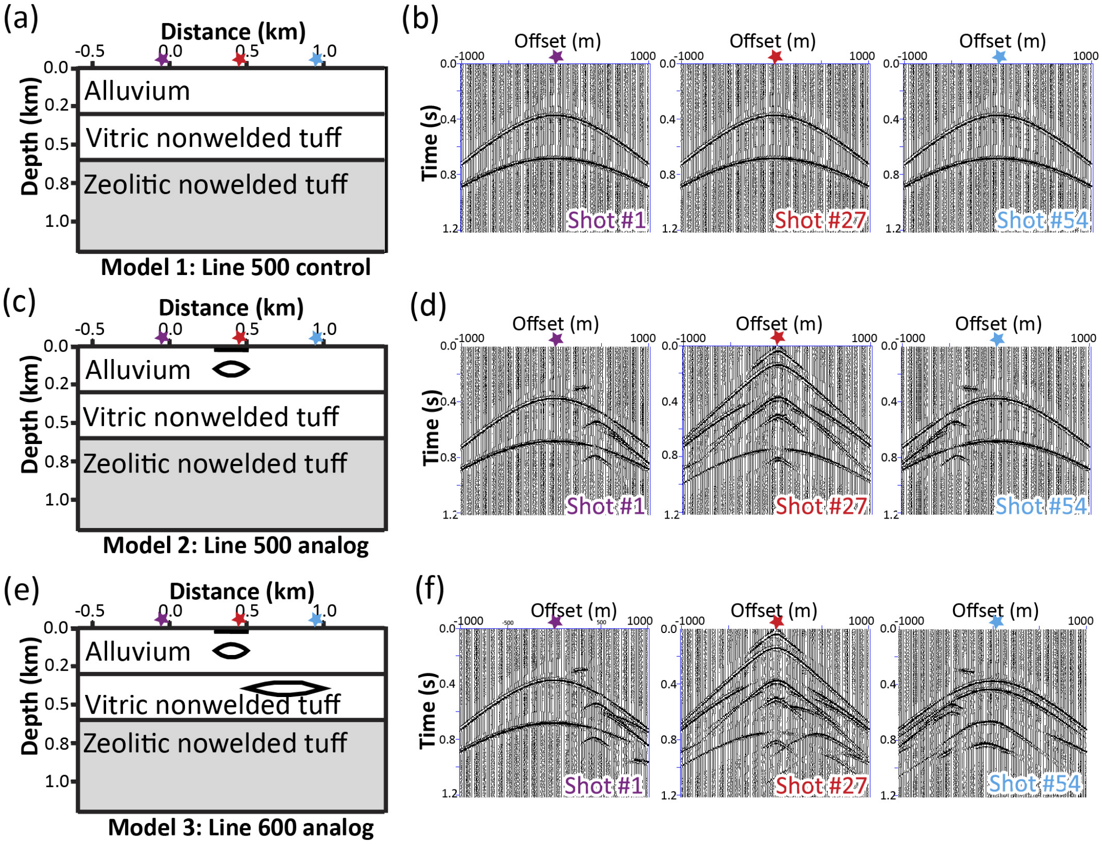

Figure 1.6.5: (a) Model 1 is a control for both Lines. (b) Synthetic shot gathers calculated from Model 1. The purple star shows shot #1, the red star shows shot #27 and the blue star is shot #54. (c) Model 2 is the same as Model 1 with the inclusion of a linear high-V_P anomaly roughly the length of the anomaly in the inverted V_P model at ∼30 m depth and a low-V_P anomaly representing the cavity beneath the spalled layer centered at 150 m in the first layer. (d) Synthetic shot gathers calculated from Model 2. The purple star shows shot #1, the red star shows shot #27 and the blue star is shot #54. (e) Model 3 is the same as Model 1 with the inclusion of a linear high-V_P anomaly roughly the length of the anomaly in the inverted V_P model at ∼30 m depth, a low-V_P anomaly representing the cavity beneath the spalled layer centered at ∼150 m in the first layer, and a low-V_P anomaly centered at 400 m depth in the second layer. (f) Synthetic shot gathers calculated from Model 3. The purple star shows shot #1, the red star shows shot #27, and the blue star is shot #54. Line 500 and Line 600 analog models are identical except for the addition of the extra low-V_P anomaly.

the Gardner's density–velocity relation: $\rho = \alpha V_P^{\beta}$ where is bulk density in g/cm^3, V_P is in m/s, coefficient (α) = 0.31 and exponent (β) = 0.25 (*Gardner et al.*, 1974).

We generated Gaussian beam synthetic seismograms for the sloth models using the triseis algorithm from Seismic Unix. A Gaussian beam is a high-frequency asymptotic time-harmonic solution of the wave equation, with a bell-shaped (Gaussian) amplitude profile around the central ray (*Červen and Pšenčík*, 1983; *Liu*, 2010). Kinematic and dynamic raytracing through the models is implemented efficiently because the models' cross-sections are subdivided into triangles, and in each triangle the ray path is part of a circle (*Muller*, 1984). Raytracing then becomes a matter of determining the intersection of an arbitrary triangle with an arbitrary circle as discussed by *Muller* (1984) and *Červen and Pšenčík* (1983). In the FREY study, we calculated synthetic seismic data from the sloth models in a split-spread geometry with 268 geophones and 54 shot points. The receiver spacing was 15 m. Figure 1.6.5b, 1.6.5d and 1.6.5f shows the first, middle, and last shots, respectively, calculated from the models. One significant limitation of these calculations is that they are acoustic only and therefore do not include the surface waves observed in the data and lack random noise. Thus, they are idealized and certainly represent the best-case scenario and overestimate the ability of the data to image the model structures. Still, simple modeling as done in this study is straightforward and sufficiently simulates reflected phases needed for reflection imaging.

Because the idealized synthetic data did not contain coherent noise such as surface waves and random-noise contaminants such as bursts of wind, no f-κ or band-pass filtering was performed on the data. To process the synthetic seismic data, we first sorted the shot gathers to CMP gathers and then performed constant velocity scans to estimate the velocity fields for each line. We then corrected for normal moveout accompanied by a stretch mute to eliminate the artifacts associated with normal moveout corrections at far offsets and then stacked the data. Finally, we performed 2D poststack Kirchhoff migration (*Yilmaz*, 2001) on the resultant stacks to form an image approximating the subsurface reflectivity.

1.7 Results

1.7.1 Tomographic inversion

Tomographic inversion results show a high-V_P anomaly between 20–60 m depth and a low-V_P anomaly at ∼200 m depth, which is likely the residual cavity on both Line 500 and Line 600 (Figure 1.7.1a; 1.7.1b). The tomography results show a prominent but poorly resolved low-V_P anomaly primarily below the detonation point (∼364 m) on both lines (Figure 1.7.1c; 1.7.1d).

The V_P change at ∼0.1 km depth on Line 600 highlights a significant difference between the two lines. The V_P transition at this depth is less abrupt on Line 500 than on Line 600 (Figure 1.7.1a; 1.7.1b), suggesting that nearby underground nuclear tests (see craters in Figure 1.2.1) may have affected the structure along Line 600 above the alluvium–tuff contact. The V_P range above 250 m depth is between 400–1500 m/s and is 1500–2500 m/s between 250 and 400 m depth.

Checkerboard tests using 200 × 50 m and 50 × 25 m blocks with ±20% perturbations, which is the expected minimum perturbation for the target cavities (*Hoots et al.*, 2020; *Toney et al.*, 2019), demonstrate excellent recovery at both scales down to the top of the shallow low-V_P anomaly in the central portion of the model and to somewhat greater depths on either side of this anomaly (Figure 1.7.2a-d). Below ∼200 m depth, model resolution degrades but is still useful for the larger blocks down to 300–350 m, especially in the central portion of the model. Below this depth, resolution rapidly degrades with only partial recovery and smearing of the checkerboard blocks. Overall, Line 500 shows better resolution over a larger lateral extent than does Line 600, best recovery of which is predominately located near the center of the line.

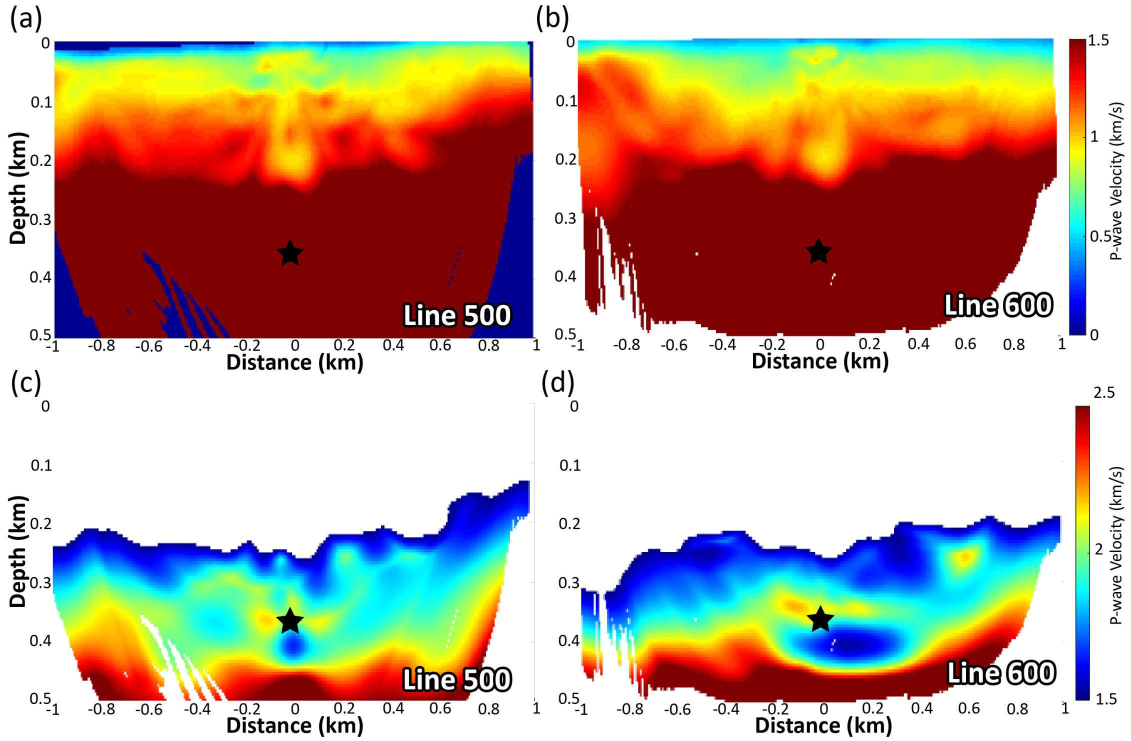

Figure 1.7.1: Slices through the 3-D tomographic model. (a) Line 500 tomogram with colormap optimized for the region above the chimney. The black star marks the depth of burial. (b) Line 600 tomogram with colormap optimized for the region above the chimney. (c) Line 500 tomogram with colormap optimized for the region around the detonation point. (d) Line 600 tomogram with colormap optimized for the region around the detonation point.

These checkerboard resolution images are closely related to ray-path density plots (Figure 1.7.2e and 1.7.2f). The highest densities of ray paths are located above ∼200 m. The effects of the low-V_P zones are clearly visible in these plots. Shadow zones of low ray-path density are coincident with both the shallow and deep low-V_P zones. Ray paths become focused between the two low-V_P zones. Thus, we would expect poorer resolvability within the low-V_P zones themselves relative to surrounding structure. Based on checkerboard and ray-path densities, the deeper low-velocity anomaly near the detonation point is especially poorly resolved in location, extent, and recovered velocities.

1.7.2 2D seismic reflection processing and imaging

The migrated stacked seismic sections show a short high-amplitude reflector at ~50 m depth, which we interpret to be the spalled layer (Figure 1.7.3a-d). The void locations, highlighted by the red ellipses in Figure 1.7.3c and Figure 1.7.3d, are not clearly identifiable on the seismic sections, but they become clearer when the tomograms are overlaid on the seismic sections (Figure 1.7.3e; 1.7.3f). There are also high-amplitude, continuous linear reflectors at ~300 m for both Lines 500 and 600 (Figure 1.7.3c and Figure 1.7.3d). This reflector correlates to borehole U-3dl stratigraphy, which places the depth to the base of alluvium at 283.3 m (*DOE*, 2000, M. Townsend, written comm., 2016). We interpret this reflector to be the alluvium–vitric nonwelded tuff contact. We interpret the second strong discontinuous reflector located at ~600 m on Line 500 to be the vitric nonwelded tuff–zeolitic contact. This contact is not as clear on Line 600 compared with Line 500 perhaps because of the three nearby tests on the northwest side of the line (Figure 1.2.1c; 1.2.1d).

1.7.3 Forward modeling

All synthetic shot gathers of the control experiment (model 1) have only the alluvium–tuff reflection and the vitric nonwelded tuff–zeolitic nonwelded tuff reflection. For both Line 500 (model 2) and Line 600 (model 3) analog models, cavity diffractions are the earliest arrivals at far offsets (Figure 1.6.5d; 1.6.5f), whereas the spall surface reflection is the earliest arrivals closer to middle of the line (Figure 1.6.5d; 1.6.5f). Diffraction peaks mark the location of the residual cavity

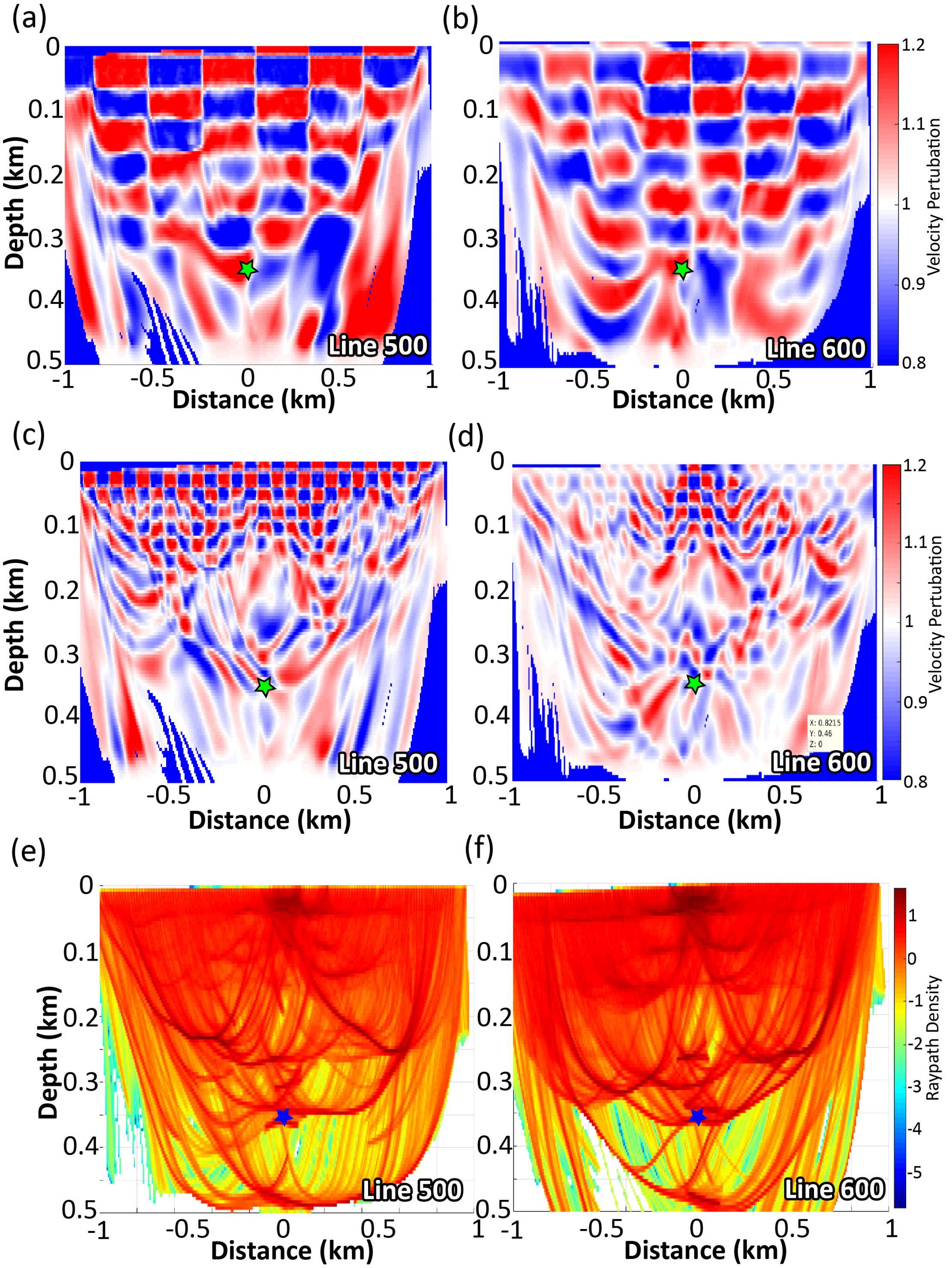

Figure 1.7.2: Checkerboard test with ±20% perturbation and ray coverage plots. (a) Line 500 checkerboard test result using 200 x 50 m blocks. The stars mark the depth of burial. (b) Line 600 checkerboard test result using 200 x 50 m blocks. (c) Line 500 checkerboard test result using 50 x 25 m blocks. (d) Line 600 checkerboard test result using 50 x 25 m blocks. (e) Ray coverage plot for Line 500. (f) Ray coverage plot for Line 600.

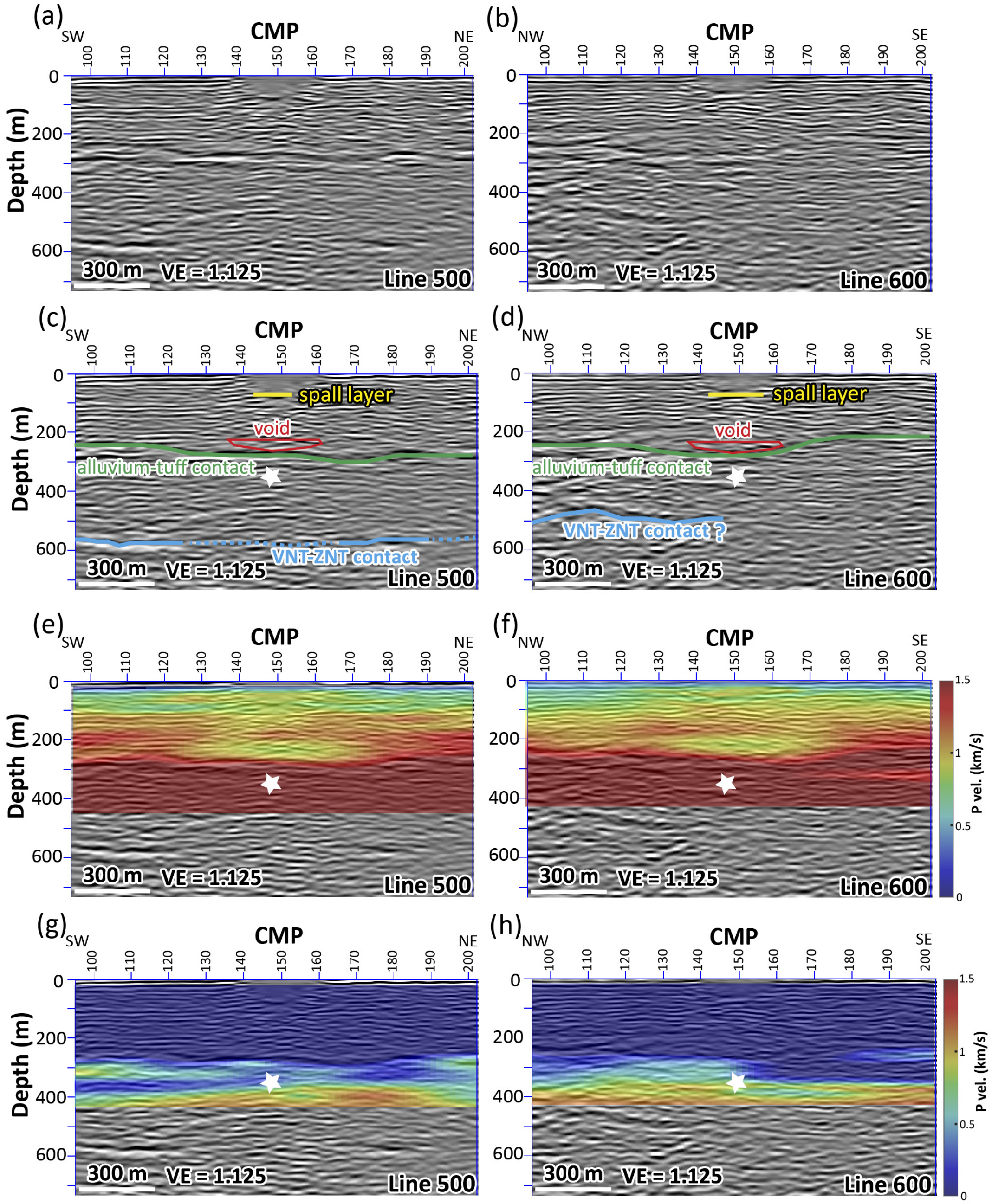

Figure 1.7.3: Line 500 and 600 migrated sections. (a) Line 500 seismic image. (b) Line 600 seismic image. (c) Interpreted Line 500 seismic image. (d) Interpreted Line 600 seismic image. The yellow line represents the spalled layer, the red ellipse denotes the void, the green line marks the alluvium-tuff contact, and the blue line marks the vitric non welded tuff (VNT)-zeolitic nonwelded tuff (ZNT) contact. (e) Line 500 tomogram with colormap optimized for the region above the chimney overlaid on Line 500 seismic image. (f) Line 600 tomogram with colormap optimized for the region above the chimney overlaid on Line 600 seismic image. (g) Line 500 tomogram with colormap optimized for the region around the detonation point overlaid on Line 500 seismic image. (h) Line 600 tomogram with colormap optimized for the region around the detonation point overlaid on Line 600 seismic image. The white star marks the detonation point.

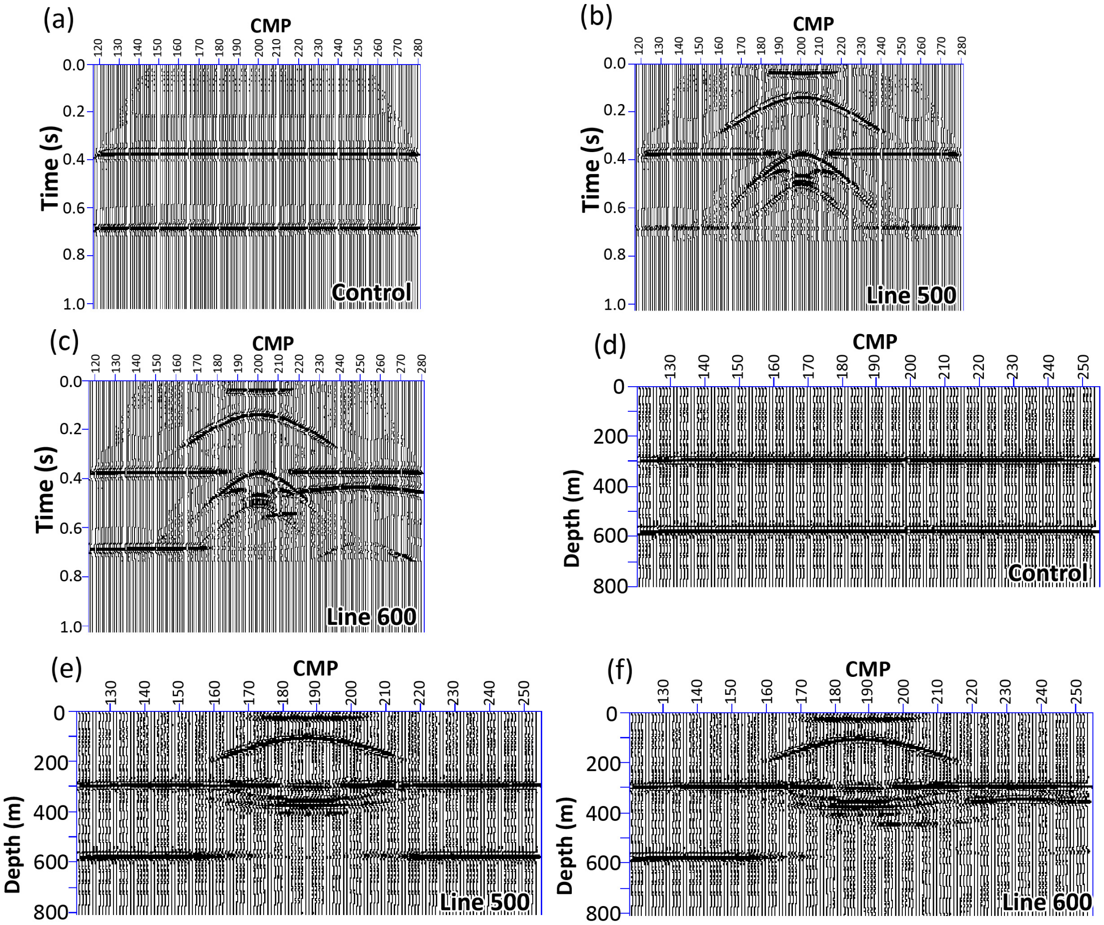

Figure 1.7.4: Images of stacked synthetic section after normal-moveout correction and migration. (a) Control for both lines (Model 1) stacked section showing the alluvium-tuff reflector at 0.4 s and VNT-ZNT contact at 0.7 s. (b) Synthetic stack of Line 500 (Model 2) showing the spall surface at 0.1 s, the void between the peaks of the two diffraction hyperbolas at ∼0.3 s and ∼0.4 s, the alluvium-tuff contact at ∼0.4 s and the VNT-ZNT contact at ∼0.7 s. (c) Synthetic stack of Line 600 (Model 3) showing the spall surface at 0.1 s, the void between the peaks of the two diffraction hyperbolas at ∼0.3 s and ∼0.4 s, the additional low-V_P anomaly between the hyperbolas peaks at ∼0.5 s and 0.65s, the alluvium-tuff contact at ∼0.4 s and the VNT-ZNT contact at ∼0.7 s. (d) Model 1 migrated section showing the alluvium-tuff reflector at ∼300 m and VNT-ZNT contact at ∼600 m depth. (e) Migrated synthetic stack of Line 500 (Model 2) showing the spall surface at ∼30 m, the void at ∼200 m, the alluvium-tuff contact at 300 m and the VNT-ZNT contact at ∼600 m. (f) Migrated synthetic stack of Line 600 (Model 3) showing the spall surface at ∼30 m, the void at ∼200 m, the additional low-V_P anomaly centered at ∼400 m, the alluvium-tuff contact at 300 m and the VNT-ZNT contact at ∼600 m.

and low-V_P anomaly. These signals are reflected from more than one layer and are recorded as diffraction multiples below the expected low-V_P anomaly positions.

It is notable that the vitric nonwelded tuff–zeolitic nonwelded tuff contact in models 2 and 3 is not as continuous as the vitric nonwelded tuff–zeolitic nonwelded tuff contact for model 1, perhaps the result of shadowing caused by the void anomaly. This effect can be observed in the unmigrated stacked sections following normal moveout correction (Figure 1.7.4b; 1.7.4c), which clearly show the extent of the diffraction hyperbolas and their multiples. The shadowing leads to weak reflections within the lateral extent of the lower hyperbola. Still, both the control (model 1) and the analog for Line 500 (model 2) migrated sections clearly show reflectors at 300 m depth (alluvium–tuff contact) and at 600 m depth (vitric nonwelded tuff–zeolitic nonwelded tuff contact) (Figure 1.7.4d; 1.7.4e). The spall surface contact is located at ∼30 m depth, and the void below it is located at ∼200 m depth.

In addition to observing the alluvium–tuff contact, vitric nonwelded tuff–zeolitic nonwelded tuff contact, spall surface, and the void on the Line 600's forward model 3 (Figure 1.7.4f), an additional ellipsoidal feature, the result of adding the low-V_P anomaly centered at ∼400 m, can be observed beneath the alluvium–tuff contact. This feature obscures about a third of the vitric nonwelded tuff–zeolitic nonwelded tuff contact beneath it. The total amount of shadowing caused by the upper void and this low-V_P anomaly effectively renders more than half of the vitric nonwelded tuff–zeolitic nonwelded tuff surface invisible.

1.8 Discussion

1.8.1 Limitations of seismic imaging

In suitable settings, seismic reflection imaging is a powerful tool for the characterization of near-surface geology. However, coherent unwanted waves such as ground-coupled airwaves and ground roll can present a challenge for shallow seismic surveys compared with deeper surveys partly because the low V_P/V_S of dry unconsolidated overburden ensures a small "optimum window" in which reflections are separated from surface waves (*Hunter et al.*, 1984). In addition to being situated in dry Quaternary alluvium, the HADDOCK test site is laterally heterogenous, and the stratigraphic layering is disturbed around the damage zone.

There has been limited success seismically detecting voids and tunnels because the presence of these features even in ideal geological conditions lead to difficulties associated with distinguishing void reflections or diffractions from ground roll and refractions (*Miller and Steeples*, 1991; *Sloan et al.*, 2015; *Tricot et al.*, 1987). This challenge is also evident in the HADDOCK data. Despite knowing the precise location of the HADDOCK chimney, a qualitative analysis of the raw shot gathers shows no clear reflection or diffraction hyperbola from the void even though the elastic properties of the residual air-filled void and the ambient rocks should provide a large impedance contrast. In fact, apart from the ground roll (A in Figure 1.6.1), first break (B in Figure 1.6.1), and the near-offset noise (C in Figure 1.6.1), the seismic data are essentially a mixture of refraction arrivals, scattering, and diffuse reflections. Literature searches for direct void and tunnel detection using seismic reflection acquisition return few examples of successful surveys, most of which use anomalously high frequencies obtained from atypical seismic sources and ultra-high-pass frequency filtering (*Hunter et al.*, 1984; *Jongerius and Helbig*, 1988). Rapid attenuation of these high frequencies with depth has been cited as one reason for the lack of successful examples of direct detection of void and tunnels below 50 m (*Steeples et al.*, 1997). The obscuring or degeneration of reflections by voids or tunnels is another reason direct void and tunnel detection has not been successful. As a result, researchers have surmised that the absence of continuous reflectors could indicate the presence of a void (*Miller and Steeples*, 1991).

The FREY study corroborates and augments our current understanding of indirect and direct void detection at depths >50 m. Model 2's unmigrated stacked section (Figure 1.7.4b) shows diffraction hyperbolas at the suspected void location, and the vitric nonwelded tuff–zeolitic nonwelded tuff reflector is faded directly below it (Figure 1.7.4b at ∼0.7 s). In addition to the faded portion directly beneath the void, the vitric nonwelded tuff–zeolitic nonwelded tuff reflector of model 3 (Figure 1.7.4c at ∼0.7 s) is also missing the area directly beneath the second low-V_P anomaly. Therefore, the missing portions of the vitric nonwelded tuff–zeolitic nonwelded tuff contact on Line 600's migrated field data (Figure 1.7.4f) could indicate damage from nearby tests (Figure 1.7.1d; 1.7.3f; 1.7.3h). Therefore, although the missing middle part of the second reflector on Line 500's migrated field data (Figure 1.7.4e) can be attributed to attenuation caused by the void above it, nearby tests can explain why the left portion of this reflector is also missing on Line 600 migrated field data (Figure 1.7.4f) and perhaps why the left portion of the top reflector is attenuated. Although we successfully modeled the effect of the low-V_P anomalies on the vitric nonwelded tuff–zeolitic nonwelded tuff reflectors on both Lines 500 and 600, the detonation point at ∼364 m is in this vicinity, so the missing middle parts of the reflector could also be a manifestation of the lateral extent of the damage zone. We also note that Line 600 extends to a heavily damaged region by previous tests, which may also contribute to attenuation of the vitric nonwelded tuff–zeolitic nonwelded tuff reflector.

Borehole U-3dl data from the HADDOCK site places the alluvium and tuff contact at a depth of 283.5 m (*DOE*, 2000, M. Townsend, written comm., 2016), which agrees with our interpretation of the alluvium–vitric nonwelded tuff contact, which is undulating at ∼300 m (Figure 1.7.3a-h). The alluvium–tuff reflector at ∼300 m on the migrated Line 500 stacked section is not as adversely affected by the void as the vitric nonwelded tuff–zeolitic nonwelded tuff reflector at 600 m depth, perhaps because of the bulk properties of the materials below the void or the void's geometry. As observed in model 2's migrated section (Figure 1.7.4e), even though the alluvium–tuff reflector immediately below the void is obscured by the shadowing, the lower hyperbola spans the gap. A void sitting just above the reflective interface could generate a diffraction hyperbola that comingles with and spans the reflection. Moreover, the diffraction multiples (∼400 m depth) beneath the alluvium–vitric nonwelded tuff interface (Figure 1.7.4e; 1.7.4f) highlight the difficulties of differentiating actual reflection arrivals from multiples and/or diffractions in the field data especially for shots above the void anomaly (shot #27 on Figure 1.6.3b; 1.6.3c). Although we observed diffractions in the unmigrated stacked field data (Figure 1.6.4), for example, above 0.4 s along the U shape at the center of both lines, we were unable to interpret diffractions in the shot gathers even after comparing synthetic gathers with field data that share the same geometry in the f-κ domain (Figure 1.6.3b;1.6.3c). Therefore, the task of eliminating unwanted multiples and identifying diffractions in field data is almost impossible, given the geological conditions in this setting. Moreover, eliminating surface waves using f-κ filters also has the unintended consequence of eliminating diffractions. As a result, we observe fewer diffractions on the unmigrated sections (Figure 1.6.4).

1.8.2 Chimney structure

We interpret the low-V_P zone at ∼200 m to be the residual cavity on top the chimney after the partial collapse of the rock column into the temporary postdetonation cavity. The presence of a low-V_P subsurface void underneath a high-V_P spall-compaction region would form a nuclear explosion fingerprint that may help discriminate a suspect event from a natural earthquake (at least in cases in which deep alluvium overlies the nuclear test). The imaging of the low-V_P void in the case of HADDOCK is a hopeful sign that future attempts at other locations may image detonation chimneys. There is evidence that an explosion in a region with different geologic structure, for example, in hard rock as opposed to alluvium, would have a different character (*Mellors et al.*, 2018). For instance, spall damage in granite might result in velocity decrease, as opposed to velocity increase. Nevertheless, imaging of a void in hard rock would give evidence of an explosion. This, in addition to the lack of observation of an earthquake fault, either seen in fault reflections or offset stratigraphy, would be strong evidence for an underground explosion source.

The V_P contrast and extent of spall from our study can be of immediate use in creating models for seismic propagation for the SPE program or for propagation at other nuclear test sites. As noted by (*Taylor and Randall*, 1989), spall mass is an important parameter for modeling regional nuclear test seismograms. The depth and breadth of the spall anomaly seen in our reflection sections and V_P tomograms (Figure 1.7.1; 1.7.3), combined with the density of the alluvium, can be used as a preliminary estimate of the spall mass parameter.

The low-V_P anomaly near the HADDOCK detonation point (Figure 1.7.1c; 1.7.1d) is suggestive of cracking and damage in the volcanic tuff at that depth or of low-V_P rockfall filling the original cavity. It is, however, poorly resolved for this survey and cannot be ruled out as an artifact. It is unclear that this result is due to a lack of sensitivity at this depth or an insufficiently strong anomaly. A future study over a shallower test would likely prove to be more effective.

1.9 Conclusions

We conducted a hybrid 2D–3D controlled-source seismic survey at the NNSS in Yucca Flat, Nevada, with the goal of constraining the postdetonation structure of the HADDOCK chimney to (1) assist in future investigations over suspected nuclear tests, (2) support ongoing SPEs, and (3) support global nuclear explosion monitoring. The final stacked sections for Line 500 and Line 600, coupled with the forward models, suggest that a hybrid 2D–3D survey geometry can be a useful tool for investigations over suspected nuclear tests, particularly for constraining the depth and lateral position of spall surfaces and postdetonation cavities. The low-V_P anomaly at ∼200 m depth from the tomographic images and the discontinuous, chaotic seismic character at ∼250 m depth, along with the attenuated strong reflector at ∼600 m on the final Line 500 stack, strongly suggests the existence of a void left in place above the collapsed rubble. Finally, subsurface information from this survey can be used to constrain and improve models for other underground nuclear tests, aiding in the understanding of the SPE chemical explosions in the Yucca Flat basin, as well as global nuclear explosion monitoring.

1.10 Data and Resources

The FREY seismic data in this study were acquired by Sandia National Laboratories and coordinated by the Desert Research Institute, Mission Support and Test Services, LLC. The data were acquired by PS-5R geophones (https://www.sunfull.com/cp/html/?52.html, last accessed July 2020). An assembled dataset of the SEGY field data from both the Seismic Hammer and the AWD will be available via IRIS Data Services (https://doi.org/10.7914/SN/X3_2017). Plotting and analysis tools used Generic Mapping Tools (https://www.generic-mapping-tools.org/, last accessed March 2020;

Wessel et al., 2013), visual SUNT by W-Geosoft (http://www.wgeosoft.ch/PDF/Visual_SUNT_Pro_Data.html, last accessed July 2020), seismic UNIX (Cohen, J. K., & Stockwell, J. W. (2000). CWP/SU: Seismic Unix Release 33: A Free Package for Seismic Research and Processing, Center for Wave Phenomena, Colorado School of Mines, Colorado), Paradigm ECHOS by Emerson E&P (https://www.pdgm.com/solutions/seismic-processing-and-imaging/seismic-processing, last accessed July 2020), and MATLAB by Mathworks. We obtained digital elevation data for Figures 1a, 1c and 1d from the U.S. Geological Survey (USGS) National Elevation Dataset (https://viewer.nationalmap.gov/basic/, last accessed March 2020). Geologic map data for Figure 1b was obtained from the USGS Geoscience Data Catalog (https://geo-nsdi.er.usgs.gov/metadata/open-file/99-554/metadata.html, last accessed July 2020).

Contained in the Appendix A of this article, Figure 1.A.1 is LANL-80-6, a legacy seismic profile near HADDOCK. Figure 1.A.2 has raw and filtered average spectra plots of the field data, and Figure 1.A.3 has stacking velocity models and unmigrated stacks for Line 500 and Line 600.

1.11 Acknowledgements

The Source Physics Experiment (SPE) would not have been possible without the support of many people from several organizations. The authors wish to express their gratitude to the National Nuclear Security Administration, Defense Nuclear Nonproliferation Research and Development, and the SPE working group, a multi-institutional and interdisciplinary group of scientists and engineers. We also thank Ping Lee, Ray Keegan, Bob White, Kale McLin, and Jesse Bonner for field support. Field acquisition of the Seismic Hammer dataset was in conjunction with John Hampshire, Rob Henley, and Peter Eick. Field acquisition of the AWD dataset was in conjunction with Sean Hollister, Samuel Bolin, and Matthew Geuss. Lance Prothro provided information on the geology of the NNSS and past seismic reflection experiments. The authors are also grateful to Christian Poppeliers, Thomas Brocher, Don Steeples and the anonymous reviewer for their helpful comments on this manuscript.

Sandia National Laboratories is a multimission laboratory managed and operated by National Technology & Engineering Solutions of Sandia, LLC, a wholly owned subsidiary of Honeywell International Inc., for the U.S. Department of Energy's National Nuclear Security Administration under contract DE-NA0003525. This paper describes objective technical results and analysis. Any subjective views or opinions that might be expressed in the paper do not necessarily represent the views of the U.S. Department of Energy or the United States Government.

References

Abbott, R. E., L. L. Worthington, and L. A. Preston (2017), Frey-nevada national security site haddock, *Tech. rep.*, International Federation of Digital Seismograph Networks, doi:10.7914/SN/X3_2017.

Allen, B., S. J. Drellack, and M. Townsend (1997), Surface effects of underground nuclear explosions, *Tech. rep.*, Bechtel Nevada Corporation (BNC), doi:10.2172/671858.

Büker, F., A. G. Green, and H. Horstmeyer (1998), Shallow seismic reflection study of a glaciated valley, *Geophysics*, *63*(4), 1395–1407.

Carothers, J. (1995), Caging the dragon: the containment of underground nuclear explosions, *Tech. rep.*, Office of Scientific and Technical Information, Oak Ridge, TN, doi:10.2172/524871.

Červen, V., and I. Pšenčík (1983), Gaussian beams in two-dimensional elastic inhomogeneous media, *Geophysical Journal International*, *72*(2), 417–433, doi: 10.1111/j.1365-246X.1983.tb03793.x.

Chen, T., C. M. Snelson, and R. J. Mellors (2017), Seismic Imaging of the Source Physics Experiment Site with the Large-N Seismic Array, in *AGU Fall Meeting Abstracts*.

Cogbill, A. H., and S. R. Taylor (1994), PRE-AND POST-EVENT SEISMIC REFLECTION SURVEY AT THE DIVIDER SITE, NEVADA TEST SITE.

Connor, C. B., J. A. Stamatakos, D. A. Ferrill, B. E. Hill, G. I. Ofoegbu, F. M. Conway, B. Sagar, and J. Trapp (2000), Geologic factors controlling patterns of small-volume basaltic volcanism: Application to a volcanic hazards assessment at Yucca Mountain, Nevada, *Journal of Geophysical Research: Solid Earth*, *105*(B1), 417–432, doi:10.1029/1999JB900353.

Day, S. M., and K. L. McLaughlin (1991), Seismic source representations for spall, *Bulletin of the Seismological Society of America*, *81*(1), 191–201.

Dobrin, M. B., and C. H. Savit (1988), Introduction to Geophysical ProspectingMcGraw-Hill Book Co, *New York (867 pp.)*.

DOE, D. o. E. (2000), United States Nuclear Tests July 1945 through September 1992, *DOE/NV—209-REV 15*.

Drellack, S. L., Jr., L. B. Prothro, J. L. Gonzales, and J. M. Mercadante (2010), The Hydrogeologic Character of the Lower Tuff Confining Unit and the Oak Springs Butte Confining Unit in the Tuff Pile Area of Central Yucca Flat, *Tech. rep.*, Nevada Test Site/National Security Technologies, LLC (United States), doi:10.2172/985874.

Eisler, J. D., and F. Chilton (1964), Spalling of the Earth's surface by underground nuclear explosions, *Journal of Geophysical Research*, *69*(24), 5285–5293, doi:10.1029/jz069i024p05285.

Farhang-Boroujeny, B. (1999), *Adaptive filters: theory and applications*, John Wiley & Sons.

Fenelon, J. (2005), Analysis of Ground-Water Levels and Associated Trends in Yucca Flat, Nevada Test Site, Nye County, Nevada, 1951-2003, *Tech. rep.*, National Nuclear Security Agency Service Center, doi:10.2172/860820.

Finlay, T. S., R. E. Abbott, H. A. Knox, D. G. Tang, S. R. James, M. M. Haney, and J. B. Hampshire (2015), Hammering Yucca Flat, part two: Shear-wave velocity, *AGUFM*, *2015*, S53B–2809.

Ford, S. R., and W. R. Walter (2013), An explosion model comparison with Insights from the source physics experiments, *Bulletin of the Seismological Society of America*, *103*(5), 2937–2945, doi:10.1785/0120130035.

Forel, D., T. Benz, and W. D. Pennington (2005), *Seismic Data Processing with Seismic Un∗ x: A 2D Seismic Data Processing Primer*, 4–1 pp., Society of Exploration Geophysicists, Tulsa, OK (United States).

Gardner, G. H. F., L. W. Gardner, and A. R. Gregory (1974), FORMATION VELOCITY AND DENSITY—THE DIAGNOSTIC BASICS FOR STRATIGRAPHIC TRAPS, *GEOPHYSICS*, *39*(6), 770–780, doi:10.1190/1.1440465.

Germain, L. S., and J. S. Kahn (1968), Phenomenology and Containment of Underground Nuclear Explosions, Lawrence Radiation Laboratory, Livermore, Rept, *UCRL-50482*.

Glasstone, S., and P. J. Dolan (1977), The effects of nuclear weapons, US Department of Defense, *Energy Research and Development Administration, Washington.*

Grasso, D. N. (2000), Geologic surface effects of underground nuclear testing, Yucca Flat, Nevada Test Site, Nevada, *Tech. rep.*

Grasso, D. N. (2003), Geologic Surface Effects of Underground Nuclear Testing, Buckboard Mesa, Climax Stock, Dome Mountain, Frenchman Flat, Rainier/Aqueduct Mesa, and Shoshone Mountain, Nevada Test Site, Nevada, *Tech. rep.*, doi: 10.3133/ofr03125.

Hakala, W. W. (1970), Subsidence caused by an underground nuclear explosion, *Tech. rep.*

Hampshire, J. B., and J. O'Donnell (2013), The Seismic Hammer™: A. 16 MJoule seismic source with flat output spectrum from 10s to 250 Hz.

Higgins, G. H. (1970), Nuclear explosion data for underground engineering applications. Peaceful Nuclear Explosions, in *Proceedings*, pp. 111–121.

Hole, J. A., and B. C. Zelt (1995), 3-D finite-difference reflection travel times, *Geophysical Journal International*, *121*(2), 427–434, doi:10.1111/j.1365-246X.1995.tb05723.x.

Hoots, C. R., R. Abbott, L. Preston, H. Knox, and P. C. Schwering (2020), Near-field imaging of shallow chemical explosions in granite using change detection methods with surface and borehole seismic data, *Tech. rep.*, Sandia National Lab.(SNL-NM), Albuquerque, NM (United States).

Hudson, B. C., E. M. Jones, C. E. Keller, and C. W. Smith (1983), Proceedings of the Monterey Containment Symposium, Monterey, California, August 26-28, 1981. Volume 1, *Tech. rep.*

Hudson, M. R., D. A. Sawyer, and R. G. Warren (1994), Paleomagnetism and rotation constraints for the middle Miocene southwestern Nevada volcanic field, *Tectonics*, *13*(2), 258–277.

Hunter, J. A., S. E. Pullan, R. A. Burns, R. M. Gagne, and R. L. Good (1984), Shallow seismic reflection mapping of the overburden-bedrock interface with the engineering seismograph—Some simple techniques, *GEOPHYSICS*, *49*(8), 1381–1385, doi:10.1190/1.1441766.

Jones, E., F. App, and R. Whitaker (1993), Ground motions and the infrasound signal: A new model and the discovery of a significant cavity rebound signal. Los Alamos Source Region Program, *Tech. rep.*, Los Alamos National Laboratory (LANL), Los Alamos, NM, doi:10.2172/10165578.

Jones, K. R., R. W. Whitaker, and S. J. Arrowsmith (2015), Modelling infrasound signal generation from two underground explosions at the Source Physics Experiment using the Rayleigh integral, *Geophysical Journal International*, *200*(2), 779–790, doi:10.1093/gji/ggu433.

Jongerius, P., and K. Helbig (1988), Onshore high-resolution seismic profiling applied to sedimentology, *GEOPHYSICS*, *53*(10), 1276–1283, doi:10.1190/1.1442405.

Keiswetter, D., and I. J. Won (1997), Multifrequency electromagnetic signature of the cloud chamber, Nevada test site, *Journal of Environmental and Engineering Geophysics*, *2*(2), 99–103.

Klemperer, S. L. (1987), Seismic noise-reduction techniques for use with vertical stacking: An empirical comparison, *GEOPHYSICS*, *52*(3), 322–334, doi:10.1190/1.1442306.

Lee, R. F., and R. E. Abbott (2017), Test to Extract Soil Properties Using the Seismic HammerTM Active Seismic Source, *Tech. rep.*, Sandia National Laboratories (SNL), Albuquerque, NM, and Livermore, CA (United States), doi: 10.2172/1380104.

Liu, Y. (2010), Gaussian-beam Modeling in Heterogeneous Anisotropic Media, doi: 10.1.1.170.4353.

Maldonado, F. (1977), Summary of the geology and physical properties of the Climax Stock, Nevada Test Site, *Tech. rep.*, doi:10.3133/ofr77356.

Mellors, R. J. (2011), Seismic reflection imaging of underground cavities using open-source software, *Tech. rep.*, Lawrence Livermore National Laboratory (LLNL), Livermore, CA (United States), doi:10.2172/1034499.

Mellors, R. J., A. Pitarka, E. Matzel, S. Magana-Zook, D. Knapp, W. R. Walter, T. Chen, C. M. Snelson, and R. E. Abbott (2018), The Source Physics Experiments Large N Array, *Seismological Research Letters*, *89*(5), 1618–1628, doi: 10.1785/0220180072.

Merkle, D. H. (1980), Basic mechanisms of spall from near-surface explosions. Final report, 1 April-31 October 1980, *Tech. rep.*

Miller, R., and D. Steeples (1992), Seismic reflection surveys before and after BEXAR at the Nevada Test Site. Los Alamos Source Region Project: Final report, *Tech. rep.*, Los Alamos National Laboratory (LANL), Los Alamos, NM, doi:10.2172/10186626.

Miller, R., and D. W. Steeples (1991), Detecting voids in a 0.6 m coal seam, 7 m deep, using seismic reflection, *Geoexploration*, *28*(2), 109–119, doi:10.1016/0016-7142(91)90043-C.

Minor, S. A. (1995), Superposed local and regional paleostresses: Fault-slip analysis of Neogene extensional faulting near coeval caldera complexes, Yucca Flat, Nevada, *Journal of Geophysical Research: Solid Earth*, *100*(B6), 10,507–10,528, doi:10.1029/95JB00078.

Muller, G. (1984), Efficient calculation of Gaussian-beam seismograms for two-dimensional inhomogeneous media, *Geophysical Journal International*, *79*(1), 153–166, doi:10.1111/j.1365-246X.1984.tb02847.x.

Oppenheim, A., and R. W. Schafer (1975), Digital signal processing(Book), *Research supported by the Massachusetts Institute of Technology, Bell Telephone Laboratories, and Guggenheim Foundation. Englewood Cliffs, N. J., Prentice-Hall, Inc., 1975. 598 p.*

Oppenheim, A., R. W. Schafer, and J. R. Buck (1989), Discrete-Time Signal Processing: Prectice Hall, *Englewood Cliffs, New Jersey.*

Patton, H. J., and S. R. Taylor (1995), Analysis of Lg spectral ratios from NTS explosions: Implications for the source mechanisms of spall and the generation of Lg waves, *Bulletin of the Seismological Society of America*, *85*(1), 220–236.

Phelps, G. A., A. Boucher, and K. J. Halford (2011), A refined characterization of the alluvial geology of yucca flat and its effect on bulk hydraulic conductivity, *US Geological Survey, Open-File Report*, *1307*, doi:10.3133/ofr20101307.

Poppeliers, C., K. Anderson Aur, and L. A. Preston (2019), The Relative Importance of Assumed Infrasound Source Terms and Effects of Atmospheric Models on the Linear Inversion of Infrasound Time Series at the Source Physics Experiment, *Bulletin of the Seismological Society of America*, *109*(1), 463–475, doi:10.1785/0120180249.

Preston, L. A., K. C. Creager, R. S. Crosson, T. M. Brocher, and A. M. Trehu (2003), Intraslab earthquakes: dehydration of the Cascadia slab., *Science (New York, N.Y.)*, *302*(5648), 1197–200, doi:10.1126/science.1090751.

Preston, L. A., K. Smith, and D. von Seggern (2007), P wave velocity structure in the Yucca Mountain, Nevada, region, *Journal of Geophysical Research*, *112*(B11), B11,305, doi:10.1029/2007JB005005.

Proffett Jr, J. M. (1977), Cenozoic geology of the Yerington district, Nevada, and implications for the nature and origin of Basin and Range faulting, *Geological Society of America Bulletin*, *88*(2), 247–266.

Prothro, L., H. Huckins-Gang, S. Drellack, D. Reed, M. Townsend, K. Day, and T. Kincaid (2016), Three-dimensional seismic-attribute model for Yucca Flat, *Tech. rep.*

Pugin, A., and S. E. Pullan (2000), First-Arrival Alignment Static Corrections Applied to Shallow Seismic Reflection Data1, *Journal of Environmental and Engineering Geophysics*, *5*(1), 7–15, doi:10.4133/JEEG5.1.7.

Robinson, E. A., and S. Treitel (2000), *Geophysical signal analysis*, Society of Exploration Geophysicists.

Rygg, E. (1979), Anomalous surface waves from underground explosions, *Bulletin of the Seismological Society of America*, *69*(6), 1995–2002.

Schlittenhardt, J. (1991), The effects of spall on teleseismic P-waves: An investigation with theoretical seismograms, in *Explosion Source Phenomenology*, vol. 65, pp. 141–150, Wiley Online Library, doi:10.1029/GM065p0141.

Schramm, K. A., R. E. Abbott, M. Asten, S. Bilek, A. Pancha, and H. J. Patton (), Broadband Rayleigh-Wave Dispersion Curve and Shear-Wave Velocity Structure for Yucca Flat, Nevada, doi:10.1785/0120110296.

Sexton, E., C. M. Snelson, V. D. Chipman, D. Emer, B. White, R. Emmit, A. Wright, S. Drellack, H. Huckins-Gang, and J. Mercadante (2013), Site Characterization of the Source Physics Experiment Phase II Location Using Seismic Reflection Data, *Tech. rep.*

Sloan, S. D., S. L. Peterie, R. D. Miller, J. Ivanov, J. T. Schwenk, and J. R. McKenna (2015), Detecting clandestine tunnels using near-surface seismic techniques, *GEOPHYSICS*, *80*(5), EN127–EN135, doi:10.1190/geo2014-0529.1.

Snelson, C. M., R. E. Abbott, S. T. Broome, R. J. Mellors, H. J. Patton, A. J. Sussman, M. J. Townsend, and W. R. Walter (2013), Chemical explosion experiments to improve nuclear test monitoring, *Eos*, *94*(27), 237–239, doi:10.1002/2013EO270002.

Springer, D. L. (2002), Seismic Source Summary for All U.S. Below-Surface Nuclear Explosions, *Bulletin of the Seismological Society of America*, *92*(5), 1806–1840, doi:10.1785/0120010194.

Steeples, D. W., A. G. Green, T. V. McEvilly, R. D. Miller, W. E. Doll, and J. W. Rector (1997), A workshop examination of shallow seismic reflection surveying, *The Leading Edge*, *16*(11), 1641–1647, doi:10.1190/1.1437543.

Stump, B. W. (1985), Constraints on explosive sources with spall from near-source waveforms, *Bulletin of the Seismological Society of America*, *75*(2), 361–377.

Sweetkind, D. S., I. Drake, and M. Ronald (2007), Geologic characterization of young alluvial basin-fill deposits from drill hole data in yucca flat, nye county, nevada., *Tech. rep.*, United States Geological Survey-Nevada, Henderson, Nevada, doi:10.3133/ofr20061390.

Tang, D. G., R. E. Abbott, L. A. Preston, and J. B. Hampshire (2015), Hammering Yucca Flat, Part One: P-Wave Velocity, in *AGU Fall Meeting Abstracts*.

Taylor, S. R., and G. E. Randall (1989), The effects of Spall on regional seismograms, *Geophysical Research Letters*, *16*(2), 211–214, doi:10.1029/GL016i002p00211.

Toney, L. D., R. E. Abbott, L. A. Preston, D. G. Tang, T. Finlay, and K. Phillips-Alonge (2019), Joint Body- and Surface-Wave Tomography of Yucca Flat, Nevada, Using a Novel Seismic Source, *Bulletin of the Seismological Society of America*, *109*(5), 1922–1934, doi:10.1785/0120180322.

Townsend, M., and C. Obi (2015), Data Release Report for Source Physics Experiments 2 and 3 (SPE-2 and SPE-3) Nevada National Security Site, *Tech. rep.*, National Security Technologies, doi:10.2172/1179079.

Tricot, J. C., B. Dellanoy, B. Piwakowski, and P. Pernod (1987), Some problems and experimental results of seismic shallow prospecting, in *Proceedings of the Fifteenth International Symposium, July 14–6, 1986*, pp. 471–479, Springer.

Vincent, P., S. M. Buckley, D. Yang, and S. F. Carle (2011), Anomalous transient uplift observed at the Lop Nor, China nuclear test site using satellite radar interferometry time-series analysis, *Geophysical Research Letters*, *38*(23), 1–7, doi:10.1029/2011GL049302.

Widrow, B., and S. D. Stearns (1985), Adaptive Signal Processing Prentice-Hall, *Englewood Cliffs, NJ.*

Yilmaz, O. (2001), Processing, Inversion, and Interpretation of Seismic Data, in *Seismic Data Analysis*, 3 ed., pp. 24–124, Society of Exploration Geophysicists, Tulsa, OK (United States), doi:10.1190/1.9781560801580.fm.

Appendix

1.A Supplementary Figures

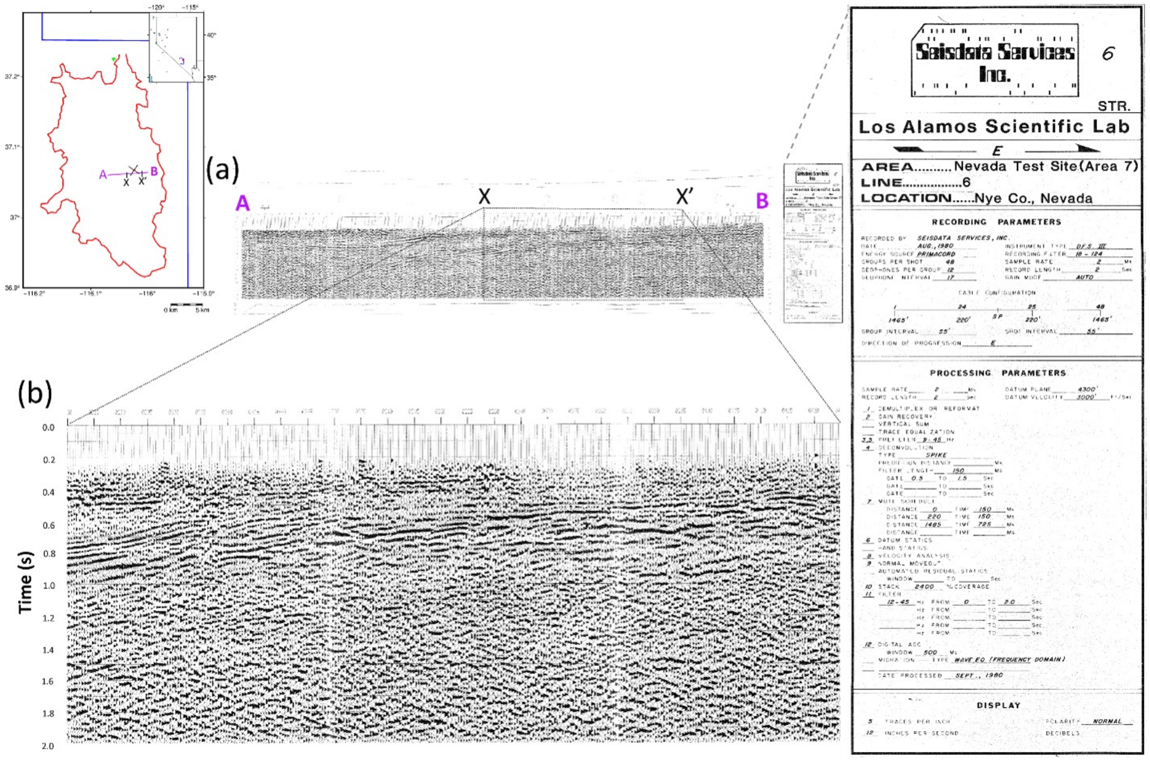

Seisdata Services Inc. 6

STR.

Los Alamos Scientific Lab

E

AREA.........Nevada Test Site(Area 7)
LINE...............6
LOCATION......Nye Co., Nevada

RECORDING PARAMETERS

RECORDED BY SEISDATA SERVICES, INC.
DATE AUG., 1980
INSTRUMENT TYPE DFS III
ENERGY SOURCE PRIMACORD
RECORDING FILTER 18 - 124
GROUPS PER SHOT 48
SAMPLE RATE 2 Ms
GEOPHONES PER GROUP 12
RECORD LENGTH 2 Sec
GEOPHONE INTERVAL 17
GAIN MODE AUTO

CABLE CONFIGURATION

1 1465' 24 220' SP 25 220' 48 1465'

GROUP INTERVAL 55'
SHOT INTERVAL 55'
DIRECTION OF PROGRESSION E

PROCESSING PARAMETERS

SAMPLE RATE 2 Ms
DATUM PLANE 4300'
RECORD LENGTH 2 Sec
DATUM VELOCITY 3000' Ft/Sec

1 DEMULTIPLEX OR REFORMAT
2 GAIN RECOVERY
VERTICAL SUM
TRACE EQUALIZATION
3,5 PREFILTER 9-45 Hz
4 DECONVOLUTION
TYPE SPIKE
PREDICTION DISTANCE Ms
FILTER LENGTH 150 Ms
GATE 0.5 TO 1.5 Sec
GATE TO Sec
GATE TO Sec
7 MUTE SCHEDULE
DISTANCE 0 TIME 150 Ms
DISTANCE 220 TIME 150 Ms
DISTANCE 1465 TIME 725 Ms
DISTANCE TIME Ms
6 DATUM STATICS
HAND STATICS
8 VELOCITY ANALYSIS
9 NORMAL MOVEOUT
AUTOMATED RESIDUAL STATICS
WINDOW TO Sec
10 STACK 2400 % COVERAGE
11 FILTER
12-45 Hz FROM 0 TO 2.0 Sec
Hz FROM TO Sec
Hz FROM TO Sec
Hz FROM TO Sec
Hz FROM TO Sec
12 DIGITAL AGC
WINDOW 500 Ms
MIGRATION TYPE WAVE EQ (FREQUENCY DOMAIN)
DATE PROCESSED SEPT., 1980

DISPLAY

5 TRACES PER INCH
POLARITY NORMAL
12 INCHES PER SECOND
DECIBELS

Figure 1.A.1: Legacy seismic profile (LANL-80-6) near HADDOCK (L. Prothro, written comm., 2018). (a) The entire seismic line. The purple letter A marks the beginning of the line while the purple letter B marks the end of the seismic line. (b) A subset of the seismic line (X to X') showing the prominent basin reflectors near HADDOCK lie with the 0.4–1.2 s window.

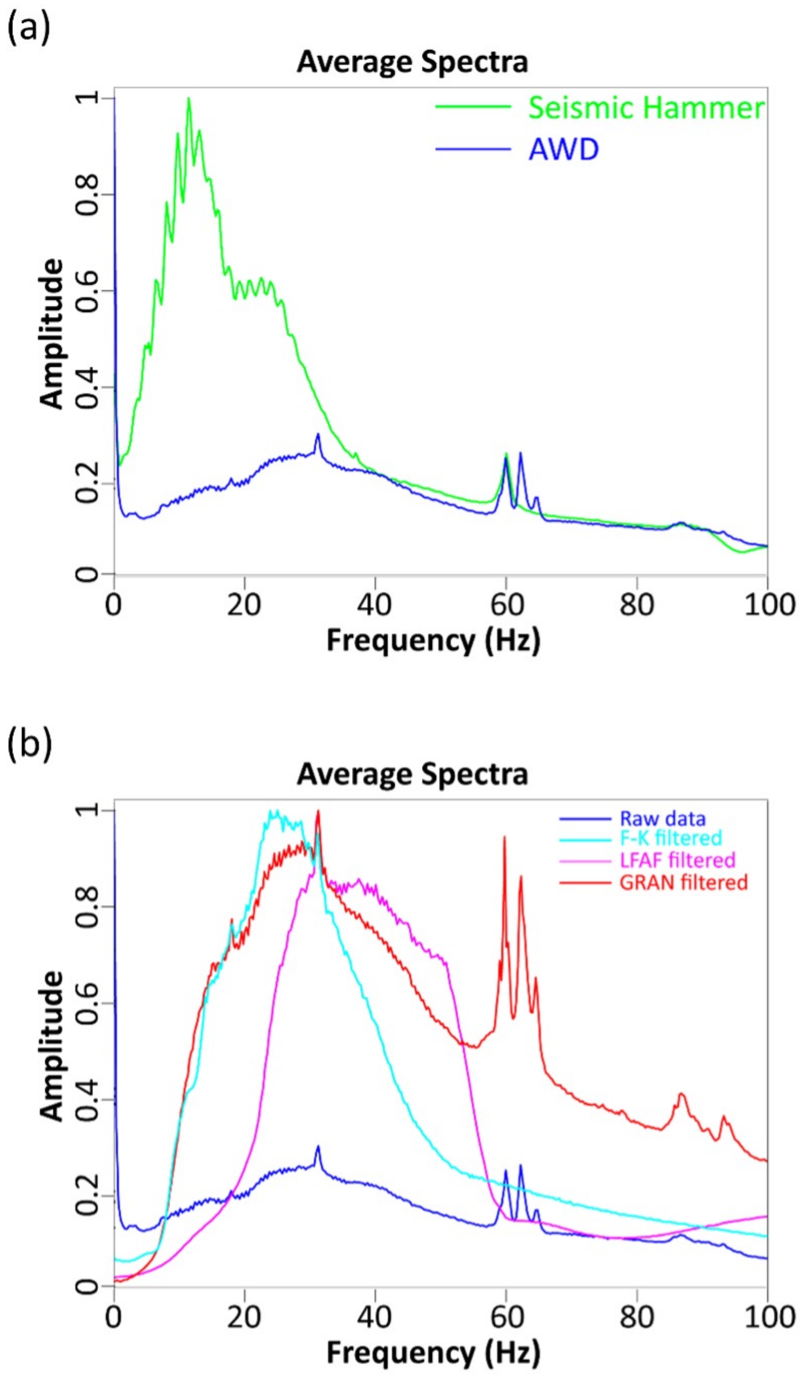

Figure 1.A.2: Average spectra plots. (a) The green curve is the average spectra of the raw Seismic Hammer field data. The blue curve is the average spectra of the raw Accelerated Weight Drop field data. (b) Average spectra of the Accelerated Weight Drop field data after applying different ground-roll removal filters. The blue curve represents the average spectra of the raw data. The cyan curve is the average spectra of the f-κ filtered data. The magenta curve is the average spectra of the low-frequency array filtered (LFAF) data. The red curve is the average spectra of the ground roll adaptive noise (GRAN) filtered data.

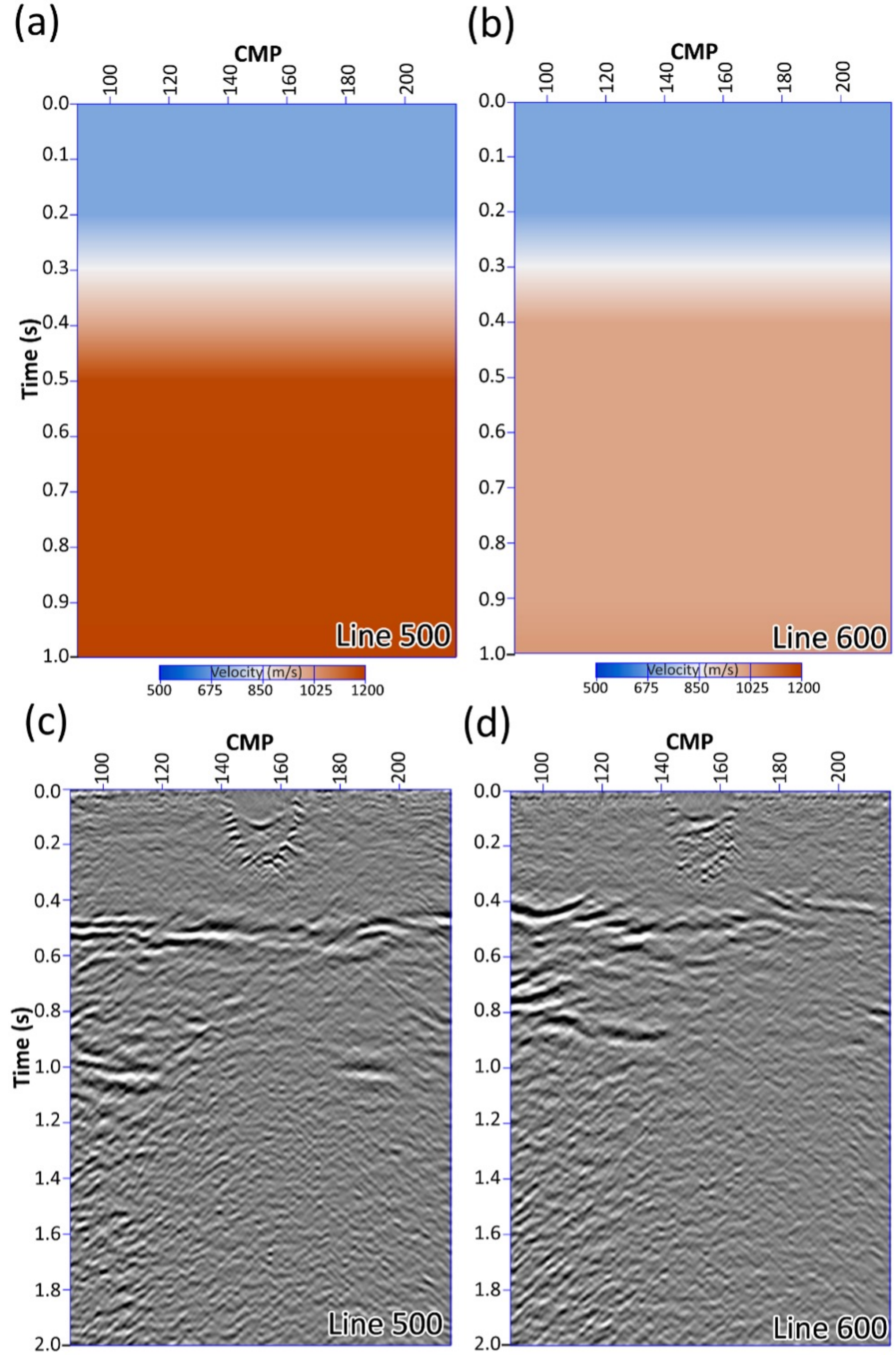

Figure 1.A.3: Final stacking velocities for Line 500 and Line 600. (a) Stacking velocity model for Line 500. (b) Stacking velocity model for Line 600. (c) Unmigrated stack of Line 500. (d) Unmigrated stack of Line 600.

2 Subduction Zone Interface Structure Within the Southern Mw9.2 1964 Great Alaska Earthquake Asperity: Constraints From Receiver Functions Across a Spatially Dense Node Array

Authors and Affiliations

Evans A. Onyango[1*]

Lindsay L. Worthington[1]

Brandon Schmandt[1]

Geoffrey A. Abers[2]

[1]Dept. of Earth and Planetary Sciences, University of New Mexico, Albuquerque, New Mexico, USA

[2]Department of Earth and Atmospheric Sciences, Cornell University, Ithaca, New York, USA

[*]Corresponding author

Modified from a manuscript published in *Geophysical Research Letters*

2.1 Abstract

We conduct a high-resolution teleseismic receiver function investigation of the subducting plate interface within the Alaskan forearc beneath Kodiak Island using data collected as part of the Alaska Amphibious Community Seismic Experiment in 2019. The Kodiak node array consisted of 398 nodal geophones deployed at ∼200–300 m spacing on northeastern Kodiak Island within the southern asperity of the 1964 M_W9.2 Great Alaska earthquake. Receiver function images at frequencies of 1.2 and 2.4 Hz show a coherent, slightly dipping velocity increase at ∼30–40 km depth consistent with the expected slab Moho. In contrast to studies within the

northern asperity of the 1964 rupture, we find no evidence for a prominent low-velocity layer above the slab Moho thick enough to be resolved by upgoing P-to-S conversions. These results support evidence from seismicity and geodetic strain suggesting that the 1964 rupture connected northern (Kenai) and southern (Kodiak) asperities with different plate interface properties.

2.2 Introduction

Understanding plate interface structure and subduction geometries can illuminate slip mechanisms, earthquake rupture behavior and shallow subduction zone processes. Because most global forearc regions are submerged, they are commonly studied via marine seismic methods, which, thus far, precludes dense-array natural source seismic imaging. Therefore, well-exposed forearcs such as Kodiak Island provide rare opportunities to study subduction zone and plate interface structure within the shallow forearc using a dense seismic array. Here, we use three-component node array data acquired in 2019 across northeastern Kodiak Island as part of the Alaska Amphibious Community Seismic Experiment (AACSE) to compute Ps teleseismic receiver functions (RFs) to better understand the nature of the plate interface in the rupture area of the 1964 $M_W 9.2$ Great Alaska earthquake.

The Alaska-Aleutian subduction zone has hosted more M>8 earthquakes than any other system globally and offers opportunities to explore relationships between megathrust slip phenomena, seismicity, deformation and forearc structure. The Kodiak node array (Figure 2.2.1a-c) lies within the southern rupture area of the 1964 $M_W 9.2$ Great Alaska earthquake, the second largest earthquake ever recorded (*Kanamori*, 1977, Figure 2.2.1a). Coseismic slip and ground shaking from this event created damage across a 600–800 km section of the Alaskan margin and triggered local and far-field tsunami. Previous work investigating static deformation, seismic

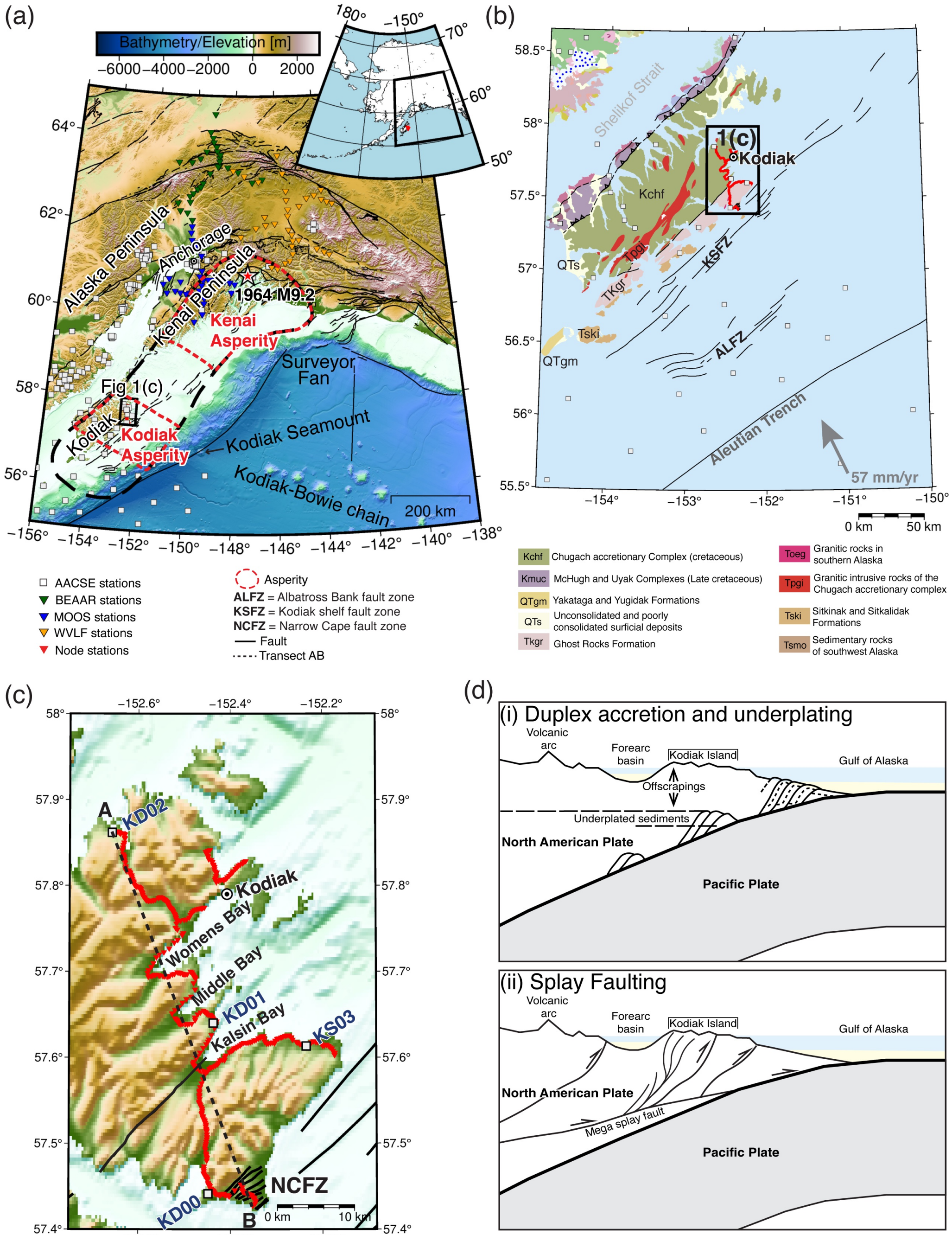
(a)
Bathymetry/Elevation [m]
−6000 −4000 −2000 0 2000
180°
−150°
70°
60°
50°
64°
62°
60°
58°
56°
Alaska Peninsula
Anchorage
Kenai Peninsula
1964 M9.2
Kenai Asperity
Surveyor Fan
Fig 1(c)
Kodiak
Kodiak Asperity
Kodiak Seamount
Kodiak-Bowie chain
200 km
−156° −154° −152° −150° −148° −146° −144° −142° −140° −138°
AACSE stations
BEAAR stations
MOOS stations
WVLF stations
Node stations
Asperity
ALFZ = Albatross Bank fault zone
KSFZ = Kodiak shelf fault zone
NCFZ = Narrow Cape fault zone
Fault
Transect AB
(b)
58.5°
58°
57.5°
57°
56.5°
56°
55.5°
Shelikof Strait
1(c)
Kodiak
Kchf
Tpgi
QTs
TKgr
KSFZ
Tski
QTgm
ALFZ
Aleutian Trench
57 mm/yr
−154° −153° −152° −151° −150°
0 km 50 km
Kchf Chugach accretionary Complex (cretaceous)
Kmuc McHugh and Uyak Complexes (Late cretaceous)
QTgm Yakataga and Yugidak Formations
QTs Unconsolidated and poorly consolidated surficial deposits
Tkgr Ghost Rocks Formation
Toeg Granitic rocks in southern Alaska
Tpgi Granitic intrusive rocks of the Chugach accretionary complex
Tski Sitkinak and Sitkalidak Formations
Tsmo Sedimentary rocks of southwest Alaska
(c)
−152.6° −152.4° −152.2°
58°
57.9°
57.8°
57.7°
57.6°
57.5°
57.4°
A
KD02
Kodiak
Womens Bay
Middle Bay
KD01
Kalsin Bay
KS03
NCFZ
KD00
B
0 km 10 km
(d)
(i) Duplex accretion and underplating
Volcanic arc
Forearc basin
Kodiak Island
Gulf of Alaska
Offscrapings
Underplated sediments
North American Plate
Pacific Plate
(ii) Splay Faulting
Volcanic arc
Forearc basin
Kodiak Island
Gulf of Alaska
North American Plate
Mega splay fault
Pacific Plate

Figure 2.2.1: Study area. (a) Shaded topographic map and faults of southern Alaska and the Kodiak Islands region. MOOS array (blue triangles), BEAAR array (green triangles), WVLF array (Orange triangles). (b) Geology map of the Kodiak Islands region. Refer to Wilson et al. (2015) for geologic unit explanation. (c) Shaded topographic map of the study area. (d) Schematic diagrams depicting scenarios for Kodiak Island formation and deformation. (i) Modified from Paterson and Sample (1988) illustrates the duplex accretion and underplating scenario. (ii) Modified from Tsuji et al. (2014) illustrates the splay faulting scenario.

waves, and tsunami propagation from this event revealed two major coseismic slip asperities: the Kenai asperity in the north and the Kodiak asperity in the south (*Christensen and Beck*, 1994; *Ichinose et al.*, 2007; *Johnson et al.*, 1996; *Suito and Freymueller*, 2009, Figure 2.2.1a). Differences in coseismic slip (*Johnson et al.*, 1996), major earthquake recurrence interval (*Nishenko and Jacob*, 1990; *Wesson et al.*, 1999), locking (*Li and Freymueller*, 2018; *Zweck et al.*, 2002), subduction geometries (*Christeson et al.*, 2010) and sediment input (*Reece et al.*, 2011; *Worthington et al.*, 2012) between these two regions suggest major differences in subduction and interface properties within south-central Alaska.

2.3 Geologic Background and Previous Geophysical Studies of the 1964 Rupture Area

Kodiak Island (Qikertaq in Alutiiq) is part of an archipelago that represents an exposed section of the Mesozoic-Tertiary Alaska-Aleutian accretionary complex uplifted either via duplex accretion and underplating (*Sample and Fisher*, 1986), out-of-sequence splay faulting (e.g., *Rowe et al.*, 2009), or a combination of these processes. The surface exposures consist of Jurassic to Eocene formations bounded by NW-dipping and NE-striking thrusts (*Wilson et al.*, 2015, Figure 2.2.1b). The thrust-bounded units get progressively younger towards the southeast, approaching the current subduction trench offshore (Figure 2.2.1b). Potentially active Quaternary fault systems include the Albatross Bank, Kodiak Shelf and Narrow Cape fault zones (Figure 2.2.1b and 2.2.1c). Paleocene granitic intrusions (∼58–50 Ma) from ridge subduction (*Ayuso et al.*, 2009; *Farris et al.*, 2006, Figure 2.2.1b) form the mountainous spine of the island interior. In the duplex accretion and underplating scenario for Kodiak Island formation and deformation, a stacked section of marine sediments builds up near the subduction decollement, forming a series of flat-ramp-flat geometries of imbricated material at depth within the overriding plate (*Sample and Fisher*, 1986, Figure 2.2.1d (i)). The build-up of the underthrusted material causes the accretionary prism to grow vertically, with minimal fault penetration or deformation within the overlying sediments. In the splay fault model (Figure 2.2.1d (ii)), the island was uplifted due to deformation on one or several seaward-vergent thrusts possibly rooted at the megathrust.

Prior to our study, the 2007-2008 Multidisciplinary Observations of Onshore Subduction (MOOS; *Li et al.*, 2013, Figure 2.2.1a) measured structure and seismicity beneath the Kenai Peninsula in the northern 1964 rupture zone. The MOOS experiment included 34 broadband seismometers deployed at 10–15 km station spacing. Major results include RF imaging showing a 3–5 km-thick low-velocity zone (LVZ) sandwiched between the overriding North American plate and the subducting Yakutat microplate (*Kim et al.*, 2014). This low-velocity zone suggests the presence of subducting sediments and/or the presence of fluids within or below the plate interface. Imaging via autocorrelation of P-wave coda from local earthquakes replicates these results and further suggests that S-wave velocity within this zone decreases with depth (*Kim et al.*, 2019).

A more recent study of the subducting crust beneath southcentral Alaska suggests that the LVZ extends far beyond the location of the MOOS array. In their scattered-wave imaging of the subduction zone beneath southcentral Alaska, *Mann et al.* (2022) analyzed seismic data recorded by 218 broadband seismometers across southcentral Alaska. Using data from the Wrangell Volcanism and Lithospheric Fate (WVLF; Figure 2.2.1a) array, the Broadband Experiment Across the Alaska Range (BEAAR; Figure 2.2.1a) array, the Transportable Array (TA) and the MOOS array, they found that the LVZ covers > 450 km of the subducting Yakutat terrane (*Mann et al.*, 2022). Our study tests whether these features extend southward, controlling structure beneath northeast Kodiak Island.

2.4 Data and methods

2.4.1 The AACSE

The AACSE took place in 2018-2019 between Kodiak Island and Sanak Island (*Abers et al.*, 2019; *Barcheck et al.*, 2020, Figure 2.2.1a). All experiment data is publicly available and was open immediately upon completion of quality assurance, control and archiving. The AACSE included 75 broadband ocean-bottom seismometers (OBS), 30 broadband land seismometers, several dozen additional nearby permanent and EarthScope Transportable Array seismometers, complementary strong motion sensors and absolute- and differential-pressure gauges, and >3,000 km of active source wide-angle refraction profiles collected by the R/V Marcus G Langseth (*Barcheck et al.*, 2020). The Kodiak node array was deployed in 2019 as a supplement to the larger AACSE. The array consisted of 398 FairfieldNodal autonomous node sensors (from PASSCAL and University of Utah) with 3-component 5-Hz geophones deployed along a ∼50 km road network centered on the city of Kodiak (Figure 2.2.1b and 2.2.1c). Sensors were deployed at ∼200–300 m station spacing over the course of 6 days (May 18-24) and recovered over 3 days (June 19–21). The full nodal array was operational for 25 days (May 25 to June 18). All continuous waveform data from the node array are available in PH5 format via IRIS Data Services (network code 8J from 2019).

2.4.2 Receiver Function Processing

Previous work shows that the autonomous three-component 5-Hz geophones used in this study can yield high-quality RFs comparable with co-located broadband seismometers (*Liu et al.*, 2018; *Ward and Lin*, 2017; *Ward et al.*, 2018). Like those earlier studies, our short deployment period limited the number of teleseismic events for RF calculation. Out of 52 teleseismic events M>5.0 occurring within the 30°–90°

search radius, we retained 7 events (Table 2.B.1; Figure 2.A.1a,b) that met the selection criteria: (1) a magnitude >5.5, (2) a 30°–90° epicentral distance from the center of the array, and (3) a signal-to-noise ratio (SNR)>3 and an identifiable incident P wave across the array (Figure 2.A.1c).

Prior to calculating RFs, we windowed the seismograms from 15 s before to 75 s after the theoretical P arrival. Next, we decimated the waveforms to 50 samples per second using a finite impulse response filter to prevent aliasing. We then removed the mean and the trend and applied a Hanning taper. Finally, we removed the instrument response from the nodal geophones (5 Hz corner frequency). We followed the above steps as outlined by (*Ward et al.*, 2018). We then filtered the resulting time series using a bandpass of 0.2–2.0 Hz. To groundtruth our waveform processing workflow, we retrieved waveforms for the selected 7 events recorded by AACSE broadband stations deployed within the node array footprint (*Li et al.*, 2020), performed the same pre-processing procedure, and compared the resultant broadband waveforms with the pre-processed nodal time series (Appendix 2.A Figure 2.A.2).

After preprocessing, we culled additional noisy signals by applying a SNR-based noise reduction procedure which eliminated traces with SNR<2.0 on the vertical component or SNR<1.25 on the north component. Then we rotated from the station ZNE (vertical, north, east) coordinate system to the earthquake ZRT (vertical, radial, transverse) system. To compute the RFs for each event, we deconvolved the radial component seismograms with vertical component seismograms at each station using the time-domain iterative deconvolution method (*Ligorria and Ammon*, 1999) with a Gaussian filter parameter of 2.5 (∼1.2 Hz) and 5.0 (∼2.4 Hz). All analyses were performed via Python using the open-source rf software package (*Eulenfeld*, 2020).

Before stacking the RFs, we applied a Ps phase moveout correction using the iasp91 (*Kennett and Engdahl*, 1991) model and calculated piercing points. We set the piercing point depth at 20 km based on estimates of slab depth (20–27 km) beneath the study area from the Slab2.0 model (*Hayes et al.*, 2018), created equal profile boxes along the array (Appendix 2.A Figure 2.A.3), and then stacked the receiver functions by common conversion points (Figure 2.4.1). Both the stacked 1.2 Hz and 2.4 Hz RFs were converted to depth (Figure 2.4.1b and 2.4.1c) using the rf software and the iasp91 velocity model (*Kennett and Engdahl*, 1991)

2.4.3 1-D Synthetic Modeling

To aid our interpretation, we produced synthetic RFs (assuming a ray parameter of 0.05 s/km) that tested three simple velocity-density models of the structure below Kodiak Island. Our primary goal was to evaluate resolution of hypothetical structures near the top of the subducting oceanic crust and compare with previous results from the northern 1964 rupture area. To better account for the RF variability across the Kodiak profile, we selected groups of RFs from three different sections (6-km bins, centered at 10, 22 and 32 km distance along the profile) which showed good signal-to-noise ratios (Figure 2.4.1c) and calculate uncertainties by bootstrap resampling the RFs in each bin before producing the bins' unweighted stacks. We then used the position of the slab Moho Ps arrival on the resultant stacked traces to define the slab Moho depth of the models (Figure 2.5.1a-c).

Model 1 (Appendix 2.B Table 2.B.2; Figure 2.5.1a) is a four-layer model based on the *Kim et al.* (2014) Kenai Peninsula model beneath the Kenai asperity. The model consists of a featureless upper crust, a 3 km-thick LVZ at the plate interface and an 8 km-thick oceanic crust. To construct model 2 (Appendix 2.B Table 2.B.2; Figure 2.5.1b), we removed the 3-km-thick LVZ from model 1 and calculated

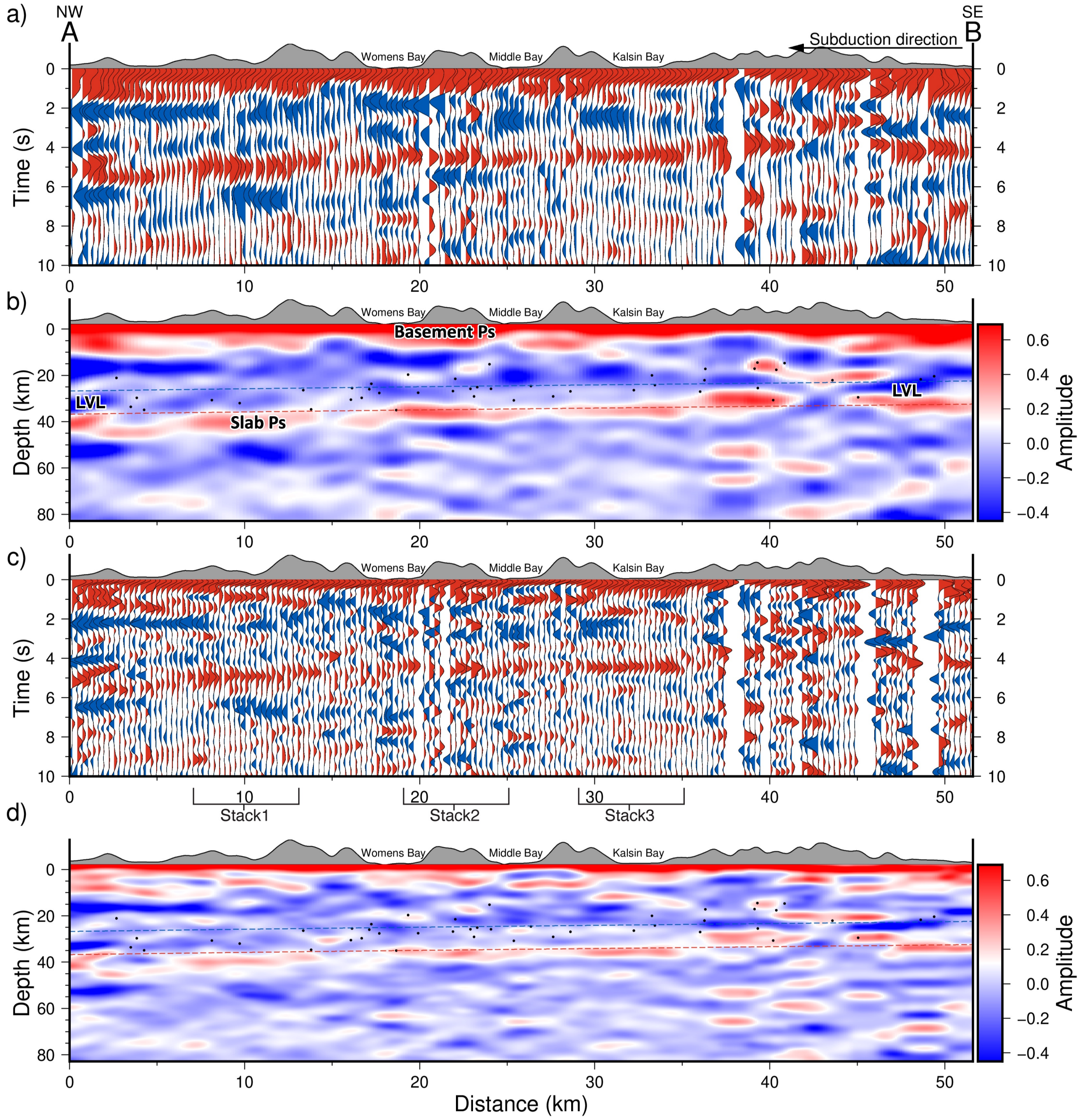

Figure 2.4.1: Receiver function profiles. (a) Stacked radial receiver functions with a Gaussian value of 2.5 (∼1.2 Hz). (b) ∼1.2 Hz CCP image for transect A-B. Note the clear lack of a low-velocity channel at the plate interface (Red = Positive, Blue = Negative). For reference, we plotted earthquakes from the AACSE catalog (black dots), the top-of-slab depth from Hayes et al. (2018) (blue dashes), and an inferred Moho surface (red dashes) assuming an 8-km thick oceanic crust. Vertical exaggeration = 0.135. (c) Stacked radial receiver functions with a Gaussian value of 5.0 (∼2.4 Hz). Stack1, Stack2 and Stack3 show the locations of the receiver functions stacked and plotted in Figure 3 to compare with synthetics. (d) ∼2.4 Hz CCP image for transect A-B. Note the clear lack of a low-velocity channel at the plate interface.

synthetics using just the featureless upper crust and the 8 km-thick oceanic crust. For Model 3 (Appendix 2.B Table 2.B.2; Figure 2.5.1c), we eliminated the 3-km LVZ and the top of the oceanic crust resulting in a simple two-layer model with one increase in velocity at the slab Moho depth.

2.5 Results

2.5.1 Receiver Function Imaging

Our final common conversion point stack produces a NW-SE-trending, approximately trench-perpendicular profile that samples a ∼50 km segment of the Alaska subduction forearc up to 80 km deep (Figure 2.4.1). Both the stacked 1.2 Hz (Figure 2.4.1a) and the stacked 2.4 Hz images (Figure 2.4.1c) show a coherent, SE to NW dipping positive conversion at ∼30–40 km depth consistent with the expected slab Moho depth from previous studies. For reference, we plotted earthquakes from the AACSE catalog (*Ruppert et al.*, 2021a,b) beneath the study area (57.40°–58.0° N, 152.083°–152.75° W) which are within one standard deviation of the mean hypocentral depth of 24.96 km on our CCP images (black dots in Figure 2.4.1b and 2.4.1d). We also plotted the top of the slab depth from *Hayes et al.* (2018) and inferred the slab Moho depth assuming an 8-km thick oceanic crust (blue and red dashed lines in Figure 2.4.1b and 2.4.1d). We do not observe a negative top-of-slab conversion above the positive slab Moho conversion.

We observe intermittent segments of shallow (above ∼10 km depth) positive conversions across the length of the profile in our high frequency (2.4 Hz) stacked image (Figure 2.4.1d). One such horizon at ∼5 km depth extends from about ∼8–12 km along the profile, and another beneath Kalsin Bay at ∼7 km depth extends from 28–35 km along the profile. Since the depths of these early arrivals vary along the line, the features generating them are likely laterally discontinuous. A mixture of the resultant reverberations and other possible primary arrivals could explain the chaotic character of the traces between ∼5 km and 35 km depths. Increasing the Gaussian value to 10 (∼4.8 Hz) sharpened the amplitudes of coherent arrivals and introduced noise that degraded prominent features such as the slab Moho Ps (Appendix 2.A Figure 2.A.4(b)).

2.5.2 Synthetic Modeling Results

Since we were only modeling the features at slab depth and only considering the upgoing Ps conversion, we calculated correlation coefficients of the predicted and the observed RFs from 2 s after the P arrival to 10 seconds after the P arrival. Model 1 (Figure 2.5.1a) produced the worst-fitting synthetics of all three models (average correlation coefficient of 0.003). Model 2 (Figure 2.5.1b) is a better fit compared to the first model (average correlation coefficient of 0.54). Model 3 (Figure 2.5.1c), the simple two-layer model with an increase in velocity at the slab Moho depth, is the best-fitting model with an average correlation coefficient of 0.59. The results suggest that the P-wave velocity (V_P), S-wave velocity (V_S) and density above the slab Moho must be uniform to obtain an optimal fit to the observed data. In other words, introducing additional features in the model above the Moho, even an oceanic crust, creates synthetics that poorly match the observational data.

2.6 Discussion

2.6.1 Absence of Oceanic Crust Arrival

In subduction zone environments, RFs are commonly used to investigate plate interface structure since the method exploits the conversion of incident P-waves from a teleseismic event to S-waves at significant seismic-velocity discontinuities. RFs have identified LVZs along the plate interfaces in subduction zones globally as

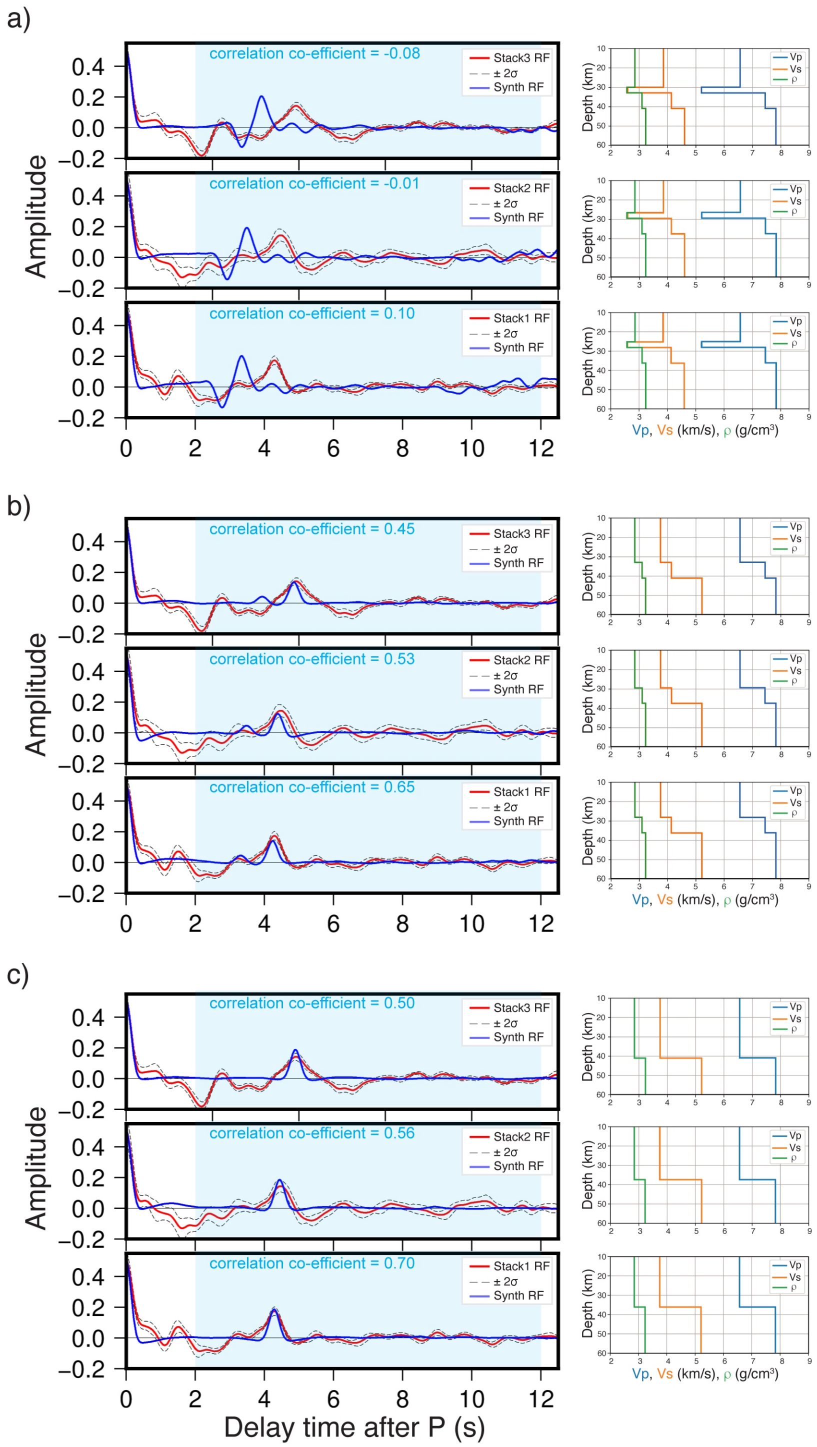

Figure 2.5.1: Synthetic tests. Each set of 3 plots represents synthetic modeling results (black dashed lines) overlaid on stacked field RFs (red lines) centered at 10 km (top), 22 km (middle) and 3 km (bottom), field RF uncertainties are plotted as black dashed lines. The right column contains the velocity models used to calculate the synthetic RFs on the left. (a) Model 1 is analogous to the Kenai observations by Kim et al. (2014). (b) Model 2 has no LVZ above the subduction slab. (c) Model 3 is the best-fitting model, it only contains the slab Moho.

negative amplitude pulses atop positive amplitude pulses at slab depth (*Audet and Kim*, 2016; *Bostock*, 2013). This dipole character has been observed in the Japan (*Akuhara et al.*, 2017; *Kawakatsu and Watada*, 2007), Cascadia (*Janiszewski and Abers*, 2015; *Ward et al.*, 2018), Costa Rica (*Audet and Schwartz*, 2013), Mariana (*Tibi et al.*, 2008), Alaska (*Ferris et al.*, 2003), and the central Mexico (*Kim et al.*, 2012; *Pérez-Campos et al.*, 2008) subduction zones. Depending on how far down dip the study area is located, the negative pulse is typically interpreted as hydrated oceanic crust or mantle hydrated by fluid expelled from the subducting slab due to the low S-wave velocities observed, while the positive amplitude pulse is generally the slab Moho. In Cascadia, *Janiszewski and Abers* (2015) interpreted the LVZ as metamorphosed sediments, while *Bangs et al.* (2009) interpreted the LVZ in Nankai as high porosity underthrust sediment. In the northern 1964 segment, *Kim et al.* (2014) also observed this typical negative-to-positive character, attributing the negative arrivals to an LVZ of subducted marine sediments along the plate interface. Neither our observed nor the preferred synthetic RFs (Figure 2.4.1 and Figure 2.5.1) feature the negative-positive dipole character observed within the northern 1964 asperity, highlighting a significant difference in RF character within the 1964 rupture area. The lack of major arrivals before the positive slab Moho phase suggests three possibilities for subsurface structure: (1) The presence of metasediments at the plate interface with seismic properties similar to the base of the upper plate and top of the subducting slab; (2) A sedimentary layer too thin to be resolved by 1.2–2.4 Hz RFs; and (3) No sediments present at the plate interface because they have been scraped off at the trench during subduction.

We rule out possibility #3 because we observe negative arrivals above the slab Moho at both ends of our profiles (Figure 2.4.1) that may suggest limited areas of low velocity at the interface, perhaps sediments. Also, plate interface material is commonly inferred from trench sediment input to the subduction zone (*Morgan*, 2004; *Underwood*, 2007) and approximately 2 km of pelagic and Surveyor Fan sediment (*Reece et al.*, 2011; *von Huene et al.*, 2012, Figure 2.2.1a) comprise the subduction input near Kodiak. It is therefore unlikely that the plate interface beneath Kodiak is devoid of sediments.

For possibility #1, we suggest that the subduction zone environment may have altered the properties of most of the subducted sediment at the interface, thus suppressing the velocity and density contrast between the sediment and the surrounding rock across most of the interface. There is ample evidence from magnetotelluric (*Heise et al.*, 2012), laboratory (*Miller et al.*, 2021) and field studies of exhumed metasedimentary rocks from subduction zone forearcs (*Rowe et al.*, 2009, 2013) pointing to instances of hundreds of meters of metamorphosed sediments lining the plate interface. It is likely that the metasedimentary rocks exhumed on Kodiak Island are close enough in seismic properties (e.g., *Miller et al.*, 2021) to the Pacific crust that there is no significant discontinuity at the interface to resolve with Ps RFs. Therefore, the absence of a well-defined LVZ channel at the plate interface beneath our study area does not necessarily mean an absence of subducted sediment. In their study of P- and S-wave velocities of exhumed Kodiak metasediments, (*Miller et al.*, 2021) reported anisotropy of $\sim$8-28% in V_p and $\sim$6.5-8% in V_s, with lower wave speeds perpendicular to the rocks' dominant fabric. This suggests an absence of foliation or obliquely foliated rocks conducive for higher wave speeds beneath our study area.

For possibility #2, while the Ps RFs presented here use relatively high frequencies for teleseismic imaging (1.2–2.4 Hz), there may be coherent structural layers that are too thin to be resolved. Using controlled source seismic reflection data, *Li et al.* (2018) estimated a thin 600–900 m low-velocity channel at shallower (8–10 km) depths along the plate interface south of Kodiak Island inside the 1938 $M_W 8.2$ Semidi rupture zone. Our synthetic test of 2.4 Hz Ps RFs showed that although we can detect a 750 m thick LVZ, it is very close to the limit of our resolution (Appendix 2.A Figure 2.A.4(a)). RFs recovered from a 500 m thick LVZ fall within 2 standard deviations (2σ) of the field data (Appendix 2.A Figure 2.A.4(a)) suggesting that, if an LVZ exists beneath our study area, it is less than 500 m thick. We also tested using higher frequency observations, 4.8 Hz, but the signal-to-noise ratio of teleseismic sources decreases and the prominent velocity increase interpreted as the slab Moho is only resolved sporadically across the array (Appendix 2.A Figure 2.A.4(b)). In areas where potential slab Moho arrivals are observed in the 4.8 Hz RF image, we still do not find evidence for an overlying LVZ (Appendix 2.A Figure 2.A.4(b)). Thus, we cannot rule out a thin LVZ (<500 m) but we can be confident that a thicker LVZ (∼3–5 km) like that imaged by (*Kim et al.*, 2014) in the Kenai asperity would be resolvable if it existed beneath our study area. (*Mann et al.*, 2022) used scattered P and S coda of teleseismic P-waves to successfully image a continuous ∼7-km thick low-velocity layer lining the top of the subducted Yakutat crust. While we see reverberations in sections of our profile, their quality is too low to allow for interpretation. The short deployment window of the Kodiak node array (∼25 days) and the limited back-azimuth distribution of the events used in this study limits the usefulness of later arrivals. We note that RF results alone cannot discriminate between possibilities #1 and #2, but with constraints from marine seismic profiles one can favor possibility #2.

2.6.2 Evidence of Rupture Across a Heterogenous Plate Interface

The simple plate interface structure beneath Kodiak compared to the more complicated plate interface structure beneath the Kenai Peninsula supports other evidence that the 1964 earthquake ruptured multiple segments across distinctive asperities. During the 1964 event, the northern Kenai asperity slipped an average of 18 m, while Kodiak slipped an average of 10 m (*Johnson et al.*, 1996). Major earthquakes in the Kenai area have a recurrence interval of 700–800 years (*Wesson et al.*, 1999) and the plate interface is strongly locked (*Zweck et al.*, 2002). In Kodiak, the major earthquake recurrence interval is 60 years (*Nishenko and Jacob*, 1990) and, while the southern end of the Kodiak interface appears strongly locked (*Li and Freymueller*, 2018), locking decreases to the north. Subduction geometry in the Kenai segment is controlled by subduction of the Yakutat microplate, a thick, buoyant oceanic plateau (*Christeson et al.*, 2010) and a thick, subducting sediment package (*Kim et al.*, 2014; *Worthington et al.*, 2012). Beneath Kenai, the plate interface dips shallowly at ∼3–4 degrees. In Kodiak, the Pacific plate subducts beneath North America at ∼8 degrees, and incoming plate structure includes ∼2.5 km-thick sediments from the distal Surveyor Fan (*Reece et al.*, 2011) and the Kodiak-Bowie seamount chain (Figure 2.2.1a).

Large megathrust earthquakes at other subduction zones, such as the 1700 M 9.0 Cascadia (*Wang et al.*, 2013), 2011 M 9.0 Tohoku-Oki (*Wei et al.*, 2012), 2004 M 9.2 Sumatra (*Chlieh et al.*, 2007), and the 2011 M 8.8 in Chile (*Lorito et al.*, 2011) events encompassed patches of slip rates different from the ambient slip rates within their rupture extents. The ubiquity of heterogeneous coseismic slip during large earthquakes further illustrates that the Great Alaska earthquake entraining multiple major segments during rupture is not unique to the Alaska subduction zone.

2.6.3 Implications for Rupture Dynamics

Since *Ruff* (1989) observed that large earthquakes occurred in subduction segments with large sediment inputs, a growing number of studies have linked the occurrence of great megathrust earthquakes with subducted sediment thickness ≥1.2 km (e.g., *Scholl et al.*, 2015; *Seno*, 2017). Many of these studies argue that, depending on the quantity and mineralogical properties of the subducted sediments, a sedimentary layer can level inter-plate relief facilitating rupture propagation over long distances

(*Ruff*, 1989). Numerical modeling (e.g., *Brizzi et al.*, 2020) suggests that a total absence of sediments at the plate interface would yield significantly smaller earthquakes (M<8.5) compared to interfaces with just a 1.5 km thick sediment layer. The 2011 M 9 Tohoku-Oki provides an example of a great earthquake that occurred with <1 km thick sediment layer at the interface (*Heuret et al.*, 2012). We did not find any published record of a great megathrust earthquake occurring at subduction zones with no trench sediment input.

In their study of Kodiak region seismicity between 1964 and 2001, *Doser et al.* (2002) found that, while most earthquakes occur within the downgoing plate, several events beneath southern Kodiak Island have depths and thrust faulting mechanisms consistent with seismicity on the interface, suggesting the existence of subducted topographic features such as seamounts from the Kodiak-Bowie chain (Figure 2.2.1a) beneath Kodiak that have not been smoothed with a thick sediment padding. Detailed seismicity studies on the Kenai Peninsula using the MOOS array show a well-defined seismic zone concentrated in the down-going plate, just below the plate boundary, that parallels the megathrust zone and is dominated by normal faulting mechanisms (*Li et al.*, 2013). In contrast to observations in the Kodiak region, active thrusting and seismicity on the plate interface itself was absent (*Li et al.*, 2013), possibly related to thick sediment subduction between the North American and Yakutat plates smoothening localized asperities and favoring uniform rupture in great earthquakes but not small heterogenous ruptures.

2.7 Conclusions

We analyzed teleseismic P waves from 398 autonomous three-component 5-Hz nodal geophones on Kodiak Island as part of the Alaska Amphibious Community Seismic Experiment. We calculated RFs with a Gaussian value of 2.5 (1.2 Hz) and a Gaussian value of 5.0 (2.4 Hz). The lower frequency (1.2 Hz) RFs were comparable to RFs from near-collocated broadband seismometers, and the higher frequency (2.4 Hz) RFs image produced more details. In both the low and high-frequency images, there is a coherent, SE to NW dipping positive phase at the expected slab Moho depth but no observable negative arrival to indicate phase conversions at the oceanic crust. To help explain the observed RFs, we calculated synthetic RFs from three 1-D models. These synthetic tests suggest that the overriding forearc material and Pacific oceanic crust have nearly identical seismic velocities and densities. We conclude that the 1964 Great Alaska Earthquake ruptured beyond the extent of the low-velocity shear zone observed in the Kenai asperity into a structural setting beneath Kodiak Island with little impedance contrast across the plate boundary interface.

2.8 Data Availability Statement

The nodal seismic data used in this study are available from the IRIS DMC (dmc.iris.edu) under the network code 8J (doi: 10.7914/SN/8J_2019). The IRIS DMC is supported by the National Science Foundation under Cooperative Support Agreement EAR-1851048. We obtained digital elevation data for Figures 1a and 1c from the GEBCO Compilation Group (doi:10.5285/a29c5465-b138-234d-e053-6c86abc040b9, last accessed August 2021). Geologic map data for Figure 1b and 1c was obtained from the USGS Scientific Investigations map 3340 (https://pubs.er.usgs.gov/publication/sim3340, last accessed August 2021).

2.9 Acknowledgements

We acknowledge that the Alaska Amphibious Community Seismic Experiment was conducted within the present, ancestral, and unceded lands and waters of the Alutiiq/Sugpiaq, Unangax, Aleut and Central Yup'ik peoples. Seismic stations on

Kodiak Island (Qikertaq) were placed within lands of the Koniag Alaska Native Regional Corporation, specifically within the lands of Ahkiok, Anton Larsen Bay, Larsen Bay, Leisnoi, Old Harbor, and Ouzinkie Alaska Native Village Corporations and Sun'aq (Kodiak City). We are grateful to these communities and cultures for the opportunity to learn about their lands and waters.

The Alaska Amphibious Community Seismic Experiment (AACSE) was funded by the NSF award OCE-1654568 to Cornell University. Nodal geophones were provided by the Incorporated Research Institutions for Seismology-Portable Array Seismic Studies of the Continental Lithosphere (IRIS-PASSCAL) Instrument Center, which is supported by the National Science Foundation's Seismological Facilities for the Advancement of Geoscience (SAGE) Award under Cooperative Support Agreement EAR-1851048. Dr. Jamie Farrell (University of Utah) provided additional nodes and assisted with logistics. This research was partially supported by EAR-1950328. The authors would also like to acknowledge Lucia Gonzales (University of Texas at El Paso), Dr. Jenny Nakai (USGS - Alaska Volcano Observatory), and Dr. Doug Wiens (Washington University in St. Louis), for their work on the node deployment. Dr. Aubreya Adams (Colgate University), Alyssa Fintel (Purdue University) and other summer undergraduate participants assisted with node retrieval and demobilization. The authors are also grateful to Dr. Daoyuan Sun, Dr. Patricia Persaud, and an anonymous reviewer for their helpful comments that improved this article.

References

Abers, G. A., A. N. Adams, P. J. Haeussler, E. Roland, P. J. Shore, S. Y. Schwartz, A. F. Sheehan, D. J. Shillington, S. Webb, and D. A. Wiens (2019), AACSE: The Alaska amphibious community seismic experiment, *EOS Trans. AGU.*

Akuhara, T., K. Mochizuki, H. Kawakatsu, and N. Takeuchi (2017), A fluid-rich layer along the Nankai trough megathrust fault off the Kii Peninsula inferred from receiver function inversion, *Journal of Geophysical Research: Solid Earth*, *122*(8), 6524–6537, doi:10.1002/2017JB013965.

Audet, P., and Y. Kim (2016), Teleseismic constraints on the geological environment of deep episodic slow earthquakes in subduction zone forearcs: A review, *Tectonophysics*, *670*, 1–15, doi:10.1016/j.tecto.2016.01.005.

Audet, P., and S. Y. Schwartz (2013), Hydrologic control of forearc strength and seismicity in the Costa Rican subduction zone, *Nature Geoscience*, *6*(10), 852–855, doi:10.1038/ngeo1927.

Ayuso, R. A., P. J. Haeussler, D. C. Bradley, D. W. Farris, N. K. Foley, and G. A. Wandless (2009), The role of ridge subduction in determining the geochemistry and Nd–Sr–Pb isotopic evolution of the Kodiak batholith in southern Alaska, *Tectonophysics*, *464*(1-4), 137–163, doi:10.1016/j.tecto.2008.09.029.

Bangs, N., G. Moore, S. Gulick, E. Pangborn, H. Tobin, S. Kuramoto, and A. Taira (2009), Broad, weak regions of the Nankai Megathrust and implications for shallow coseismic slip, *Earth and Planetary Science Letters*, *284*(1-2), 44–49, doi:10.1016/j.epsl.2009.04.026.

Barcheck, G., G. A. Abers, A. N. Adams, A. Bécel, J. Collins, J. B. Gaherty, P. J. Haeussler, Z. Li, G. Moore, E. Onyango, et al. (2020), The Alaska Amphibious Community Seismic Experiment, *Seismological Society of America*, *91*(6), 3054–3063.

Bostock, M. (2013), The Moho in subduction zones, *Tectonophysics*, *609*, 547–557, doi:10.1016/j.tecto.2012.07.007.

Brizzi, S., I. Zelst, F. Funiciello, F. Corbi, and Y. Dinther (2020), How Sediment Thickness Influences Subduction Dynamics and Seismicity, *Journal of Geophysical Research: Solid Earth*, *125*(8), e2019JB018,964, doi:10.1029/2019JB018964.

Chlieh, M., J.-P. Avouac, V. Hjorleifsdottir, T.-R. A. Song, C. Ji, K. Sieh, A. Sladen, H. Hebert, L. Prawirodirdjo, Y. Bock, and J. Galetzka (2007), Coseismic Slip and Afterslip of the Great Mw 9.15 Sumatra-Andaman Earthquake of 2004, *Bulletin of the Seismological Society of America*, *97*(1A), S152–S173, doi:10.1785/0120050631.

Christensen, D. H., and S. L. Beck (1994), The rupture process and tectonic implications of the great 1964 Prince William Sound earthquake, *Pure and Applied Geophysics*, *142*(1), 29–53.

Christeson, G. L., S. P. Gulick, H. J. van Avendonk, L. L. Worthington, R. S. Reece, and T. L. Pavlis (2010), The Yakutat terrane: Dramatic change in crustal thickness across the Transition fault, Alaska, *Geology*, *38*(10), 895–898, doi:10.1130/G31170.1.

Doser, D. I., W. A. Brown, and M. Velasquez (2002), Seismicity of the Kodiak Island Region (1964-2001) and Its Relation to the 1964 Great Alaska Earthquake, *Bulletin of the Seismological Society of America*, *92*(8), 3269–3292, doi:10.1785/0120010280.

Eulenfeld, T. (2020), rf: Receiver function calculation in seismology, *Journal of Open Source Software*, *5*(48), 1808, doi:10.21105/joss.01808.

Farris, D. W., P. Haeussler, R. Friedman, S. R. Paterson, R. Saltus, and R. Ayuso (2006), Emplacement of the Kodiak batholith and slab-window migration, *Geological Society of America Bulletin*, *118*(11-12), 1360–1376, doi:10.1130/B25718.1.

Ferris, A., G. A. Abers, D. H. Christensen, and E. Veenstra (2003), High resolution image of the subducted Pacific (?) plate beneath central Alaska, 50-

150 km depth, *Earth and Planetary Science Letters*, *214*(3-4), 575–588, doi: 10.1016/S0012-821X(03)00403-5.

Hayes, G. P., G. L. Moore, D. E. Portner, M. Hearne, H. Flamme, M. Furtney, and G. M. Smoczyk (2018), Slab2, a comprehensive subduction zone geometry model, *Science*, *362*(6410), 58–61, doi:10.1126/science.aat4723.

Heise, W., T. G. Caldwell, G. J. Hill, S. L. Bennie, E. Wallin, and E. A. Bertrand (2012), Magnetotelluric imaging of fluid processes at the subduction interface of the Hikurangi margin, New Zealand, *Geophysical Research Letters*, *39*(4), n/a–n/a, doi:10.1029/2011GL050150.

Heuret, A., C. P. Conrad, F. Funiciello, S. Lallemand, and L. Sandri (2012), Relation between subduction megathrust earthquakes, trench sediment thickness and upper plate strain, *Geophysical Research Letters*, *39*(5), n/a–n/a, doi: 10.1029/2011GL050712.

Ichinose, G., P. Somerville, H. K. Thio, R. Graves, and D. O'Connell (2007), Rupture process of the 1964 Prince William Sound, Alaska, earthquake from the combined inversion of seismic, tsunami, and geodetic data, *Journal of Geophysical Research*, *112*(B7), B07,306, doi:10.1029/2006JB004728.

Janiszewski, H. A., and G. A. Abers (2015), Imaging the Plate Interface in the Cascadia Seismogenic Zone: New Constraints from Offshore Receiver Functions, *Seismological Research Letters*, *86*(5), 1261–1269, doi:10.1785/0220150104.

Johnson, J. M., K. Satake, S. R. Holdahl, and J. Sauber (1996), The 1964 Prince William Sound earthquake: Joint inversion of tsunami and geodetic data, *Journal of Geophysical Research: Solid Earth*, *101*(B1), 523–532, doi:10.1029/95JB02806.

Kanamori, H. (1977), The energy release in great earthquakes, *Journal of Geophysical Research*, *82*(20), 2981–2987, doi:10.1029/JB082i020p02981.

Kawakatsu, H., and S. Watada (2007), Seismic Evidence for Deep-Water Transportation in the Mantle, *Science*, *316*(5830), 1468–1471, doi:10.1126/science.1140855.

Kennett, B. L. N., and E. R. Engdahl (1991), Traveltimes for global earthquake location and phase identification, *Geophysical Journal International*, *105*(2), 429–465, doi:10.1111/j.1365-246X.1991.tb06724.x.

Kim, D., K. M. Keranen, G. A. Abers, and L. D. Brown (2019), Enhanced Resolution of the Subducting Plate Interface in Central Alaska From Autocorrelation of Local Earthquake Coda, *Journal of Geophysical Research: Solid Earth*, *124*(2), 1583–1600, doi:10.1029/2018JB016167.

Kim, Y., M. S. Miller, F. Pearce, and R. W. Clayton (2012), Seismic imaging of the Cocos plate subduction zone system in central Mexico, *Geochemistry, Geophysics, Geosystems*, *13*(7), n/a–n/a, doi:10.1029/2012GC004033.

Kim, Y., G. A. Abers, J. Li, D. Christensen, J. Calkins, and S. Rondenay (2014), Alaska Megathrust 2: Imaging the megathrust zone and Yakutat/Pacific plate interface in the Alaska subduction zone, *Journal of Geophysical Research: Solid Earth*, *119*(3), 1924–1941, doi:10.1002/2013JB010581.

Li, J., G. A. Abers, Y. Kim, and D. Christensen (2013), Alaska megathrust 1: Seismicity 43 years after the great 1964 Alaska megathrust earthquake, *Journal of Geophysical Research: Solid Earth*, *118*(9), 4861–4871, doi:10.1002/jgrb.50358.

Li, J., D. J. Shillington, D. M. Saffer, A. Bécel, M. R. Nedimović, H. Kuehn, S. C. Webb, K. M. Keranen, and G. A. Abers (2018), Connections between subducted sediment, pore-fluid pressure, and earthquake behavior along the Alaska megathrust, *Geology*, *46*(4), 299–302, doi:10.1130/G39557.1.

Li, S., and J. T. Freymueller (2018), Spatial Variation of Slip Behavior Beneath the

Alaska Peninsula Along Alaska-Aleutian Subduction Zone, *Geophysical Research Letters*, *45*(8), 3453–3460, doi:10.1002/2017GL076761.

Li, Z., D. Wiens, and W. Shen (2020), Crust and Uppermost Mantle Structure of the Alaska Subduction Zone from Joint Inversion of Rayleigh Wave Dispersion and Receiver Functions, in *AGU Fall Meeting Abstracts*, vol. 2020, pp. 055–04.

Ligorria, J. P., and C. J. Ammon (1999), Iterative Deconvolution and Receiver-Function Estimation, *Bulletin of the Seismological Society of America*, *89*(5), 1395–1400.

Liu, G., P. Persaud, and R. W. Clayton (2018), Structure of the Northern Los Angeles Basins Revealed in Teleseismic Receiver Functions from Short-Term Nodal Seismic Arrays, *Seismological Research Letters*, *89*(5), 1680–1689, doi:10.1785/0220180071.

Lorito, S., F. Romano, S. Atzori, X. Tong, A. Avallone, J. McCloskey, M. Cocco, E. Boschi, and A. Piatanesi (2011), Limited overlap between the seismic gap and coseismic slip of the great 2010 Chile earthquake, *Nature Geoscience*, *4*(3), 173–177, doi:10.1038/ngeo1073.

Mann, M. E., G. A. Abers, K. A. Daly, and D. H. Christensen (2022), Subduction of an Oceanic Plateau Across Southcentral Alaska: Scattered-Wave Imaging, *Journal of Geophysical Research: Solid Earth*, *127*(1), e2021JB022,697, doi:10.1029/2021JB022697.

Miller, P. K., D. M. Saffer, G. A. Abers, D. J. Shillington, A. Bécel, J. Li, and C. Bate (2021), P- and S-Wave Velocities of Exhumed Metasediments From the Alaskan Subduction Zone: Implications for the In Situ Conditions Along the Megathrust, *Geophysical Research Letters*, *48*(20), e2021GL094,511, doi:10.1029/2021GL094511.

Morgan, J. K. (2004), Consolidation state and strength of underthrust sediments and evolution of the décollement at the Nankai accretionary margin: Results of uniaxial reconsolidation experiments, *Journal of Geophysical Research*, *109*(B3), B03,102, doi:10.1029/2002JB002335.

Nishenko, S. P., and K. H. Jacob (1990), Seismic potential of the Queen Charlotte-Alaska-Aleutian Seismic Zone, *Journal of Geophysical Research*, *95*(B3), 2511, doi:10.1029/JB095iB03p02511.

Pérez-Campos, X., Y. Kim, A. Husker, P. M. Davis, R. W. Clayton, A. Iglesias, J. F. Pacheco, S. K. Singh, V. C. Manea, and M. Gurnis (2008), Horizontal subduction and truncation of the Cocos Plate beneath central Mexico, *Geophysical Research Letters*, *35*(18), L18,303, doi:10.1029/2008GL035127.

Reece, R. S., S. P. S. Gulick, B. K. Horton, G. L. Christeson, and L. L. Worthington (2011), Tectonic and climatic influence on the evolution of the Surveyor Fan and Channel system, Gulf of Alaska, *Geosphere*, *7*(4), 830–844, doi:10.1130/GES00654.1.

Rowe, C. D., F. Meneghini, and J. C. Moore (2009), Fluid-rich damage zone of an ancient out-of-sequence thrust, Kodiak Islands, Alaska, *Tectonics*, *28*(1), n/a–n/a, doi:10.1029/2007TC002126.

Rowe, C. D., J. C. Moore, and F. Remitti (2013), The thickness of subduction plate boundary faults from the seafloor into the seismogenic zone, *Geology*, *41*(9), 991–994, doi:10.1130/G34556.1.

Ruff, L. J. (1989), Do Trench Sediments Affect Great Earthquake Occurrence in Subduction Zones?, in *Subduction Zones Part II*, pp. 263–282, Birkhäuser Basel, Basel, doi:10.1007/978-3-0348-9140-0{_}9.

Ruppert, N., G. Barcheck, and G. Abers (2021a), AACSE earthquake catalog: January-August, 2019.

Ruppert, N. A., G. Barcheck, and G. A. Abers (2021b), AACSE earthquake catalog: May-December, 2018.

Sample, J. C., and D. M. Fisher (1986), Duplex accretion and underplating in an ancient accretionary complex, Kodiak Islands, Alaska, *Geology*, *14*(2), 160–163, doi:10.1130/0091-7613(1986)14⟨160:DAAUIA⟩2.0.CO;2.

Scholl, D. W., S. H. Kirby, R. von Huene, H. Ryan, R. E. Wells, and E. L. Geist (2015), Great (*geq*Mw8.0) megathrust earthquakes and the subduction of excess sediment and bathymetrically smooth seafloor, *Geosphere*, *11*(2), 236–265, doi:10.1130/GES01079.1.

Seno, T. (2017), Subducted sediment thickness and M w 9 earthquakes, *Journal of Geophysical Research: Solid Earth*, *122*(1), 470–491, doi:10.1002/2016JB013048.

Suito, H., and J. T. Freymueller (2009), A viscoelastic and afterslip postseismic deformation model for the 1964 Alaska earthquake, *Journal of Geophysical Research: Solid Earth*, *114*(B11), doi:10.1029/2008JB005954.

Tibi, R., D. A. Wiens, and X. Yuan (2008), Seismic evidence for widespread serpentinized forearc mantle along the Mariana convergence margin, *Geophysical Research Letters*, *35*(13), L13,303, doi:10.1029/2008GL034163.

Underwood, M. B. (2007), Sediment Inputs to Subduction Zones: Why lithostratigraphy and clay mineralogy matter, in *The Seismogenic Zone of Subduction Thrust Faults*, pp. 42–85, Columbia University Press, doi:10.7312/dixo13866-003.

von Huene, R., J. J. Miller, and W. Weinrebe (2012), Subducting plate geology in three great earthquake ruptures of the western Alaska margin, Kodiak to Unimak, *Geosphere*, *8*(3), 628–644, doi:10.1130/GES00715.1.

Wang, P.-L., S. E. Engelhart, K. Wang, A. D. Hawkes, B. P. Horton, A. R. Nelson, and R. C. Witter (2013), Heterogeneous rupture in the great Cascadia earthquake of 1700 inferred from coastal subsidence estimates, *Journal of Geophysical Research: Solid Earth*, *118*(5), 2460–2473, doi:10.1002/jgrb.50101.

Ward, K. M., and F. C. Lin (2017), On the viability of using autonomous three-component nodal geophones to calculate teleseismic ps receiver functions with an application to old faithful, Yellowstone, *Seismological Research Letters*, *88*(5), 1268–1278, doi:10.1785/0220170051.

Ward, K. M., F. Lin, and B. Schmandt (2018), High-Resolution Receiver Function Imaging Across the Cascadia Subduction Zone Using a Dense Nodal Array, *Geophysical Research Letters*, *45*(22), 218–12, doi:10.1029/2018GL079903.

Wei, S., R. Graves, D. Helmberger, J.-P. Avouac, and J. Jiang (2012), Sources of shaking and flooding during the Tohoku-Oki earthquake: A mixture of rupture styles, *Earth and Planetary Science Letters*, *333-334*, 91–100, doi:10.1016/j.epsl.2012.04.006.

Wesson, R. L., A. D. Frankel, C. S. Mueller, and S. C. Harmsen (1999), Probabilistic seismic hazard maps of Alaska, *US Geol. Surv. Open-File Rept. 99*, *36*, 20.

Wilson, F. H., C. P. Hults, C. G. Mull, and S. M. Karl (2015), Geologic map of Alaska, *Tech. rep.*, Reston, VA, doi:10.3133/sim3340.

Worthington, L. L., H. J. A. Van Avendonk, S. P. S. Gulick, G. L. Christeson, and T. L. Pavlis (2012), Crustal structure of the Yakutat terrane and the evolution of subduction and collision in southern Alaska, *Journal of Geophysical Research: Solid Earth*, *117*(B1), n/a–n/a, doi:10.1029/2011JB008493.

Zweck, C., J. T. Freymueller, and S. C. Cohen (2002), Three-dimensional elastic dislocation modeling of the postseismic response to the 1964 Alaska earthquake, *Journal of Geophysical Research: Solid Earth*, *107*(B4), 1–1, doi:10.1029/2001JB000409.

Appendix

2.A Supplementary Figures

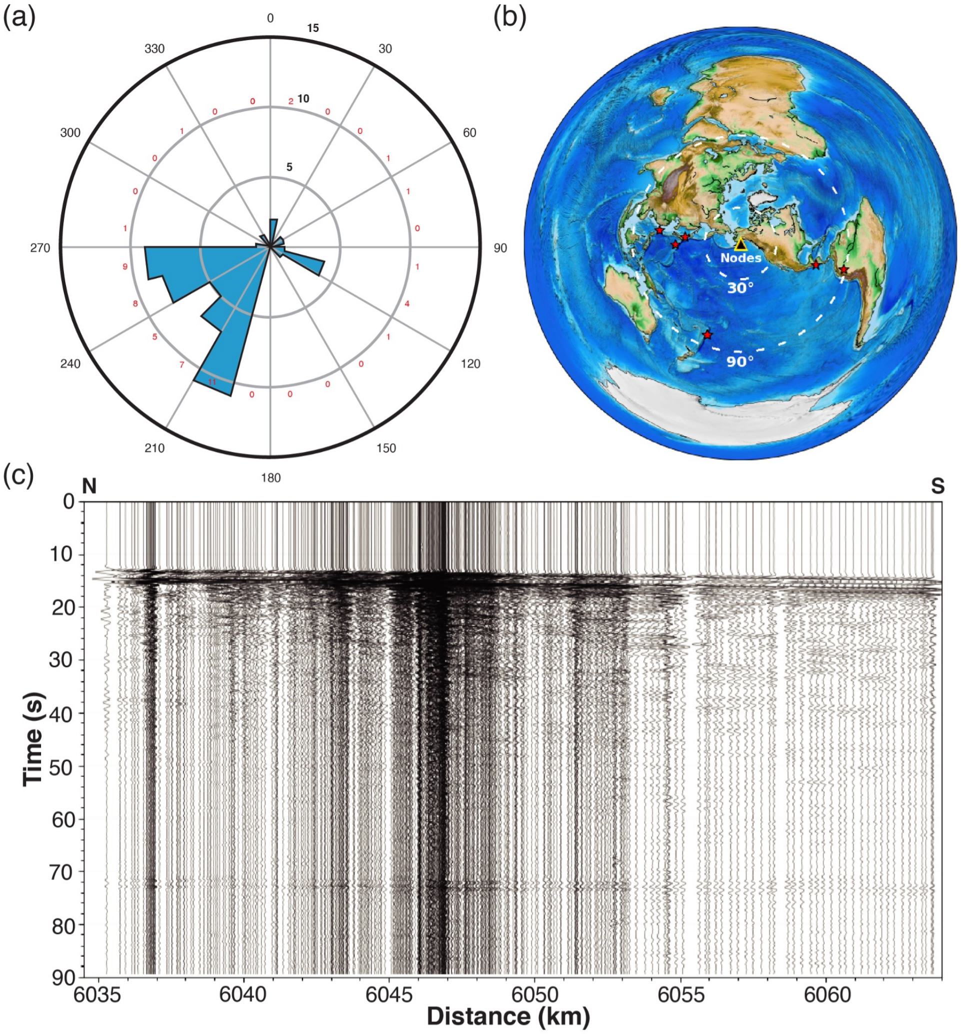

Figure 2.A.1: (a) Back azimuthal distribution of teleseismic events >5.0 MW within the 30° – 90° distance window, occurring between May 23, 2019, and June 17, 2019. (b) Location of the 7 events selected for receiver function calculation. (c) Record section plot of one of the events used for receiver function calculation after instrument response removal, and a bandpass filter (0.2-2 Hz). Amplitudes normalized with each trace. This M_W6.3 occurred on 04 June 2019, 04:39:17 UTC at ∼430 km depth southeast of Honshu, Japan.

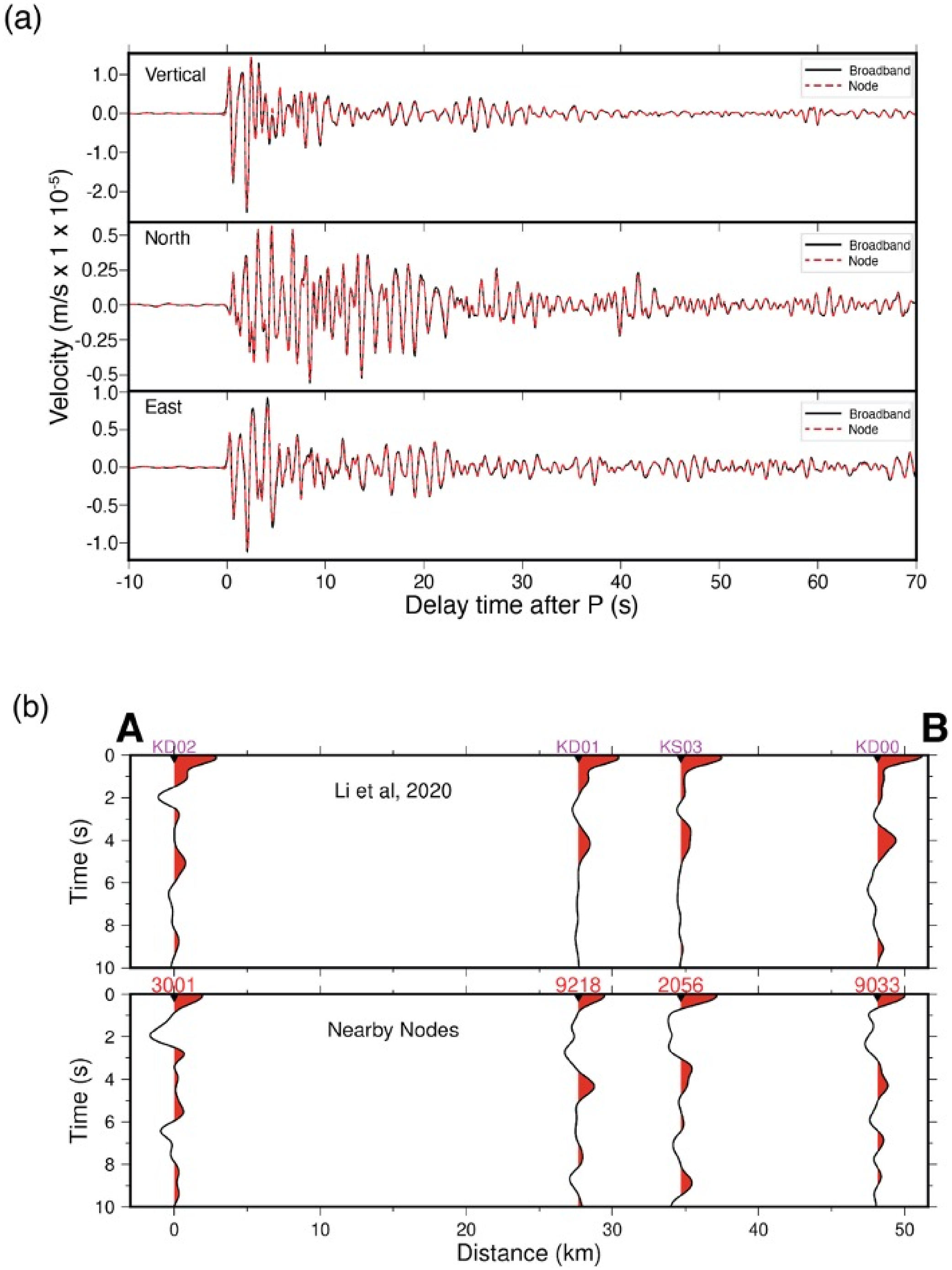

Figure 2.A.2: Comparison of near co-located nodal and broadband station waveforms. (a) Plots of node station 3001 and broadband station KD02 vertical, east, north component recordings of the 04 June 2019, 04:39:17 UTC Event shown in Appendix 2.A Figure 2.A.1 part c. (b) Plot of the average radial receiver functions for stations KD02, KD01, KS03 and KD00 calculated by Z. Li et al., (2020) projected onto transect AB (top). Plot of the average radial receiver functions calculated from near-colocated nodal station 3001, 9218, 2056 and 9033 projected onto transect AB.

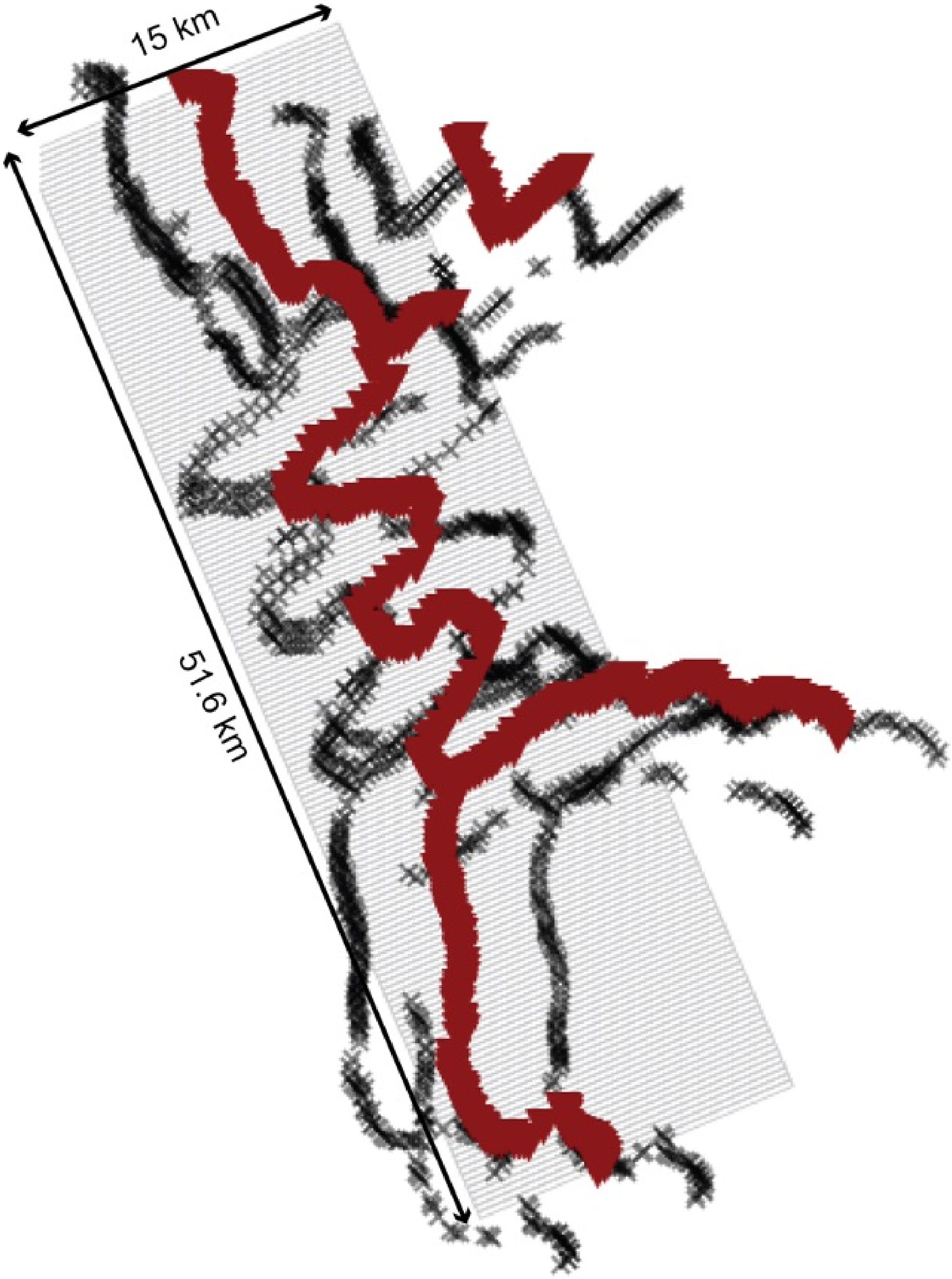

Figure 2.A.3: Map of piercing points (black stars) at 20 km depth, and the stations (red inverted triangles) used for common conversion point stacking. The grey rectangles show the position of all the profile boxes used in the stacking.

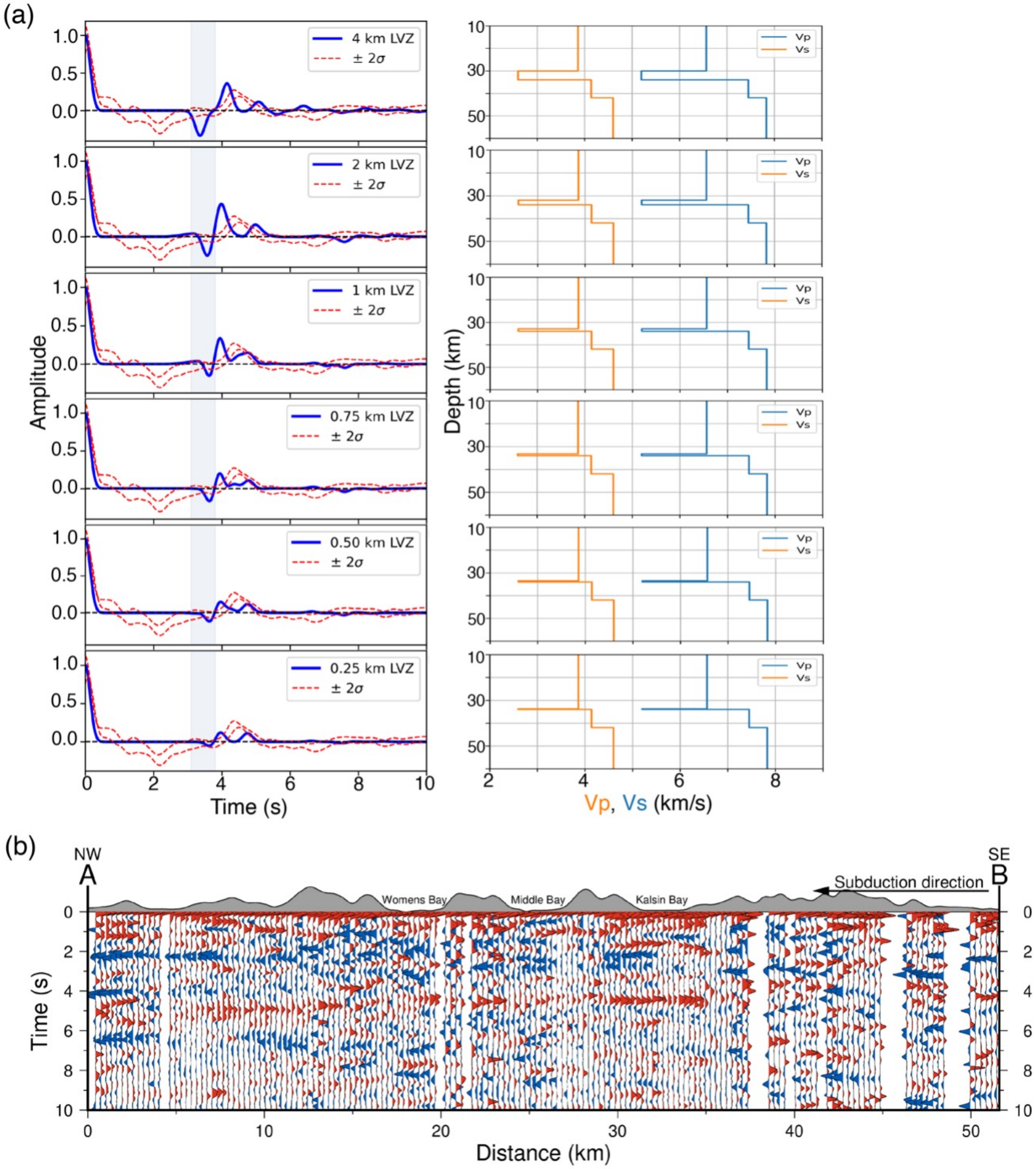

Figure 2.A.4: (a) Synthetic tests of 2.5 Hz Ps RFs for models with different LVZ thicknesses. The vertical light blue rectangles in the left panel mark the position of the negative conversion for the 4-km thick LVZ in the top seismogram. The blue lines are synthetic waveforms, and the red dashed lines are the averages of the standard deviations of the field data from Figure 2.5.1. (b) Moveout-corrected radial receiver functions with a Gaussian value of 10 (∼4.8 Hz) stacked by common conversion point.

2.B Supplementary Tables

Time	**Latitude**	**Longitude**	**Depth (km)**	**Magnitude**
2019/06/18 13:22:19	38.637	-139.4804	12	6.4
2019/06/15 21:56:11	-21.1807	-174.169	13	6.1
2019/06/04 09:46:18	22.8813	121.6704	10	5.6
2019/06/04 04:39:18	29.0623	139.2932	430.3	6.3
2019/06/02 10:36:30	-21.2091	-173.9076	10	6.0
2019/05/26 07:41:15	-5.8132	-75.2775	122.4	8.0
2019/05/30 09:03:29	13.1462	-89.3663	25	6.6

Table 2.B.1: Events used in this study

Model1	**VP (km/s)**	**Vs(km/s)**	**VP/VS**	**Density (g/cm^3)**
Layer1	6.57	3.86	1.7	2.85
Layer2	5.20	2.60	2.0	2.57
Layer3	7.45	4.14	1.8	3.11
Layer4	7.83	4.61	1.7	3.23
Model2	**VP (km/s)**	**Vs(km/s)**	**VP/VS**	**Density (g/cm^3)**
Layer1	6.57	3.75	1.75	2.85
Layer2	7.45	4.14	1.8	3.11
Layer3	7.83	5.22	1.50	3.23
Model3	**VP (km/s)**	**Vs(km/s)**	**VP/VS**	**Density (g/cm^3)**
Layer1	6.57	3.75	1.75	2.85
Layer2	7.83	5.22	1.50	3.23

Table 2.B.2: One-Dimensional model parameters

3 Geometry and Subsurface Characterization of the Raton Basin using Teleseismic Receiver Functions

Authors and Affiliations

Evans A. Onyango[1*]

Brandon Schmandt[1]

Lindsay L. Worthington[1]

[1]Dept. of Earth and Planetary Sciences, University of New Mexico, Albuquerque, New Mexico, USA

*Corresponding author

Modified from a manuscript to be submitted to a *peer-reviewed journal*

3.1 Abstract

We conduct a multiscale investigation of Raton Basin structure with teleseismic receiver function analysis of data recorded by broadband and nodal geophones. The 9-station broadband array spaced at ∼30 km provides a coarse overview of the Raton Basin region and the 96-station nodal geophone array spaced at ∼3 km provides a higher resolution image in the basin's interior. Our results show a basin-wide velocity increase at depth ∼2 km, consistent with the depth of the top of the Early Cretaceous-age Dakota Formation. These findings support earlier controlled source reflection evidence that the top of the Dakota Formation boundary exhibits larger and more coherent impedance contrast than the top of the Precambrian basement in the northern basin. The new results show that the top of the Dakota Formation is the most prominent seismic boundary across the basin. Local earthquakes previously attributed to reactivated basement faults occur ∼1.4

km deeper than the Dakota formation, suggesting that seismicity extends from near the sediment-basement boundary into the Precambrian basement.

3.2 Introduction

Located on the Colorado-New Mexico border, the Raton Basin hosted just two M>3 earthquakes between January 1, 1970 and January 1, 1999 (*USGS*, 2022, Figure 3.2.1a), both events occurred in the Colorado portion (northern half) of the Raton Basin (Figure 3.2.1a). Since wastewater injection related to coalbed methane production began in 1999 there has been significant increase in seismicity in both halves of the Basin (*Rubinstein et al.*, 2014). A total of 19 M>3 events occurred in the basin between 1999 and 2022(*USGS*, 2022, Figure 3.2.1b), representing an over nine-fold increase in seismicity in roughly the same amount of time (*Glasgow et al.*, 2021; *Nakai et al.*, 2017; *Rubinstein et al.*, 2014).

The sudden increase in seismicity has been attributed to the injection up to 153,633 m^3/month (*Wang et al.*, 2020) of wastewater by wells drilled 1–2 km (*Wang et al.*, 2020; *Weingarten*, 2015) above the Precambrian basement. *Nakai et al.* (2017) posited the existence of faults extending from the basement into the basin sediment packages as the likely mode of transmittance of pore fluid pressure into the basement. In this model, the recent increase in seismicity reflects reactivation of basement faults. However, the depth of the Precambrian basement and major sedimentary boundaries are not well known throughout the basin so the geologic setting of the earthquakes is uncertain. In particular, it is unclear if seismically reactivated basement faults extend upward across the sediment-basement boundary and could serve as conduits for pore fluid pressure diffusion. Most of the wells do not reach the Precambrian basement, and most of the publicly available industry well logs do not provide comprehensive lithostratigraphy data from the surface to

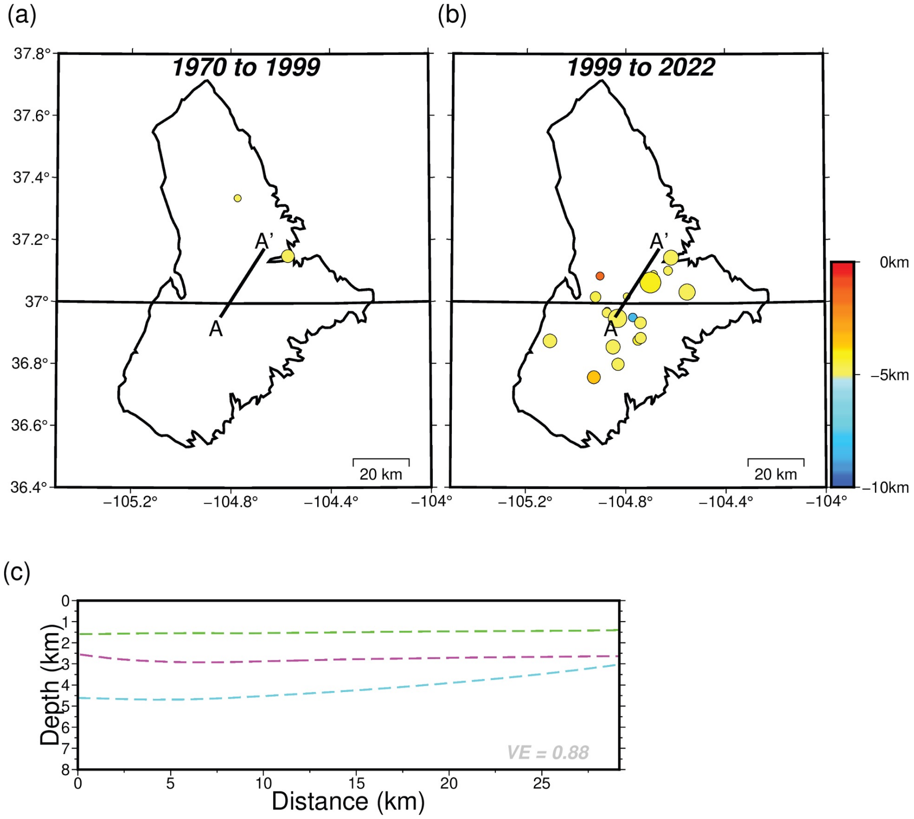
(a)
(b)
1970 to 1999
1999 to 2022
37.8°
37.6°
37.4°
37.2°
37°
36.8°
36.6°
36.4°
−105.2°
−104.8°
−104.4°
−104°
A
A'
20 km
0km
−5km
−10km
(c)
Depth (km)
0
1
2
3
4
5
6
7
8
VE = 0.88
0
5
10
15
20
25
Distance (km)

Figure 3.2.1: USGS earthquake locations of events M>3 in the Raton Basin. (a) Location of events occurring between January 01, 1970 and January 01, 1999. (b) Location of events occurring between January 01, 1999 and January 01, 2022. (c) Cross section of transect A-A'. Top of the Dakota formation (green dashed line) and top of the Precambrian basement (magenta dashed line) modified from Weingarten (2015) plotted for reference. The top of Precambrian basement estimated from Mooney and Kaban (2010) (cyan dashed line) is also plotted for comparison. Note the ∼2km difference in the predicted basement depths on western end of the transect.

the basement. Currently available estimates of the Precambrian basement depths diverge by up to 2 km in some areas (e.g., *Mooney and Kaban*, 2010; *Weingarten*, 2015, Figure 3.2.1c).

In this study, we use teleseismic waveforms recorded by 9 broadband stations and 96 nodal geophones from different deployments to determine the geometry of impedance boundaries within the basin. We employ a grid search method to estimate depths of sedimentary strata and the transition to the crystalline basement and determine V_P/V_S within basin layers. Further, we compare our results with well

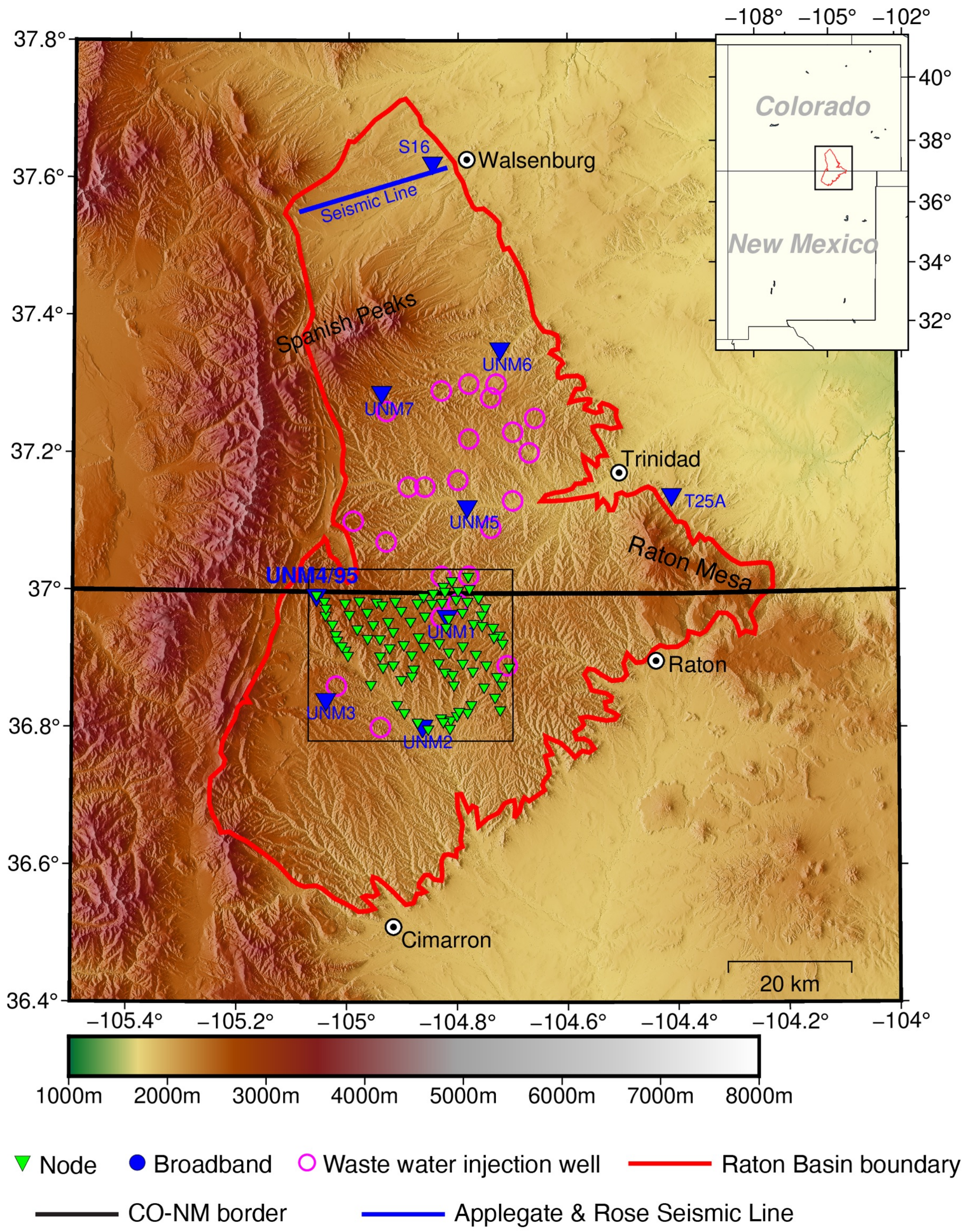

37.8°
37.6°
37.4°
37.2°
37°
36.8°
36.6°
36.4°
−105.4°
−105.2°
−105°
−104.8°
−104.6°
−104.4°
−104.2°
−104°
−108°
−105°
−102°
40°
38°
36°
34°
32°
Colorado
New Mexico
S16
Walsenburg
Seismic Line
Spanish Peaks
UNM6
UNM7
Trinidad
T25A
UNM5
Raton Mesa
UNM4/95
UNM1
Raton
UNM3
UNM2
Cimarron
20 km
1000m
2000m
3000m
4000m
5000m
6000m
7000m
8000m
Node
Broadband
Waste water injection well
Raton Basin boundary
CO-NM border
Applegate & Rose Seismic Line

Figure 3.2.2: Shaded relief map of the Raton Basin in New Mexico and Colorado and the study area.

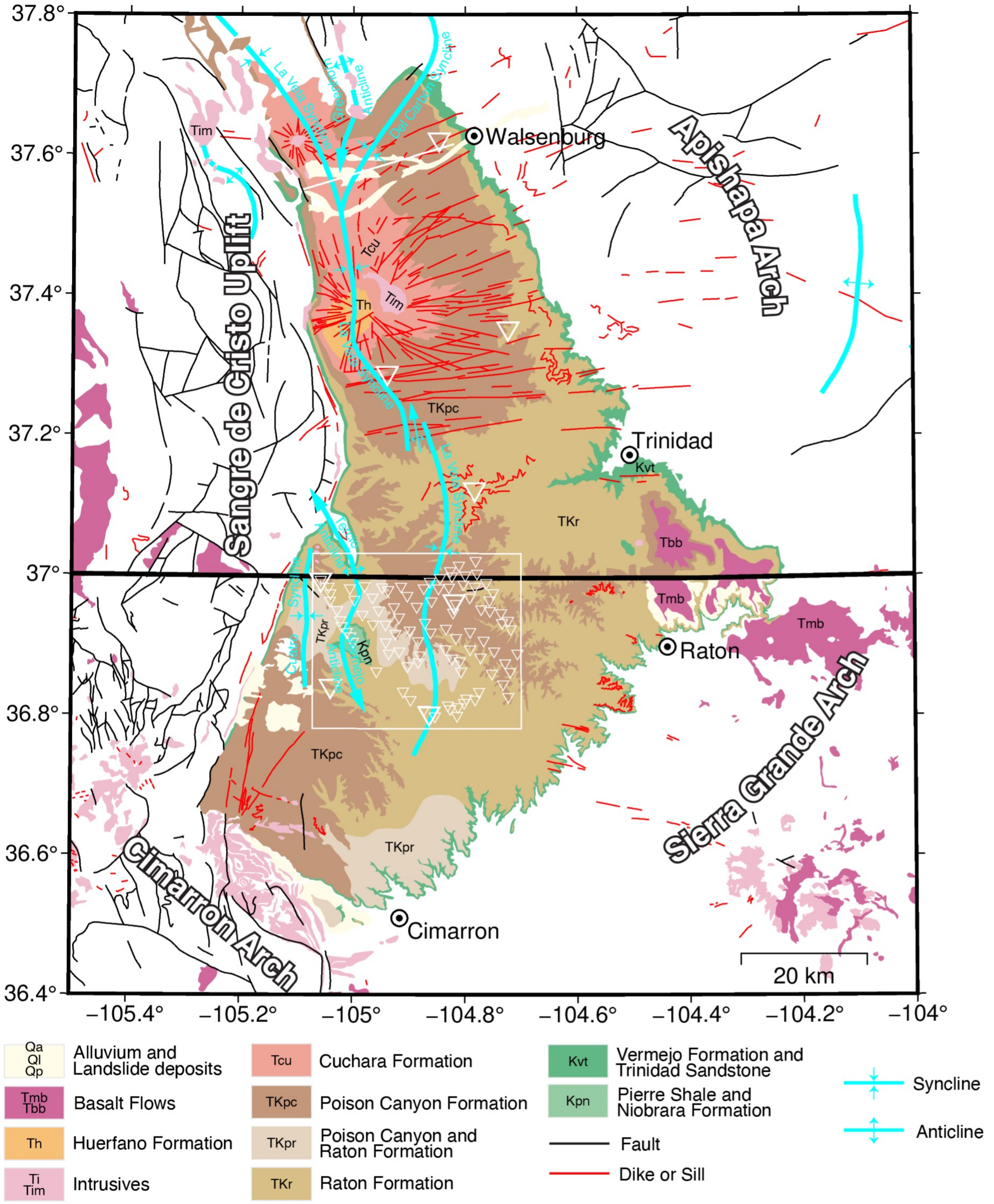
37.8°
37.6°
37.4°
37.2°
37°
36.8°
36.6°
36.4°
−105.4°
−105.2°
−105°
−104.8°
−104.6°
−104.4°
−104.2°
−104°
Walsenburg
Trinidad
Raton
Cimarron
Sangre de Cristo Uplift
Apishapa Arch
Sierra Grande Arch
Cimarron Arch
La Veta Syncline
Greenhorn Anticline
Del Carbon Syncline
Tim
Tcu
Th
TKpc
TKr
Kvt
Tbb
Tmb
TKpr
Kpn
20 km
Qa Ql Qp
Alluvium and Landslide deposits
Tmb Tbb
Basalt Flows
Th
Huerfano Formation
Ti Tim
Intrusives
Tcu
Cuchara Formation
TKpc
Poison Canyon Formation
TKpr
Poison Canyon and Raton Formation
TKr
Raton Formation
Kvt
Vermejo Formation and Trinidad Sandstone
Kpn
Pierre Shale and Niobrara Formation
Fault
Dike or Sill
Syncline
Anticline

Figure 3.2.3: Composite map of the geology and structural geology of the Raton Basin region. New Mexico geology from the Bureau of Geology and Mineral Resources (2003) and Colorado geology from Tweto (1979). See references for geologic unit explanation.

data near the seismic stations and earthquake hypocenters from a dense seismic array in the central Raton Basin to evaluate the geologic setting of reactivated faults.

3.3 Geologic Background and Previous Geophysical Studies

The Raton Basin is an arcuate sedimentary basin, bisected by the Colorado-New Mexico border. The northern lobe is in Colorado and trends to the southeast while the southern lobe is in New Mexico and trends to the northeast (Figure 3.2.2). The Basin is bounded by Sangre de Cristo Uplift to the east, the Cimarron Arch to the south, Sierra Grande Arch to the southeast and the Apishapa Arch to the northeast (Figure 3.2.3). A sequence of Devonian through Quaternary strata overlies the Precambrian basement (*Johnson and Finn*, 2001). Notable formations include the early Cretaceous Dakota formation, the late Cretaceous Trinidad sandstone and the late Cretaceous Raton formation. A wide array of igneous rocks and structures dominate the Colorado half of the basin. The largest igneous bodies are the two Spanish Peaks (*Las Cumbres Españolas* in Spanish) which stand >1900 m above surrounding relief (*Johnson*, 1968). An intrusive network of dikes radiates from the Spanish Peaks extending across the northern half of the basin and terminates at eastern edge. Extrusive basalt lava sheets cover the eastern tip of the Basin near Trinidad, Colorado (*Hemborg*, 1998, Figure 3.2.3).

Prior to this study, (*Mooney and Kaban*, 2010) compiled industry and regional map data (e.g., *Frezon et al.*, 1983; *Jachens and Moring*, 1990; *Jachens et al.*, 1995) to estimate the thickness and density of sediment cover in North America. Their final map yielded thickness spaced at 30 arc-seconds (1 km). For the Raton Basin, their results show sediments thickening westwards to a maximum of ∼5 km (*Mooney and Kaban*, 2010, Figure 3.3.1).

Petroleum exploration 2D seismic lines, primarily taken in the 1980s (e.g., *Applegate and Rose*, 1985, Figure 3.3.2), show two consistent, high amplitude reflectors spanning the northernmost section of the Raton Basin near Walsenburg and XP station S16 (Figures 3.2.1,3.3.2). In these legacy seismic records, the shallowest reflector (e.g., at 1 s in Figure 3.3.1) is interpreted to be the top of the Trinidad sandstone. The second prominent reflector (e.g., at 1.6 s in Figure 3.3.1) is interpreted to be a composite event comprising the Dakota, Purgatoire and the Entrada Formation complex. Later in the section (e.g., at 2.2 s in Figure 3.3.1), a lower amplitude, discontinuous reflector is interpreted as the Paleozoic-age sedimentary sequence that overlies the crystalline basement.

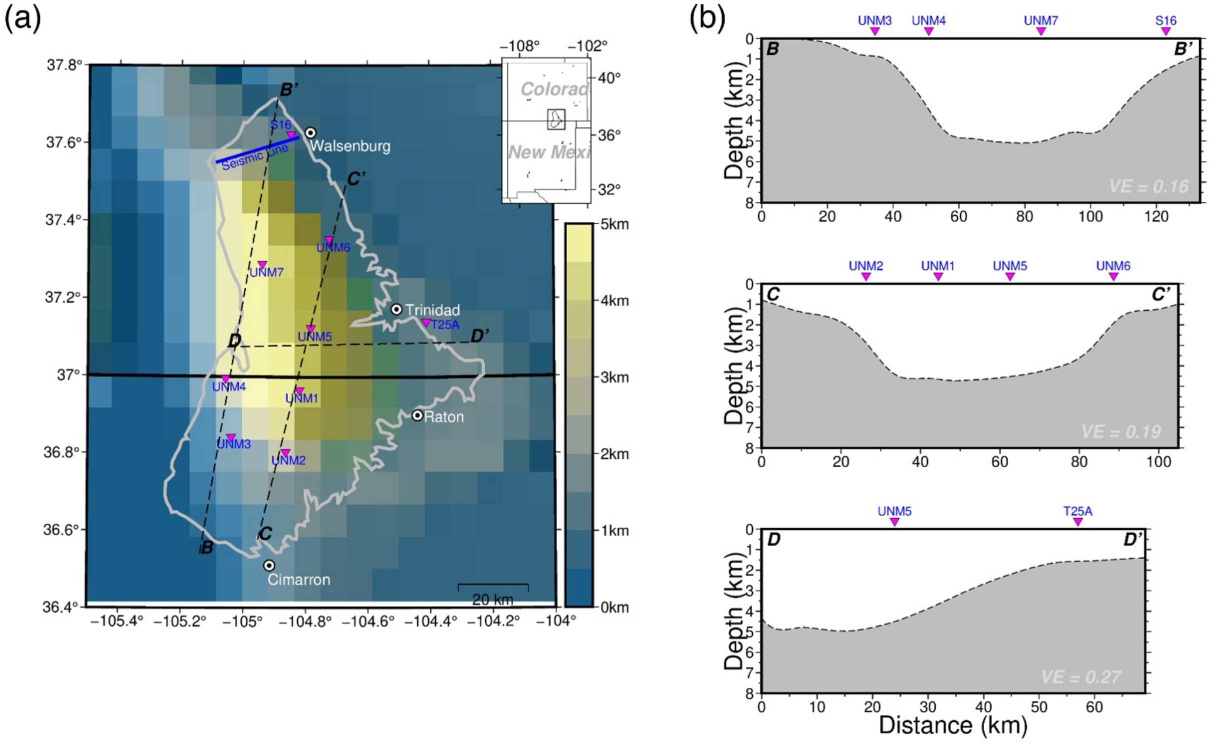
(a)
(b)
37.8°
37.6°
37.4°
37.2°
37°
36.8°
36.6°
36.4°
−105.4° −105.2° −105° −104.8° −104.6° −104.4° −104.2° −104°
−108° −102°
40°
36°
32°
Colorad
New Mexi
B
B'
C
C'
D
D'
S16
Seismic Line
Walsenburg
UNM6
UNM7
Trinidad
T25A
UNM5
UNM4
UNM1
Raton
UNM3
UNM2
Cimarron
20 km
5km
4km
3km
2km
1km
0km
UNM3 UNM4 UNM7 S16
Depth (km)
VE = 0.16
UNM2 UNM1 UNM5 UNM6
VE = 0.19
UNM5 T25A
VE = 0.27
Distance (km)

Figure 3.3.1: Mooney & Kaban (2010)'s sedimentary thickness estimates and broadband station locations. (a) Black dashed lines are B-B', C-C', D-D' profile location that are near the broadband array stations and also gives an ideas of basin structure. (b) Cross-sections of profiles B-B', C-C' and D-D' shown in (a).

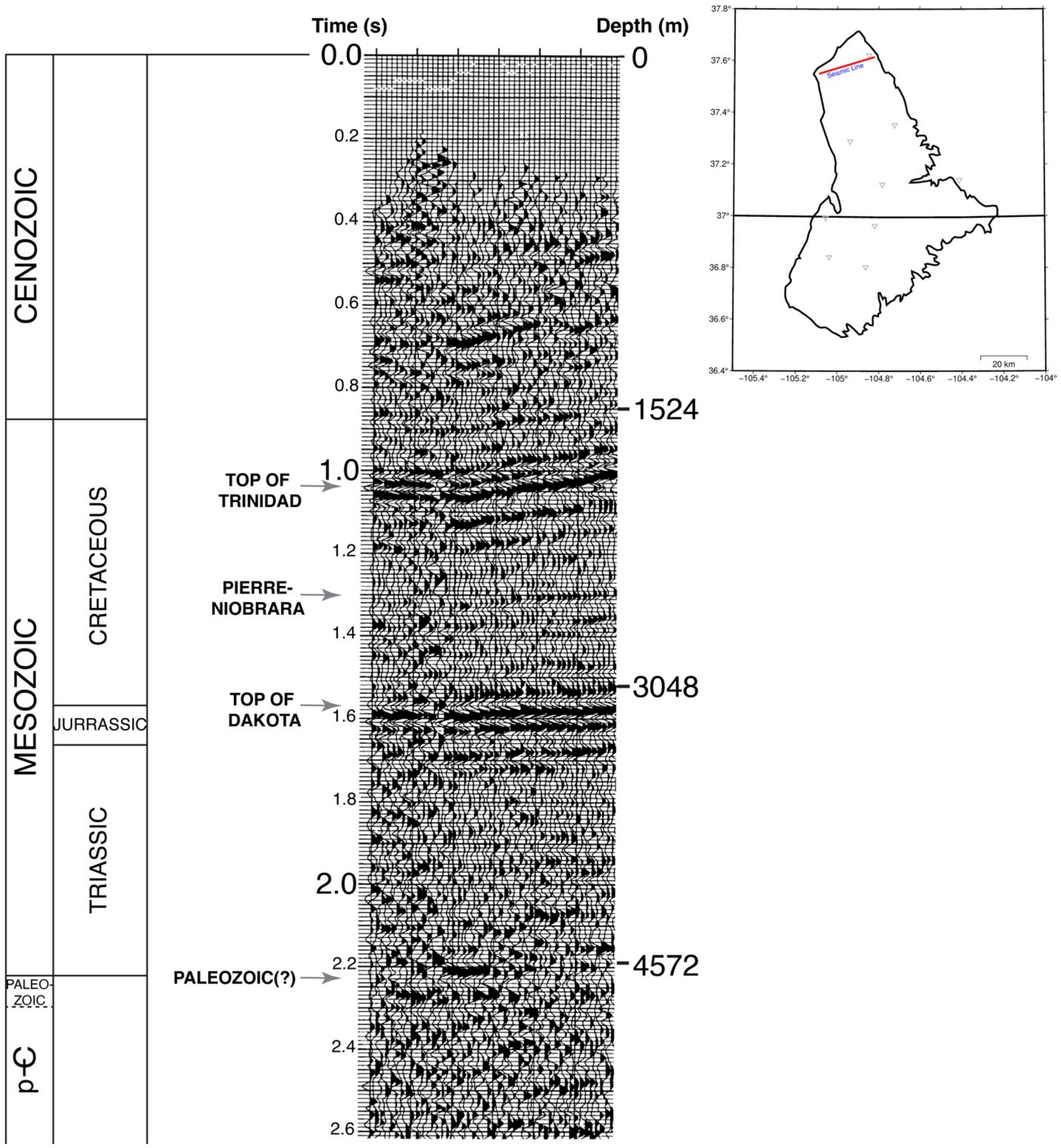

Figure 3.3.2: Modified from Applegate & Rose (1985). Seismic correlation chart for the northern Raton Basin. Notice that the top of Trinidad and top of Dakota reflectors are more clearly defined than the Precambrian basement. See Figure 3.4.10 for the complete 2D seismic profile.

Network	Station	Latitude	Longitude	Events
YX	UNM1	36.9618	-104.8192	77
YX	UNM2	36.8021	-104.8636	52
YX	UNM3	36.8408	-104.0391	77
YX	UNM4	36.9925	-104.0565	87
YX	UNM5	37.1220	-104.7829	62
YX	UNM6	37.3517	-104.7232	36
YX	UNM7	37.2878	-104.9389	82
TA	T25A	37.1388	-104.4108	107
XP	S16	37.6218	-104.8465	19

Table 3.3.1: Summary of broadband array and number of events used in analysis

3.4 Data and methods

3.4.1 Broadband Data and Processing

We use data from 9 broadband stations located ∼30 km apart, deployed over different time periods. The UNM network YX consisted of 7 stations deployed in 2016 in both halves of the Raton Basin (Table 3.3.1; Figure 3.2.2). In addition, we used data from Earthscope TA station T25A deployed from 2008 to 2019 near Trinidad, Colorado (Figure 3.2.2), and one station (S16) deployed from August 2008 to December 2009 near Walsenburg, Colorado (Figure 3.2.2). Except for station S16 which recorded continuously at a sampling rate of 40 Hz, all the other stations recorded continuously at 100 Hz. All broadband waveform data are publicly available via the IRIS DMC.

To ensure an identifiable incident P-arrival for the broadband array, we processed teleseismic events with magnitude of 6.0 or greater that met the following selection criteria: (a) a magnitude of 6.0 or greater, (b) a 25°–99° epicentral distance from the central station of each network, and (c) a clear P-arrival from visual inspection. Before calculating RFs, we windowed the seismograms from 50 s before to 150 s after the theoretical P arrival, removed their mean, detrended them and finally removed the instrument response.

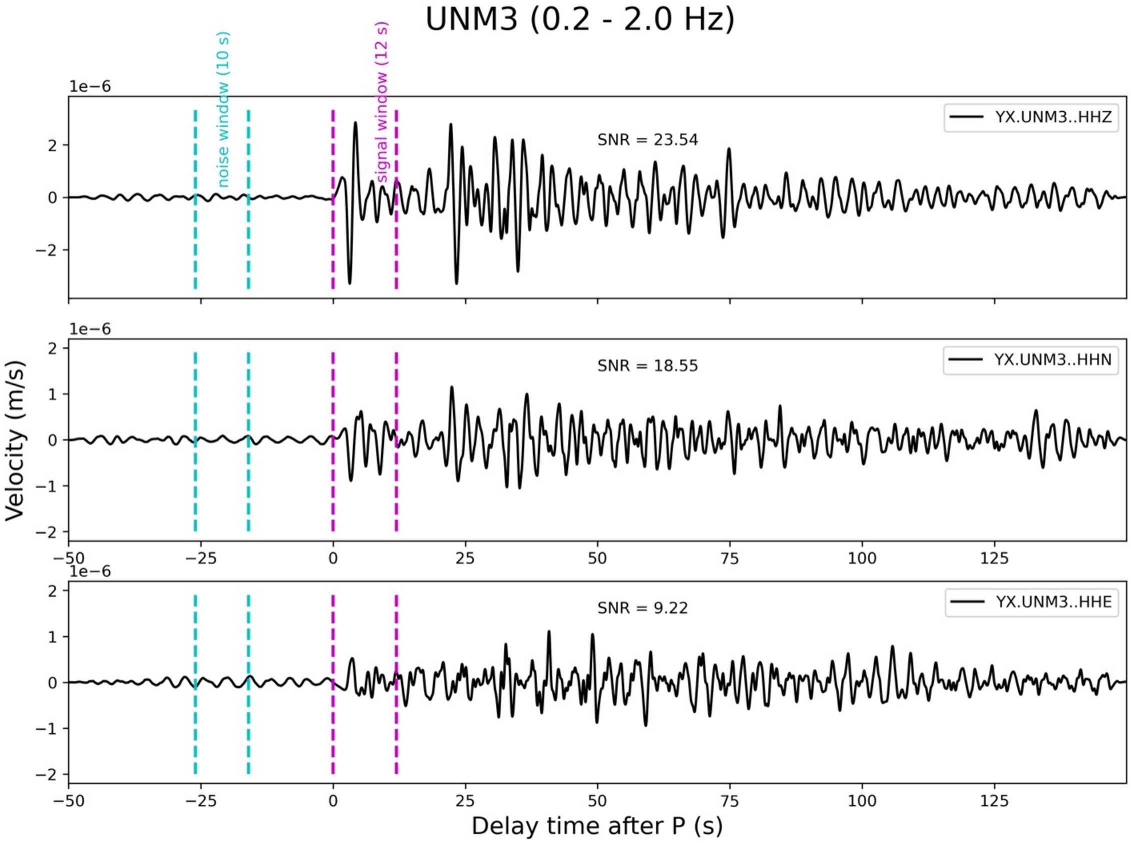

Figure 3.4.1: Plot showing time windows used to calculate the signal-to-noise ratio.

After the above preprocessing, we culled additional noisy signals by applying a signal-to-noise (SNR) based noise reduction system which eliminated traces with SNR<10 on the vertical component or SNR<5 on the north component. Figure 3.4.1 shows an example of the noise and signal windows used for SNR calculation. The selection process yields 299 events (see Appendix 3.A Figure 3.A.1 for their distribution) for RF calculation. Selected waveforms were filtered using a high-pass filter with a corner frequency of 0.03 Hz to remove long-period signals and tapered using a 5% Hanning window to minimize filtering artifacts.

3.4.2 Nodal Data and Processing

The node array comprised 96 FairfieldNodal autonomous node sensors with three-component 5 Hz geophones. Sensors were deployed near the center of the

Basin (Figure 3.2.2) at a spacing of ∼2–5 km from May to June of 2018. The stations recorded continuously at a sampling rate of 250 Hz. All continuous waveform data from the node array are publicly available in PH5 format via IRIS Data Services (network code 4E from 2018).

Since the nodal geophones were deployed for only 34 days (May 05, 2018 to June 15, 2018), we adjusted the event selection criteria to include events M>5, SNR>2 on the vertical component and SNR>1.25 on the north component. The other preprocessing steps remained the same as for the broadband array. The selection process yielded 6 events (see Appendix Figure 3.A.2 for their distribution) for RF calculation.

We validated our raw nodal waveform processing by fetching waveforms for the selected events recorded by the broadband stations within the node array footprint and comparing the preprocessed time series (Figure 3.4.2).

Well	**Latitude(°)**	**Longitude(°)**	**Elevation (m)**	**Dakota Elevation (m)**	**Thickness to Dakota (m)**
Apache Canyon 10-3	37.1	-104.99	2637	676	1961
Apache Canyon 19-10	37.07	-104.93	2241	554	1687
Beardon	37.25	-104.66	2296	797	1499
Cimarron	37.26	-104.93	2421	307	2114
Cottontail Pass	37.22	-104.78	2269	522	1747
Del Agua	37.28	-104.74	2292	561	1731
Ferminia	37.29	-104.83	2237	402	1835
Hill Ranch Deep	37.09	-104.74	2151	690	1461
Jarosa	37.3	-104.78	2159	495	1664
La Garita	37.16	-104.8	2182	558	1624
Lopez Canyon	37.15	-104.89	2205	453	1752
Polly	37.23	-104.7	2127	703	1424
Sawtooth	37.2	104.67	2047	751	1323
Southpaw	37.3	-104.73	2156	560	1596
VPA A 007	36.96	-104.83	2522	571	1951
VPA A 042	36.96	-104.83	2527	576	1951
VPA A 182	36.98	-104.8	2468	629	1839
VPA A 500	36.89	-104.71	2429	767	1662
VPR B 027	36.8	-104.94	2460	529	1931
VPR C 14	37.02	-104.78	2353	635	1718
VPR C 204	37.02	-104.83	2244	603	1641
VPR C 39	37.02	-104.78	238	635	1745
VPR D 025	36.86	-105.02	2606	649	1957
Weston	37.15	-104.86	2148	471	1677
Wild Boar	37.13	-104.7	1986	731	1255

Table 3.4.1: List of injection wells used in this study. Highlighted wells were used for groundtruthing

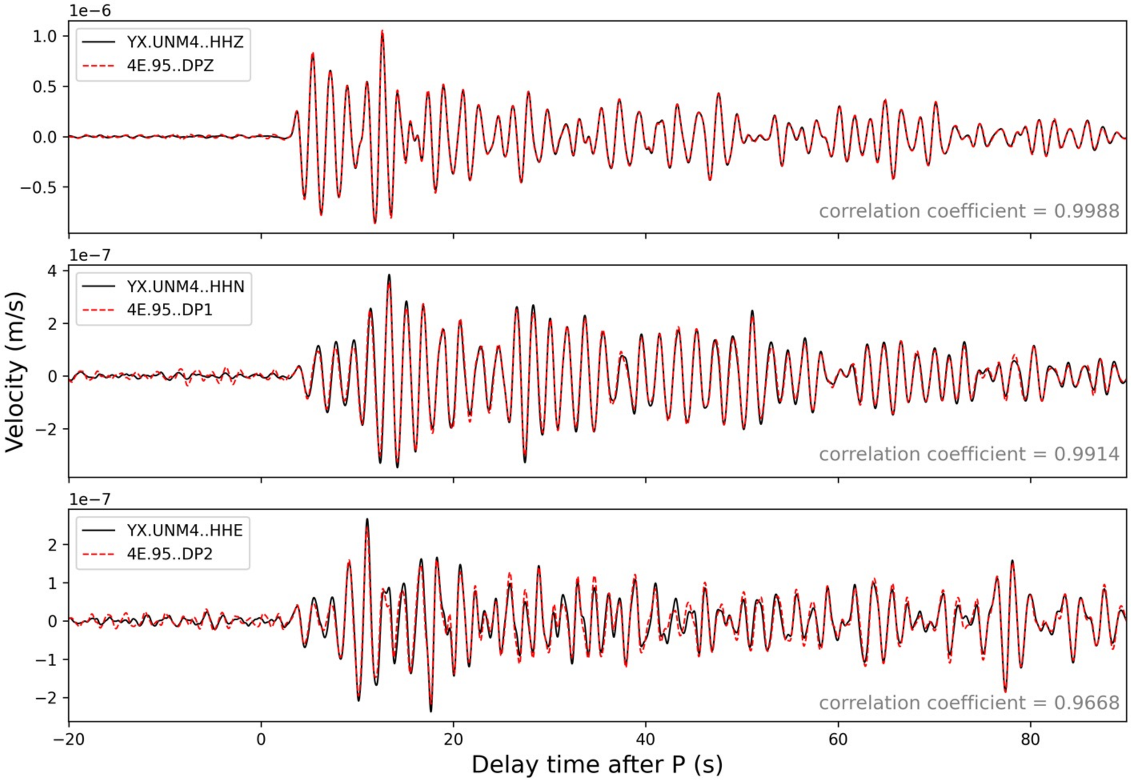

Figure 3.4.2: Comparison of co-located nodal station (4E.95) and broadband station (YX.UNM4) recordings of the June 02, 2018, 11:53:09 UTC Samoa Islands region event after preprocessing. A bandpass filter (0.5–2.0 Hz) has been applied to these waveforms.

3.4.3 Receiver Function Calculation

The receiver function method is one of the most commonly used passive source imaging tools to study the crust and upper mantle velocity structure (e.g., *Zhang and Schmandt*, 2019). The method leverages the conversion of incoming body waves (P- or S-waves) at boundaries with significant impedance contrast. A typical receiver processing workflow involves (*Langston*, 1979; *Vinnik*, 1977): (a) rotating the waveforms from the station vertical, north, east (ZNE) coordinate system to an earthquake coordinate system to try to separate vertical, radial and transverse (ZRT) energy. (b) Deconvolving the vertical from the horizontal components to remove the effect of different source time functions in the frequency-domain (e.g.,

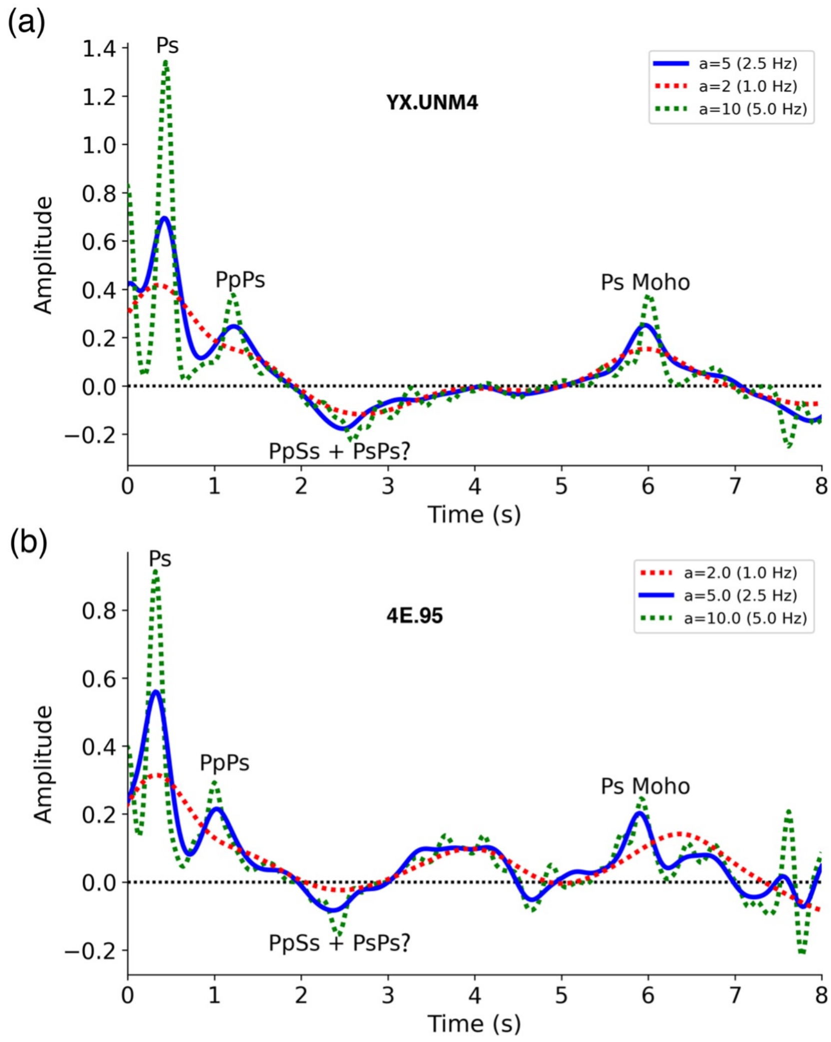

Figure 3.4.3: Average moveout corrected radial-component receiver function traces. (a) 1, 2.5 and 5 Hz receiver functions for broadband station UNM4 receiver functions. (b) 1, 2.5 and 5 Hz receiver functions for nodal geophone station 95.

Bostock, 1998), in the time-domain (e.g., *Ligorria and Ammon*, 1999) or other appropriate methods. (c) Applying a moveout correction to the data to subdue the effects of varying epicentral distances before stacking.

We rotated all our seismograms from the station ZNE coordinate system to the ZRT system and used the time-domain iterative deconvolution method on all waveforms to produce 1-20 Hz receiver functions. Finally, we applied a moveout correction using a 1-D velocity model (*Rubinstein et al.*, 2014) used in previous studies for

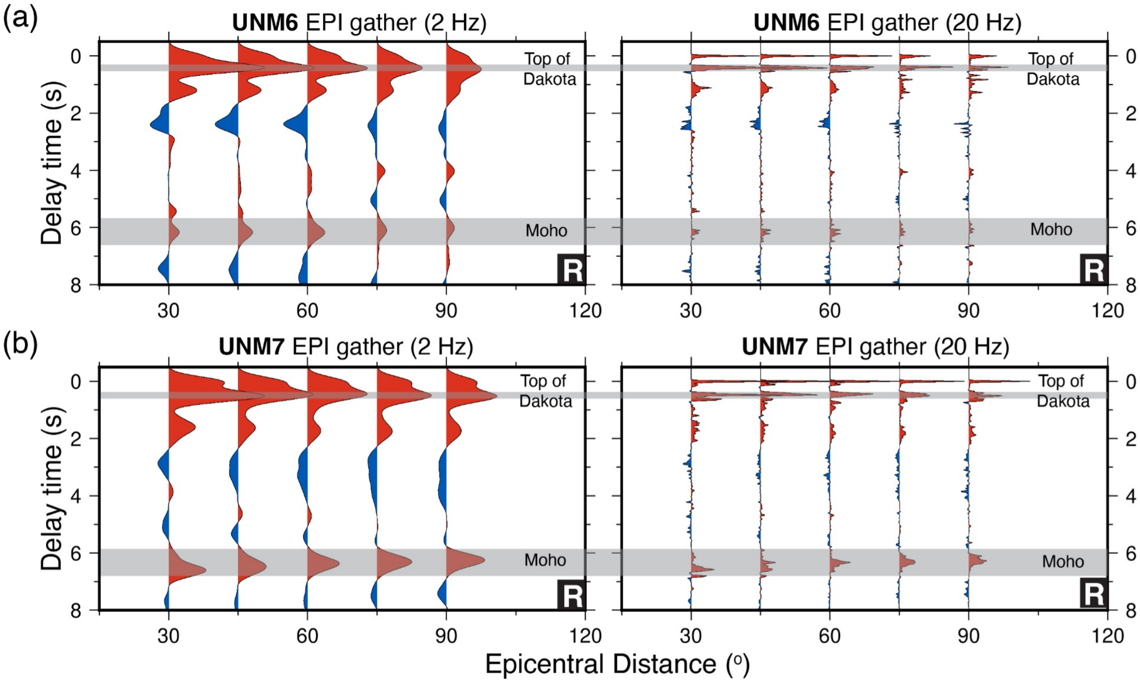

Figure 3.4.4: Example of epicentral (EPI) gathers showing interpreted top of Dakota and Moho signals at different frequencies. (a) R-component of gathers from UNM6. (b) R-component of gathers from UNM7.

hypocenter estimation (e.g., *Glasgow et al.*, 2021; *Wang et al.*, 2020). All analysis was performed using the open-source rf software package (*Eulenfeld*, 2020).

3.4.4 EPI Gather Analysis

We sort the estimated radial and transverse component receiver functions time series into epicentral (EPI) gathers for each station, stacked them in bins of 30°, with 50% overlap between the bins to accentuate coherent patterns (*Li and Nikulin*, 2022). Additionally, we converted all the receiver functions from time to depth (m) domain by applying the P-to-S delay time to depth formula (e.g., *Bourke et al.*, 2020; *Li and Nikulin*, 2022).

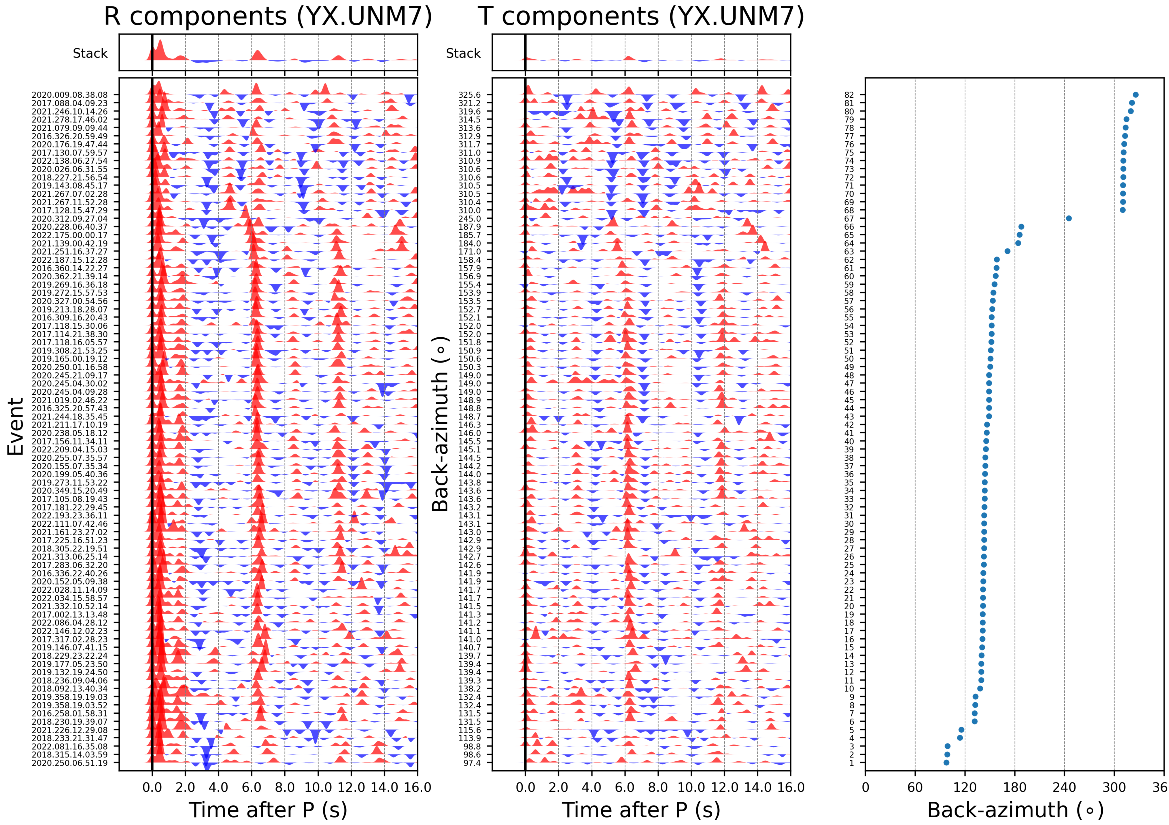

Figure 3.4.5: Example of back-azimuth plot of 2.5 Hz R- and T-component receiver functions. Note the coherent positive conversion on the R-component at ∼0.5 s.

3.4.5 H-k Stacking

Evaluating converted P-to-S phases at the Moho and their subsequent reverberations is a common method of extracting crustal properties from receiver functions (*Zandt and Ammon*, 1995; *Zhu and Kanamori*, 2000). *Zhu and Kanamori* (2000) introduced the H-κ stacking method which utilizes a grid search through thickness (H) and crustal V_P/V_S ratio (κ) to find the maxima amplitude of the stacked primary Moho conversion (Ps) and the reverberations (e.g., PpPs, PsPs+PpSs) of receiver functions from different epicentral distances and back-azimuths. Updated H-κ stacking methods were later proposed to deal with complex crustal structure such as sedimentary basins (e.g., *Yeck et al.*, 2013).

Yeck et al. (2013) exploited the frequency dependence of this method by using

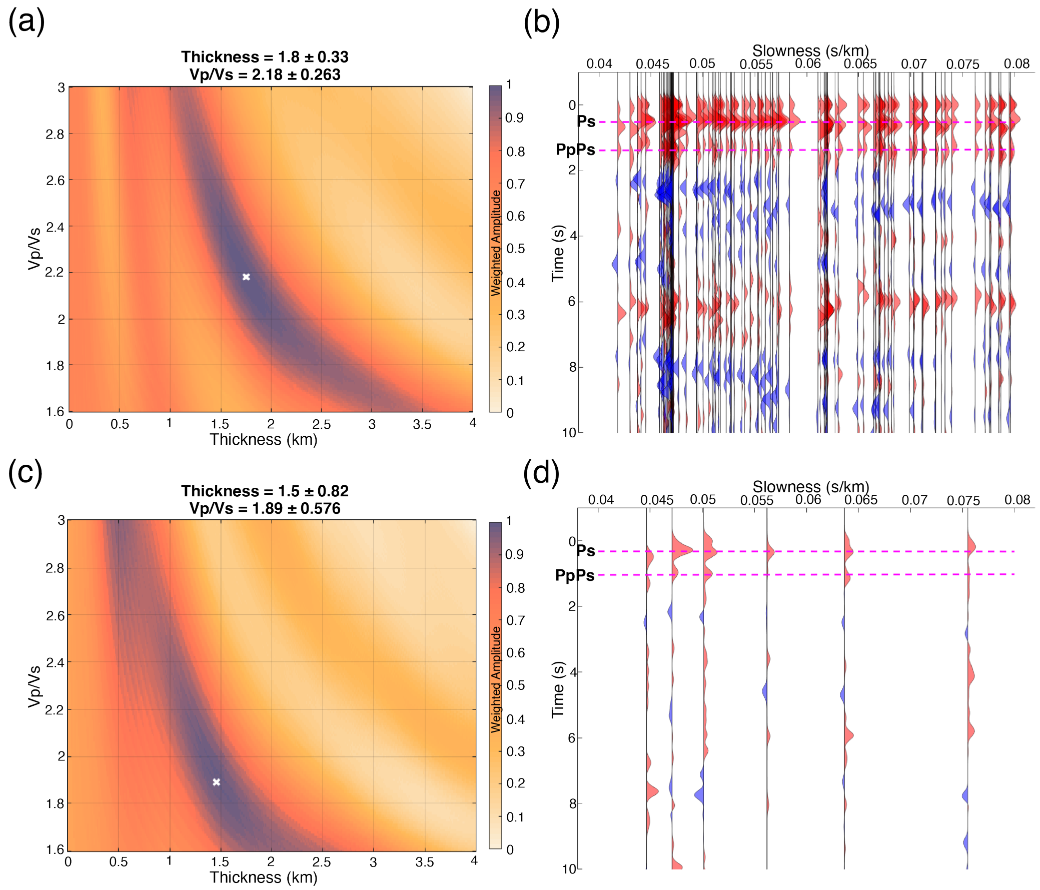

Figure 3.4.6: H-κ stacking results for UNM4 and 95. (a) Plot of the H-κ search space for UNM4 with the maximum values indicated with a white x. (b) UNM4's 2.5 Hz radial receiver functions used in the stack sorted by the slowness. Magenta lines show the moveout curves for the best estimates of the phase arrivals from H-κ stacking. (c) Plot of the H-κ search space for nodal station 95. (d) Station 95's 2.5 Hz Radial receiver functions.

high-frequency receiver functions to successfully obtain sediment thickness. Since the focus of this study was the shallow crust (<5 km depth), we used the original H-κ stacking routine introduced by *Zhu and Kanamori* (2000) on high frequency (2.5 and 5 Hz) receiver functions to constrain basement depth and determine the mean V_P/V_S of the layer above it. The H-κ grid search was performed through a sediment-thickness (H) range 0–4 km and a V_P/V_S (κ) range of 1.6–3.0 for an assumed average V_P of 4.2 km/s for the upper 4 km, from (*Rubinstein et al.*, 2014). We used a grid spacing of 0.01 for both H and κ parameters.

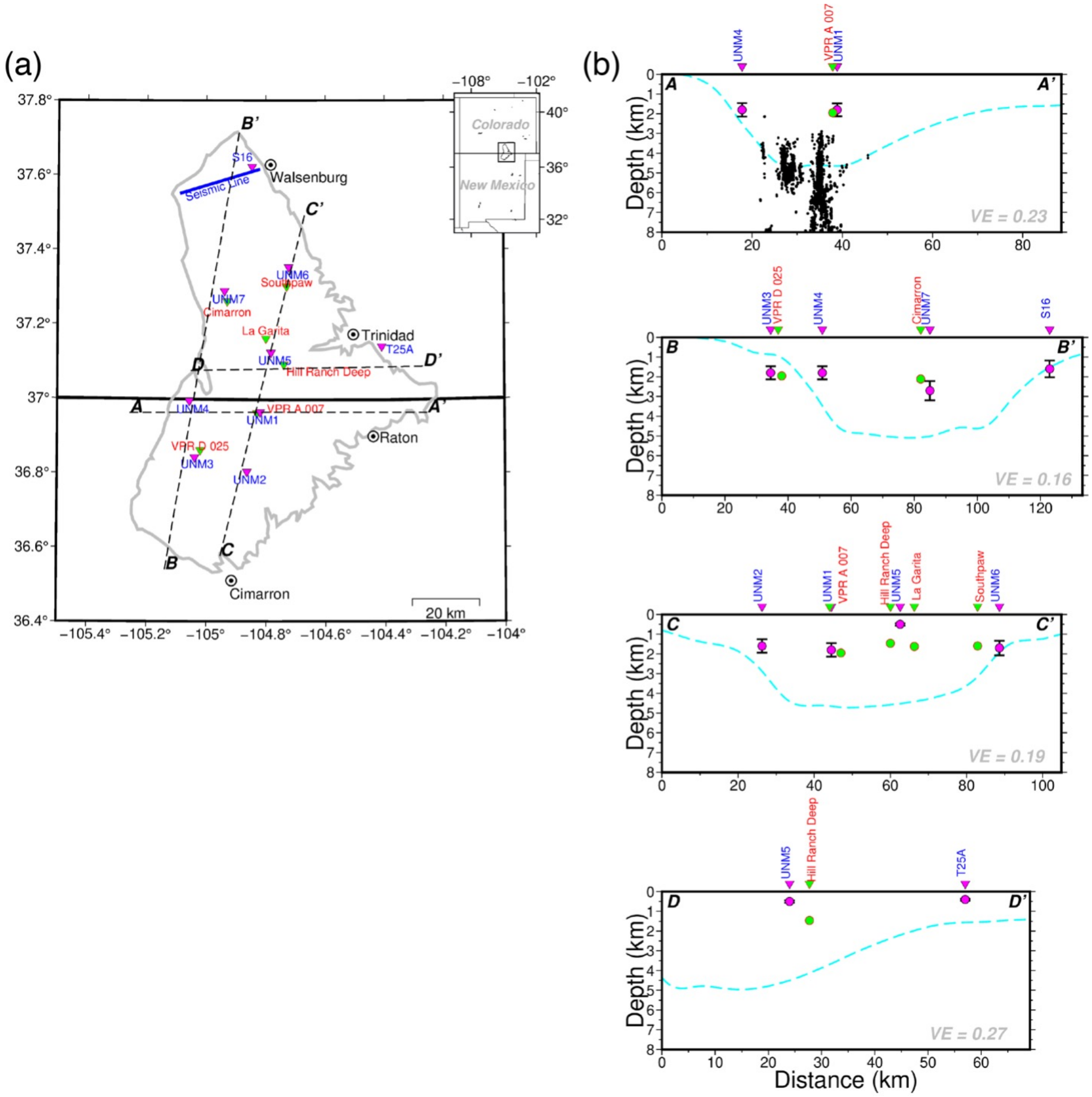

Figure 3.4.7: Comparison of H-κ stacking results with well data. (a) Map showing broadband array, near co-located injection wells. (b) Cross-sections of profiles shown in (a). Mooney & Kaban (2010)'s top of the Precambrian basement (cyan dashed line). Wang et al. (2020) relocated catalog (black dots). Magenta circles with error bars are H-κ stacking results from this study and green circles are the top of the Dakota calculated from the elevation of the known top of Dakota formation from the wells onsite.

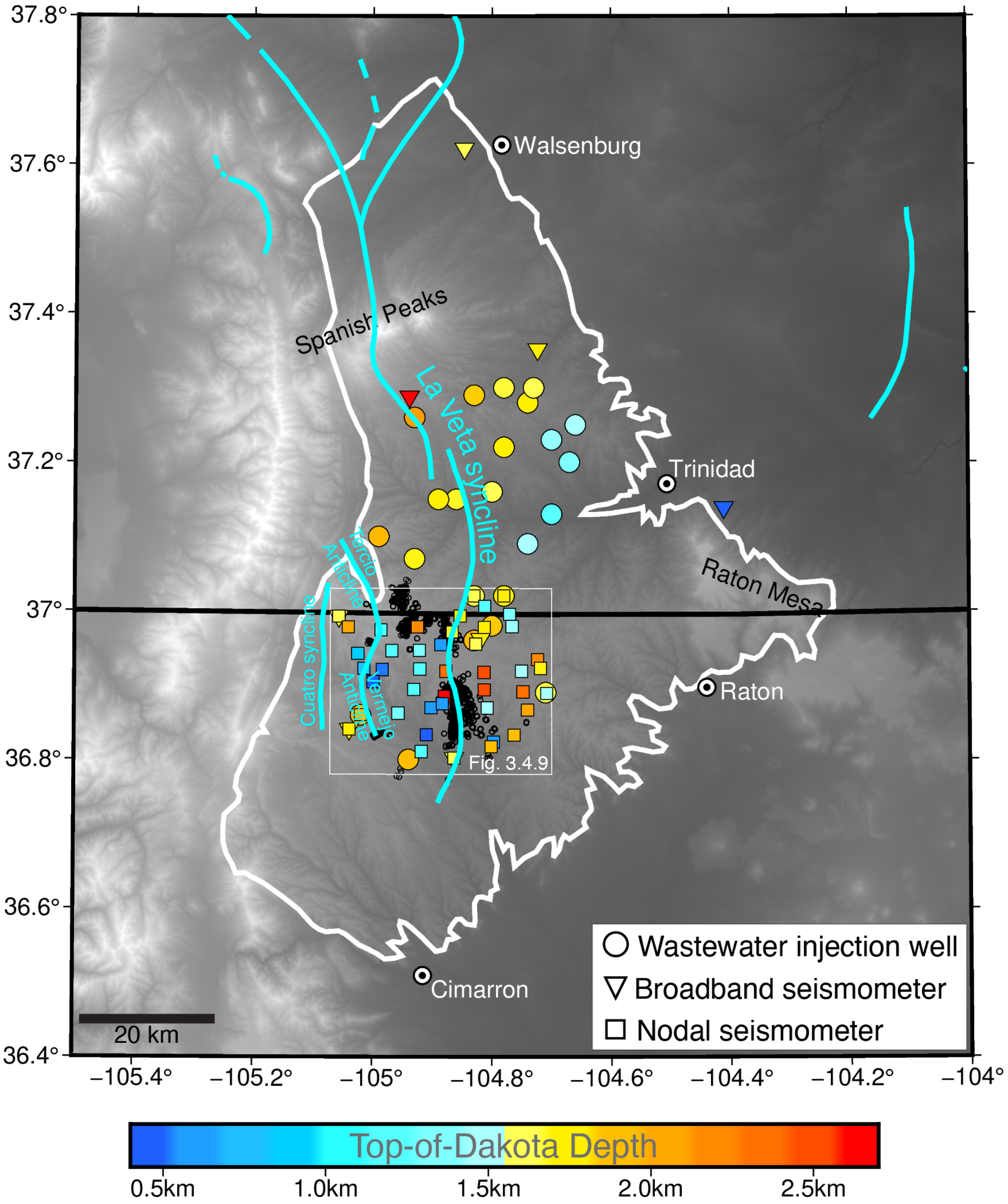
37.8°
37.6°
37.4°
37.2°
37°
36.8°
36.6°
36.4°
−105.4°
−105.2°
−105°
−104.8°
−104.6°
−104.4°
−104.2°
−104°
Walsenburg
Spanish Peaks
La Veta syncline
Trinidad
Raton Mesa
Raton
Cimarron
Cuatro syncline
Vermejo Anticline
Fig. 3.4.9
20 km
Wastewater injection well
Broadband seismometer
Nodal seismometer
Top-of-Dakota Depth
0.5km
1.0km
1.5km
2.0km
2.5km

Figure 3.4.8: Compilation of basin-wide top-of-Dakota depth measurements. Circles are depths from wells, triangles are depths estimated by the broadband array and the squares are depths estimated by the nodal array. Black circles are earthquakes detected by Wang et al., (2020).

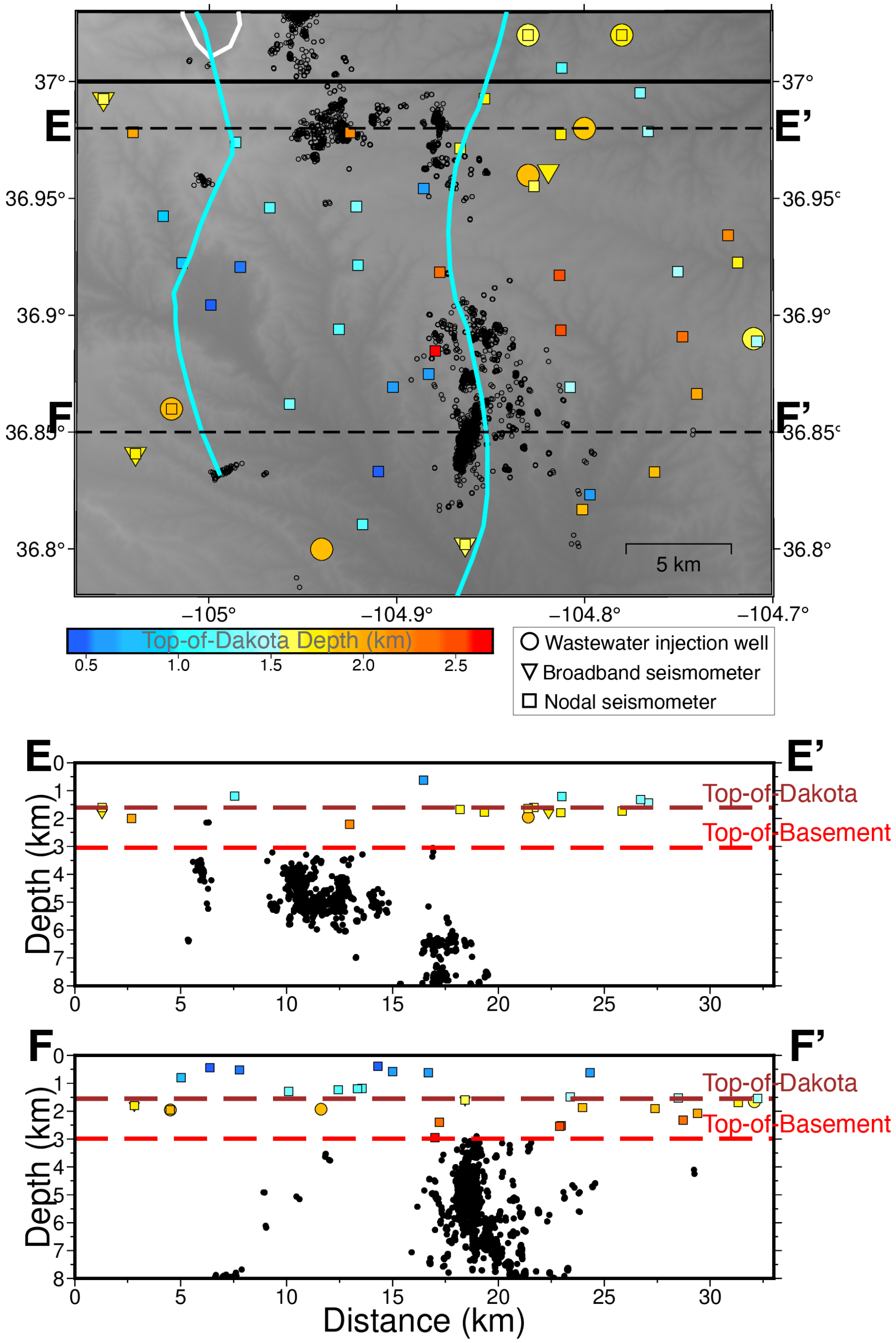

Figure 3.4.9: Zoomed-in area in Figure 3.4.8 above. Events, wells and seismometers between latitude 36.95°and 37.0° are projected to transect E-E'. Events, wells and seismometers between latitude 36.78° and 36.925°are projected to transect F-F'. Top of Dakota (brown dashed lines) inferred from the mean of the wells and seismometer estimates that are projected to the line. Top of basement (red dashed lines) inferred assuming a cumulative thickness of 1.438 km (e.g., Weingarten, 2015) for all the layer between the top of Dakota and the top of basement.

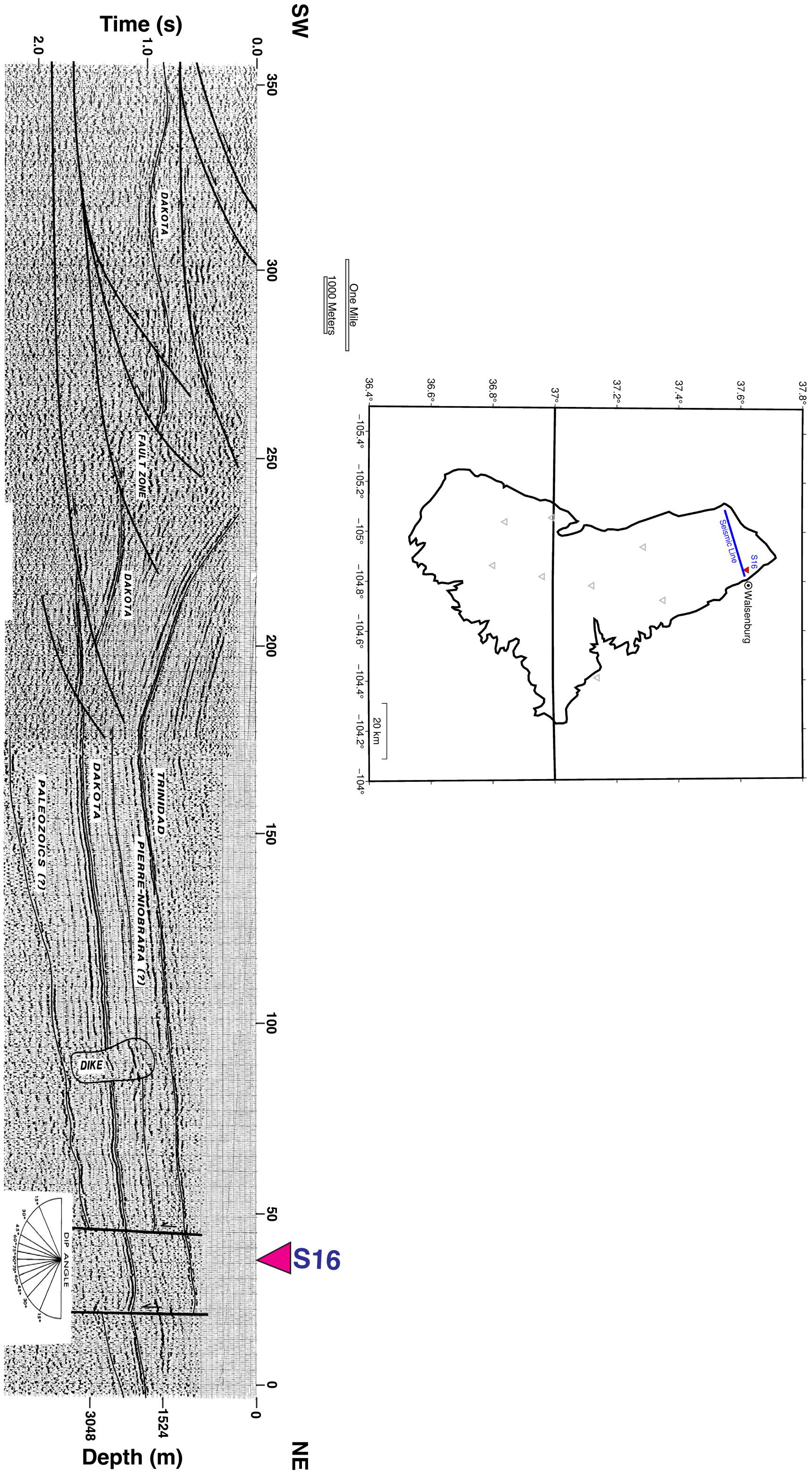
SW
NE
Time (s)
0.0
1.0
2.0
Depth (m)
0
1524
3048
350
300
250
200
150
100
50
0
DAKOTA
FAULT ZONE
DAKOTA
TRINIDAD
PIERRE-NIOBRARA (?)
DAKOTA
PALEOZOICS (?)
DIKE
DIP ANGLE
S16
One Mile
1000 Meters
36.4°
36.6°
36.8°
37°
37.2°
37.4°
37.6°
37.8°
−105.4°
−105.2°
−105°
−104.8°
−104.6°
−104.4°
−104.2°
−104°
Seismic Line
S16
Walsenburg
20 km

Figure 3.4.10: Modified from Applegate and Rose (1985). Legacy seismic line for the northern Raton Basin. Magenta triangle marks the location of S16 on the line.

3.4.6 Stratigraphic Data

Most injection wells in the Raton Basin are targeted at the Dakota Formation so the elevation to the top of this horizon is well-documented and is publicly available. To aid our interpretation, we compiled the injection wells' thickness to the top of the Dakota Formation (Table 3.4.1; Figure 3.2.2) from the Colorado Oil and Gas Conservation Commission (*COGCC*, 2022) and New Mexico Oil Conservation Division (*NMOCD*, 2022). We computed thicknesses to the tops of the Dakota Formation and compared them with H-κ thickness estimates from seismic stations within the injection well footprint.

3.5 Results

3.5.1 Receiver Function Results

Receiver functions calculated from both broadband and nodal arrays show the characteristic delayed sediment direct P in low-frequency receiver functions associated with sedimentary environments (Figure 3.4.3). In higher frequencies, the delayed sediment direct P separates into a low amplitude direct P and a high amplitude Ps (Figure 3.4.3a).

We observe a coherent primary conversion at $\sim$0.5 s in most of the EPI gathers (Figure 3.4.4) and back-azimuth plots (Figure 3.4.5). While the PpPs multiple comes in consistently at $\sim$1.2 s, the PpSs+PsPs negative multiple arrives at the expected $\sim$2 s mark in events closer to the array but disappears further away (e.g., Figure 3.4.4). We also observe the Moho Ps arrival at $\sim$6.0 s in most of the receiver functions.

3.5.2 H-k stacking Results

We present results for H-κ stacked 2.5 Hz receiver functions (Table 3.5.1) which show a consistent thickness of ∼1.8 km for much of the basin (UNM1–4 and UNM6). UNM5's thickness estimate of ∼0.5 km is an outlier compared to the other broadband station in the middle of the basin. As expected, T25A located at the edge of the basin has the thinnest estimated thicknesses.

Station	**Thickness, H(km)**	**Vp/Vs,k**	**Poisson Ratio, σ**
UNM1	1.8 ± 0.34	1.98 ± 0.237	0.329 ± 0.044
UNM2	1.6 ± 0.34	2.21 ± 0.327	0.371 ± 0.037
UNM3	1.8 ± 0.33	2.09 ± 0.266	0.352 ± 0.039
UNM4	1.8 ± 0.33	2.18 ± 0.263	0.367 ± 0.033
UNM5	0.5 ± 0.06	2.96 ± 0.134	0.436 ± 0.006
UNM6	1.7 ± 0.37	2.05 ± 0.299	0.344 ± 0.045
UNM7	2.7 ± 0.49	1.70 ± 0.140	0.235 ± 0.055
T25A	0.4 ± 0.05	2.94 ± 0.176	0.435 ± 0.008
S16	1.6 ± 0.42	2.35 ± 0.476	0.389 ± 0.039

Table 3.5.1: H-k stacking results for the broadband array

To get clearer maxima for the nodal stations, we stacked the normalized H-κ surfaces for the 2.5 and 5 Hz receiver functions. Thickness estimates for near co-located nodal and broadband stations (e.g., Figure 3.4.6) are close enough to suggest that thickness estimates from the nodal geophones are just as robust as the broadband instruments. While the thickness estimates are well determined, the V_P/V_S is poorly constrained because the Ps, PpPs and PpSs+PsPs arrive so close to each other. For nodes, arrivals later than the PsPs phase are not clear.

3.6 Discussion

3.6.1 Limitations of Seismic Imaging

As noted earlier, UNM5's thickness is inconsistent with the sediment thickness estimates from nearby Hill Ranch Deep and La Garita wells (1.323 and 1.624 km respectively, Figure 3.4.7). It is well documented that the Colorado section of the Raton Basin is dominated by Late Oligocene to Early Miocene dikes, sills, laccoliths and stocks. Regional gravity models suggest high density plutons underlie much of the area possibly due to a combination of intrusive and contact metamorphic rocks. Since UNM5 is tightly surrounded by middle Tertiary intrusive rock outcrops, we suggest that the impedance contrast observed in the receiver functions and the subsequent erroneous thin sediment thickness result is because sediment beneath the station and above the Dakota Sandstone has been altered by contact metamorphism or there is an intrusive layer present at ∼0.5 km depth. We note that the thickness estimate from UNM5 (0.5 km) is similar to the estimate from T25A (0.4 km) located near the Raton Mesa basalt flows to the east (Figure 3.2.3).

3.6.2 Identification of the Top-of-Dakota Formation Signal

For seismic stations other than UNM5 and T25A (addressed in section 3.6.1), average top of Dakota sandstone depths from the H-κ stacks range from 1.6 km (S16) to a maximum of 2.7 km (UNM7) for the broadband array. Figure 3.4.7 shows a compilation of top-of-Dakota depths from select wells from Table 3.4.1 with known top-of-Dakota depths, estimates from broadband stations UNM1, UNM3, UNM6, UNM7 and node station 20. In all cases there is good agreement between the receiver function depths and the nearby wells.

Literature search did not yield active source seismic reflection profiling in the Raton Basin that successfully constrained the top-of-basement depth. Plausible estimates inferred from the depth of the thin Paleozoic sequence immediately above the basement (e.g., *Applegate and Rose*, 1985) places the basement >1 km below the Dakota sandstone but we did not find published seismic reflection profiles with clear basement definition. Station S16 which lies on the *Applegate and Rose* (1985) seismic line (Figure 3.4.10), has a thickness estimate of 1.6 km which coincides with the ∼1.6 km depth of the interpreted top-of-Dakota event. Thus, we can be confident that the basin-wide impedance contrast observed at ∼1.6 to 2.7 km is due to the top-of-Dakota Formation.

3.6.3 Implications for Induced Seismicity

The dominant wastewater injection unit in the Raton Basin is the Dakota Formation (*Nakai et al.*, 2017), yet a growing number of studies (e.g., *Rubinstein et al.*, 2014; *Weingarten*, 2015) suggest that most induced earthquakes occur within the crystalline basement, but basement depths were not well-constrained prior to our study. Permeable fault zones are thought to aid the transfer of pore pressure from the injection reservoir into the basement (*Nakai et al.*, 2017; *Wang et al.*, 2020) used the node array presented in this study to detect clusters of >10,000 earthquakes between ML -2.2 to 3 occurring on small scale faults in the basement.

In Figure 14, we estimate the top-of-Dakota along transect E-E' by calculating the mean thickness estimates from this study and nearby wells between latitudes 36.95° and 37.0° (mean = 1.60 km). For transect F-F' we average thickness estimates and injection well data between latitudes 36.78° and 36.925° (mean = 1.55 km). To estimate the basement depth beneath transect E-E' and F-F', we add an assumed cumulative thickness of 1.438 km (e.g., *Weingarten*, 2015, Table 3.6.1) for all sequences between the top of Dakota and the top of the basement. The resulting depths (∼3.04 km for E-E' and ∼2.99 km for F-F') coincide with the shallowest limit of most events detected by *Wang et al.* (2020), suggesting that seismicity extends approximately from the bottom of the Permian-Pennsylvanian age Sangre De Cristo Formation deep into the crystalline basement.

Raton Basin Members	Formations	Formation Average Thickness (m)
Dakota	Dakota	68
Purgatoire	Dakota	
Morrison	Morrison	109
Entrada	Entrada	36
Dockum	Dockum	125
Glorieta	Dockum	
Sangre De Cristo	Sangre De Cristo	1100

Table 3.6.1: Modified from Weingarten (2015). Thickness of formations below top-of-Dakota and above top-of-basement.

3.7 Conclusions

We calculated teleseismic receiver functions from 9 broadband and 96 nodal geophones to determine the geometry of impedance boundaries of the Raton Basin. We use the H-κ stacking method to estimate depths beneath each seismic station and compare the results with nearby wastewater injection wells. Our analysis shows that the top of the Dakota Formation is the most prominent seismic contrast across the Raton Basin. Seismicity extends from the sediment-basement boundary into the crystalline basement.

3.8 Data Availability Statement

All seismic data used in this study are available from the IRIS Data Management Center under network code YX (https://doi.org/10.7914/SN/YX_2016), XP (https://doi.org/10.7914/SN/XP_2008), TA (https://doi.org/10.7914/SN/TA) and 4E (https://doi.org/10.7914/SN/4E_2018). The IRIS DMC is supported by the National Science Foundation under Cooperative Support Agreement EAR-1851048. The authors obtained digital elevation data for Figure 2a from the U.S. Geological Survey (USGS) National Elevation Dataset (https://viewer.nationalmap.gov/basic, last accessed May 2022). Geologic map for Figure 2b (New Mexico section) was obtained from the Geologic Map of New Mexico from New Mexico Bureau of

Geology and Mineral Resources. The Digital Geologic map for Figure 2b (Colorado section) retrieved from the USGS (http://pubs.usgs.gov/of/1992/ofr-92-0507, last accessed June 2022). Regional sediment thickness data obtained from the Central and Eastern United States Seismic Source Characterization for Nuclear Facilities (CEUS-SSC) (www.ceus-ssc.com/Database/sediment Thickness for North America and Neighboring Regions.zip, last accessed June 2022). Figures produced by Python and Generic mapping Tools (Wessel et al., 2019).

References

Applegate, J. K., and P. R. Rose (1985), Structure of the Raton Basin from a regional seismic line.

Bostock, M. G. (1998), Mantle stratigraphy and evolution of the Slave province, *Journal of Geophysical Research: Solid Earth*, *103*(B9), 21,183–21,200, doi: 10.1029/98JB01069.

Bourke, J., V. Levin, L. Linkimer, and I. Arroyo (2020), A Recent Tear in Subducting Plate Explains Seismicity and Upper Mantle Structure of Southern Costa Rica, *Geochemistry, Geophysics, Geosystems*, *21*(12), e2020GC009,300, doi: 10.1029/2020GC009300.

COGCC (2022), Colorado oil and gas conservation commission, Colorado Department of Natural Resources.

Eulenfeld, T. (2020), rf: Receiver function calculation in seismology, *Journal of Open Source Software*, *5*(48), 1808, doi:10.21105/joss.01808.

Frezon, S. E., T. M. Finn, and J. M. Lister (1983), Total thickness of sedimentary rocks in the conterminous United States, *Tech. rep.*, doi:10.3133/ofr83920.

Glasgow, M., B. Schmandt, R. Wang, M. Zhang, S. L. Bilek, and E. Kiser (2021), Raton Basin Induced Seismicity Is Hosted by Networks of Short Basement Faults and Mimics Tectonic Earthquake Statistics, *Journal of Geophysical Research: Solid Earth*, *126*(11), e2021JB022,839, doi:10.1029/2021JB022839.

Hemborg, H. T. (1998), *Spanish Peak Field, Las Animas County, Colorado: Geologic setting and early development of a coalbed methane reservoir in the central Raton basin*, 33, Colorado Geological Survey, Department of Natural Resources.

Jachens, R. C., and B. C. Moring (1990), Maps of the thickness of Cenozoic deposits and the isostatic residual gravity over basement for Nevada, *Tech. rep.*, doi:10.3133/ofr90404.

Jachens, R. C., A. Griscom, and C. W. Roberts (1995), Regional extent of Great Valley basement west of the Great Valley, California: Implications for extensive tectonic wedging in the California Coast Ranges, *Journal of Geophysical Research: Solid Earth*, *100*(B7), 12,769–12,790, doi:10.1029/95JB00718.

Johnson, R. B. (1968), Geology of the igneous rocks of the Spanish Peaks region, Colorado, *Tech. rep.*

Johnson, R. C., and T. M. Finn (2001), *Potential for a basin-centered gas accumulation in the Raton Basin, Colorado and New Mexico*, US Department of the Interior, US Geological Survey.

Langston, C. A. (1979), Structure under Mount Rainier, Washington, inferred from teleseismic body waves, *Journal of Geophysical Research*, *84*(B9), 4749, doi:10.1029/JB084iB09p04749.

Li, Y., and A. Nikulin (2022), Basin-scale subsurface characterization using single-station teleseismic receiver function analysis, *The Leading Edge*, *41*(10), 700–708, doi:10.1190/tle41100700.1.

Ligorria, J. P., and C. J. Ammon (1999), Iterative Deconvolution and Receiver-Function Estimation, *Bulletin of the Seismological Society of America*, *89*(5), 1395–1400.

Mooney, W. D., and M. K. Kaban (2010), The North American upper mantle: Density, composition, and evolution, *Journal of Geophysical Research*, *115*(B12), B12,424, doi:10.1029/2010JB000866.

Nakai, J. S., M. Weingarten, A. F. Sheehan, S. L. Bilek, and S. Ge (2017), A Possible Causative Mechanism of Raton Basin, New Mexico and Colorado Earthquakes Using Recent Seismicity Patterns and Pore Pressure Modeling, *Journal of Geophysical Research: Solid Earth*, *122*(10), 8051–8065, doi:10.1002/2017JB014415.

NMOCD (2022), New Mexico oil and conservation division., New Mexico Energy, Minerals and Natural Resources Department.

Rubinstein, J. L., W. L. Ellsworth, A. McGarr, and H. M. Benz (2014), The 2001-Present Induced Earthquake Sequence in the Raton Basin of Northern New Mexico and Southern Colorado, *Bulletin of the Seismological Society of America*, *104*(5), 2162–2181, doi:10.1785/0120140009.

USGS (2022), Advanced national seismic system comprehensive earthquake catalog, United States Geological Survey.

Vinnik, L. (1977), Detection of waves converted from P to SV in the mantle, *Physics of the Earth and Planetary Interiors*, *15*(1), 39–45, doi:10.1016/0031-9201(77)90008-5.

Wang, R., B. Schmandt, M. Zhang, M. Glasgow, E. Kiser, S. Rysanek, and R. Stairs (2020), Injection-Induced Earthquakes on Complex Fault Zones of the Raton Basin Illuminated by Machine-Learning Phase Picker and Dense Nodal Array, *Geophysical Research Letters*, *47*(14), e2020GL088,168, doi:10.1029/2020GL088168.

Weingarten, M. B. (2015), On the interaction between fluids and earthquakes in both natural and induced seismicity.

Yeck, W. L., A. F. Sheehan, and V. Schulte-Pelkum (2013), Sequential H- Stacking to Obtain Accurate Crustal Thicknesses beneath Sedimentary Basins, *Bulletin of the Seismological Society of America*, *103*(3), 2142–2150, doi:10.1785/0120120290.

Zandt, G., and C. J. Ammon (1995), Continental crust composition constrained by measurements of crustal Poisson's ratio, *Nature*, *374*(6518), 152–154.

Zhang, H., and B. Schmandt (2019), Application of Ps Scattering Kernels to Imaging the Mantle Transition Zone With Receiver Functions, *Journal of Geophysical Research: Solid Earth*, *124*(1), 709–728, doi:10.1029/2018JB016274.

Zhu, L., and H. Kanamori (2000), Moho depth variation in southern California from teleseismic receiver functions, *Journal of Geophysical Research: Solid Earth*, *105*(B2), 2969–2980, doi:10.1029/1999JB900322.

Appendix

3.A Supplementary Figures

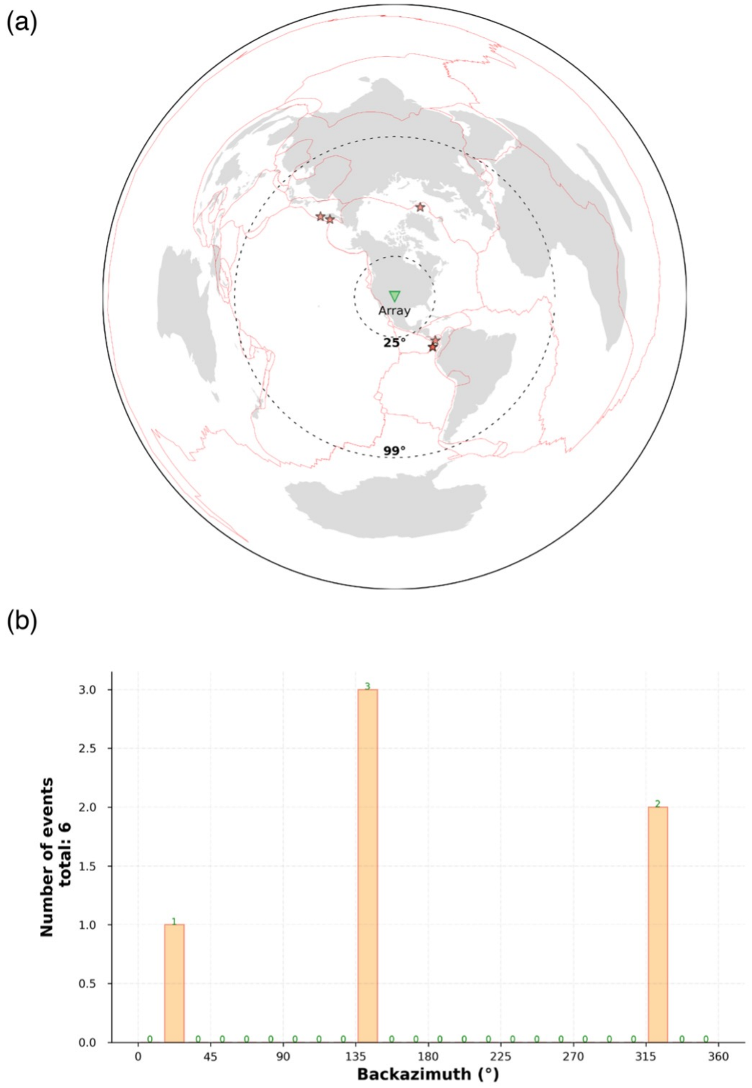

Figure 3.A.1: Distribution of M>5.5 seismic earthquakes used in the RF analysis for broadband seismometers. (a) Epicentral locations of events used for network YX, XP and TA respectively. (b) Back-azimuthal distribution of the selected earthquakes around the array.

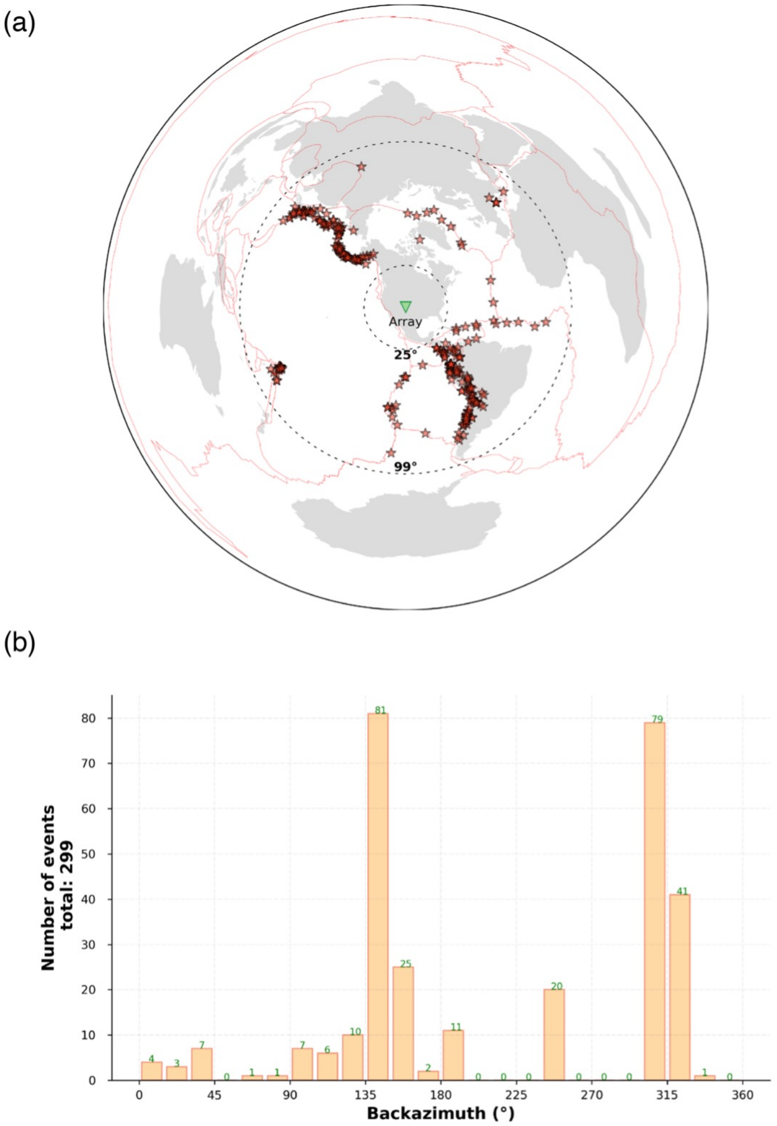

Figure 3.A.2: Distribution of M>5.5 seismic earthquakes used in the RF analysis for broadband seismometers. (a) Epicentral locations of events used for network YX, XP and TA respectively. (b) Back-azimuthal distribution of the selected earthquakes around the array.